THERMOMECHANICAL RELIABILITY OF MICROELECTRONICS

A DISSERTATION PRESENTED

BY

ZHEN ZHANG

TO

HARVARD SCHOOL OF ENGINEERING AND APPLIED SCIENCES

IN PARTIAL FULFILLMENT OF

THE REQUIREMENTS FOR THE DEGREE OF

DOCTOR OF PHILOSOPHY

IN THE SUBJECT OF

ENGINEERING SCIENCES

HARVARD UNIVERSITY

CAMBRIDGE, MASSACHUSETTS

APRIL 2007

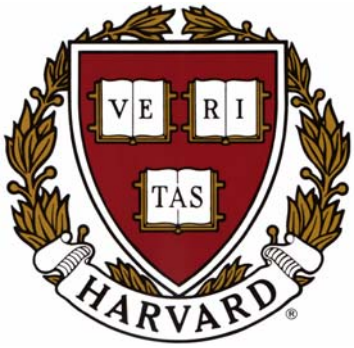

THERMOMECHANICAL RELIABILITY OF MICROELECTRONICS

Advisor: Professor Zhigang Suo Author: Zhen Zhang

Abstract

The microelectronic devices integrate more and more diverse materials in a complicated three-dimensional structure with feature size from nanometers to meters. The performance leaps of these devices are so attractive; meanwhile the reliability issues become more urgent in semiconductor industry. Among all of the reliability issues, the thermal-mechanical aspect is always one major concern. This dissertation will cover the following key issues.

One is the stress concentration that leads to many failure modes. In the microelectronic devices, the integrated diverse materials are of different thermomechanical properties, and usually bonded together to form the sharp features, such as trenches, wedges, corners or junctions. These sharp features can concentrate stresses, which in turn fail the devices in the ways of cracking, debonding, or injecting dislocations, etc. Therefore, the study of the singular stress filed around the sharp features should draw a lot of attention. Usually, the singular stress field is a linear superposition of two modes, one stronger and the other weaker, known as *split singularities*. A dimensionless parameter, called the *local mode mixity*, is defined to characterize the proportion of the two modes at the length scale where the processes of

fracture occur. We apply the theory of split singularities to the problems such as crack penetration or deflection, dislocation injection into strained silicon, and interfacial delamination due to chip-package interaction. In addition, a remedy to reduce the singularity and to suppress the debonding is verified in flexible electronics — applying coating.

Another long-standing failure mode is voiding in interconnects due to the thermal strains and electromigration. This failure mode is exacerbated by the recent introduction of low-permittivity dielectrics. We describe a method to calculate the *volume of a saturated void*, attained in a steady state when each point in a conductor line is in a state of hydrostatic pressure, and the pressure gradient balances the electron wind. The results indicate that at operation conditions, both thermal strains and electromigration make significant contributions to the void volume. We discuss these results in the context of interconnect design.

Table of Contents

List of Figures

List of Tables

List of Publications

1. Zhen Zhang, Nanshu Lu, Juil Yoon, and Zhigang Suo, "Chip-package interaction and interfacial delamination." 2007. (unpublished)
2. Juil Yoon, Zhen Zhang, Nanshu Lu, and Zhigang Suo, "The effect of coating in increasing the critical size of islands on a compliant substrate." *Applied Physics Letters*, 2007 (in press)
3. Martijn Feron, Zhen Zhang and Zhigang Suo, "Split singularities and dislocation injection in strained silicon." *Journal of Applied Physics*, 2007. (in press)
4. Zhen Zhang, Juil Yoon and Zhigang Suo, "Method to analyze dislocation injection from sharp features in strained silicon structures." *Applied Physics Letters,* **68**(26): 261912, (2006). doi:10.1063/1.2424665 .
5. Zhen Zhang, and Zhigang Suo, "Split singularities and the competition between crack penetration and debond at a bimaterial interface." *International Journal of Solids and Structures*, **44**(13):4559-4573, (2007). http://dx.doi.org/10.1016/j.ijsolstr.2006.11.035.
6. Zhen Zhang, Zhigang Suo, Yong Liu, Scott Irving, Timwah Luk and Don Desbiens, "Methodology for avoidance of ratcheting-induced stable cracking (RISC) in microelectronic devices", in *Proceedings of the 56th Electronic Components and Technology Conference*, San Diego, USA, May 30-June 2, 2006, pp.1429-1435. doi:10.1109/ECTC.2006.1645844.
7. Zhen Zhang, Zhigang Suo, and Jun He, "Saturated voids in interconnect lines due to thermal strains and electromigration", *Journal of Applied Physics*, **98**, 074501, (2005). doi:10.1063/1.2061896 .

8. Jim Liang, Zhen Zhang, Jean H. Prevost, and Zhigang Suo, “Time-dependent crack behavior in an integrated structure”, *International Journal of Fracture,* **125,** 335-348 (2004). doi: 10.1023/B:FRAC.0000022238.52635.88 **.**

Acknowledgements

I would like to express my gratitude to all those who made this dissertation possible. Firstly, I would love to give my special appreciation to my research advisor, Professor Zhigang Suo, who provided a motivating, encouraging, and enthusiastic environment during my pursuit of doctoral research. The life of a PhD student at Princeton and Harvard is not easy any way, at least to me. However, it was his steady support and inspiring guidance that brought this dissertation to its fruition. It was a great pleasure to conduct my work under his mentoring.

Secondly, I would like to thank Prof. John W. Hutchinson, Prof. Frans Spaepen and Prof. Joost J. Vlassak, for being my committee members and for their suggestions and comments on my research. I would love to thank Prof. James R. Rice for his help on the fracture mechanics topics and his support on my defense. I would also like to thank Prof. Michael J. Aziz, since I not only learned thermodynamics in his class, but also was given the chance to be the teaching fellow for his class. It was really a wonderful experience.

Thirdly, I would like acknowledge my collaborators, Dr. Juil Yoon and Ms. Nanshu Lu in Suo's group, Mr. Martijn Feron from Technische Universiteit Eindhoven, The Netherlands, Dr. Jun He and Dr. Jim Liang from Intel Corporation, for the valuable and fruitful discussions. Needless to say, that I am grateful to all of my colleagues in Suo's research group, especially Dr. Wei Hong, Mr. Xuanhe Zhao, Prof. Teng Li, Prof. Ting Zhu, Dr. Zhenyu Huang, Dr. Min Huang, Prof. Yanfei Gao, Mr. Nicolas Cordero, visiting Prof. Jinxiong Zhou from Xi'an Jiaotong University, and visiting Prof. Dunming Liao from Huazhong University of Science and Technology.

In addition, I want to thank Yong Liu and Scott Irving at Fairchild Semiconductor Corp. for their generosity to have provided me the great opportunity to do the internship in their team in the summer of 2005.

When I write this section, the list of those I want to acknowledge keeps increasing. For all those who helped me, though your name may not be listed explicitly, my heart goes to you in gratitude.

Finally, after acknowledgement to all mentioned above, I would love to come back to my family. This work would not have been possible without the devoted love and support from my parents, my grandmother, brothers, sisters, and all other family members.

This research was initiated under the support of the National Science Foundation (NSF) through the Materials Research Science and Engineering Center (MRSEC) at Princeton University. It continued to be supported by NSF through MRSEC at Harvard University, and then by Intel Corporation through a contract via the Semiconductor Research Corporation (award number 2005-KJ-1369), and by the Division of Engineering and Applied Sciences, Harvard University. I am grateful to these institutes for their support.

Chapter 1 Introduction to Reliability Physics in Electronics

Since 1950s, the thermomechanical reliability has been continuing to be one of the major concerns in microelectronics industry. In this chapter, Section 1.1 introduces a brief history of the research on the reliability physics, and discusses the current challenges that the industry confronts. Section 1.2 outlines the topics in this dissertation.

1.1 Reliability physics: history and present

In early 1950s, the reliability problems drew attention due to the needs to understand the failure mechanism of unreliable components in US Air Force equipment. And quickly, lots of problems were investigated on a wide front, such as measuring, predicting and testing of the parts, equipments, even the system reliabilities. The historic event in reliability physics was the first conference on electrical and electronic interconnections, named “Holm Conference”, in 1955. In this conference, researchers reported most of the physical failure mechanisms known to occur in the field of electrical

interconnections. At that time, the statistical approaches were widely adopted to determine the states of reliability of the devices (Ebel, 1998).

However, the microelectronics industry had started booming in late 1950s. The rapid progress of new designs, new materials, manner of fabrications, operation conditions, application criteria, etc, negated the existing data and models. The establishment of new reliability data on the new devices required expensive testing and was time-consuming. Even further, the improvement of analysis of new data could not catch up the development of new devices.

Hence, the reliability physics, or "physics of failure", was created in the early 1960s. Researchers tried to establish the quantitative reliability requirements for devices, and related the fundamental physical and chemical behavior of materials to reliability parameters. The significance, influence, and challenges on reliability studies were just as stated by Harry Davis, the deputy for research, office of the assistant secretary of defense (R&D) USA, in 1962's symposium of "physics of failure in electronics":

"The subject of this symposium, 'The Physics of Failure' in my opinion is the very heart of the reliability effort, and a thorough understanding of mechanism and physics of failures will be the principal means by which extreme reliability requirements posed by advanced systems will be met. Our failure to understand the basic mechanisms which lead to short and long term changes in the properties of electronic parts and materials is without a doubt the most important cause of the very serious reliability problems which face the nation today. As a result, improvement in part reliability during recent years has been incremental compared to the rapid rate of other technological progress. Procedures for reliability testing and design control continue to be time-

consuming and expensive."

There are many aspects about the reliability in electronics, such as electrical, thermal, mechanical or chemical reliabilities. As far as the thermal-mechanical aspects of reliability issues are concerned, researchers accomplished great achievements in 60s and 70s in both modeling and experiments. The important milestones should be mentioned. For example, electromigration has been a persistent failure mode ever since integrated circuits were mass-produced and the failure mechanism was figured out (Blech and Meieran, 1967; Black, 1967). Anstead (1967) and Bosselaar (1968) presented the work on the scanning electron microscope (SEM), the most essential failure analysis tool for integrated circuits. Ebel (1972) presented an approach to wafer testing. Zakraysek (1973) discussed the gold embrittlement of solder joints, which was a recurring problem in the electronics industry. Libove (1975) discussed reliability problems related to device packages. It covered destructive stresses placed on packages during sealing and testing. The author predicted that, during dynamic thermal cycles, compressive glass-to-metal seals could temporarily open during rapid temperature changes and then return to a hermetic condition once the temperature stabilized. This was later proven by actual testing. Trai, Lee, and Wang (1979) used transmission acoustic microscopy in failure analysis, and led to methods used today to evaluate die attachment integrity of plastic encapsulated integrated circuit. By the early 1980s, the reliability physics entered the era of specialization. Many annual meetings and workshops were catered to different branches of reliability physics.

With the rapid development of new devices, one concern was the determination the field reliability of these devices with a minimum expenditure of time and money. The

most accepted method was the accelerated testing. An important paper from Bell Telephone Laboratories by Dodson and Howard (1961), being published in the 1961's Proceedings of the NSRQC---the National Symposium on Reliability and Quality Control, formed the basis for much of the accelerated testing efforts in reliability physics. This paper justified the Arrhenius model of temperature dependence for semiconductor devices. Later on, the guidelines on accelerated testing were established by a series of works (Partridge, 1963; Bretts et al., 1963; Peck, 1971; Zierdt, 1971).

Since the integrated circuits became available commercially in 1961, the number of transistors doubles every 18~24 months in a single chip, the so-called "Moore's law". Over the past 40 years, Moore's law was remarkably true and remains to be true as markets continue to demand maximum performance and minimum cost. The miniaturization, new processes, and new materials, among many other means, are essential to these demands. Meanwhile, all those changes result in profound challenges to the reliability in all aspects. For example, thin film cracking, interfacial delamination of organic and metallic interfaces, solder joints detachment at first and second level interconnects, electromigration in conductor lines, vias, bumps, and package traces, potential moisture ingress on die edge seal and low-*k* dielectrics, stress-induced voiding in copper lines due to thermal mismatch and electromigration, integrity of package assembly, etc. The advanced semiconductor devices will require increased effort from reliability physics practitioners if the industry is to keep Moore's Law on course. The physical failure mechanisms must be determined in a timely fashion to keep up with the pace. People solve the old problems, but simultaneously create new ones. The reliability is a persistent challenge.

In the 21st century, the nanotechnology spurs the development of semiconductor industry and brings a broad set of reliability challenges at a pace that has not been seen in the past. Many aspects of semiconductor design and manufacturing will undergo dramatic changes that threaten the nearly unlimited lifetime and high level of reliability. But, customers still expect maximum performance and minimum cost even though the complexity of products has increased. In the era of nanometer regime, product cost and performance requirements will be substantially affected and, in many cases, superseded by reliability constraints. As listed out by SEMATECH (2003) and ITRS (2005), the copper/low-*k* interconnects, packaging, and the associated design and test for reliability are among the top reliability concerns in the near future at least to 2010. As far as copper/low-*k* interconnects concerned, the rapid introduction of new materials, processes that are necessary to reduce the resistance-capacitance (RC) delay creates integration and material characterization challenges. Integration complexity, process flow, techniques, and tools often create first order reliability challenges. The importance of characterizing these materials and processes for reliability as well as for performance cannot be overstated. Packaging in the nanometer regime also raises reliability concerns. The increased complexity and performance requirements for packaging these products act as an exponential multiplier for many of the failure mechanism besides introducing new ones. Detecting, testing, modeling and control of failure mechanisms will be the key to achieve necessary reliability.

"As the market demand continues to push product performance to its technological limits, the tradeoff between performance and lifetime must be tailored to the needs of different market segments. No longer can a single product satisfy all

applications with significant reliability and performance margins. This in turn requires that accurate reliability models and tools for lifetime estimation must be available during the product design stage. A failure mechanism-driven approach must be employed, identifying the potential failures and evaluating their kinetics and impact based on the specific application conditions and requirements of each market segment. An improved understanding of failure mechanisms and models is required. Together, these trends demand that reliability be modeled much more precisely during the product design cycle to make the correct performance vs. reliability tradeoffs. This in turn requires that the following be in place: (1) well developed physical models for failure mechanisms. (2) the variation to apply correct statistical models. (3) test methods and test structures to fully characterize each failure mechanism. (4) design tools to transform the test structure reliability predictions for individual failure mechanisms to a comprehensive product reliability model that fits the application operating conditions and environment." --- quoted from SEMATECH (2003).

Two other trends raise new requirements in the approaches to assure product reliability. First, the gap between normal operating condition and accelerated testing condition becomes narrower and narrower. Second, increased device complexity makes it impossible or prohibitively expensive to obtain sufficient fault coverage in accelerated life tests. As a result, the efficiency and even the ability to test reliability meaningfully at the product level are rapidly diminishing.

The introduction of new materials with more limited operating margins further accelerates this shift and requires that the potential failure mechanisms, the test structures, and the corresponding models be identified and developed well in advance of the

technology qualification.

In this section, we briefly reviewed the history and present of reliability physics. For more details, there are many review articles or industrial publications, such as Patrick et al (1991), Murarka (1997), Ebel (1998), Abtew and Selvaduray (2000), Ogawa (2002), Zeng and Tu (2002), Suo (2003), Tu (2003), among others. Lloyd and Thompson (1993), and Reuss and Chalamala (2003) have edited multi-author reviews of the reliability physics of microelectronics in MRS bulletins. The societies, such as International SEMATECH and Semiconductor Industry Association, usually update technology roadmaps and/or reports about the technology trends and the current and future reliability challenges. More information can be found at www.itrs.net and www.sematech.org.

1.2 Plan of the dissertation

In this dissertation, several key issues are investigated, such as cracking path selection, dislocation injection, chip-package interaction, suppression of debonding by coating, and voiding due to thermal strain and electromigration.

In Chapter 2, we study a very fundamental fracture problem without the complexity of real structures used in microelectronics. Since the stress concentration leads many failure modes, we set up a framework to study the concentrated stress field. The simplified geometry is a crack impinging upon a bimaterial interface at an angle. The stress field around the crack tip is a linear superposition of two singular modes, usually of unequal exponents, either a pair of complex conjugates, or two unequal real

numbers. In the latter case, a stronger and a weaker singularity coexist, known as split singularities. We define a dimensionless parameter, called the local mode mixity, to characterize the proportion of the two modes at the length scale where the processes of fracture occur. We show that the weaker singularity can readily affect whether the crack will penetrate, or debond, the interface. In the following chapters, we apply this framework to study other stress-induced failure phenomena.

The mobility of charge carriers in silicon can be significantly increased when silicon is subject to a field of strain. Hence, strained silicon technology is prosperous in the future to enhance the performance of microelectronics. However, a microelectronic device usually contains sharp features, e.g., edges and corners, which may intensify stresses, inject dislocations into silicon, and ultimately fail the device. In Chapter 3, we use the framework of split singularities and mode mixity to investigate the dislocation injection into strained silicon. After studying the general case, we focus on the material system of SiN/silicon since it is a commonly adopted structure in semiconductor industry. For this specific material combination, we simplify the singular stress field to a single mode, and therefore, simplify the criterion of dislocation injection. In addition, we use our analysis to interpret available experiments.

In Chapter 4, we extend the framework of split singularities and local mode mixity to investigate the interfacial delamination due to chip-packaging interaction. In flip-chip packages, the mismatch in thermal expansion coefficients between the silicon die and packaging substrate induces concentrated stress field around the edges and corners of die during assembly, testing and services. The concentrated stresses result in delamination on many interfaces on several levels of structures, in various length scales

from tens of nanometers to hundreds of micrometers. A major challenge to model flip-chip packages is the huge variation of length scales, the complexity of microstructures, and diverse materials properties. In this chapter, we simplify the structure to be silicon/substrate with 90^0 wedge configuration, and neglect the small local features of integrated circuits. This macroscopic analysis on package level is generic with whatever small local features, as long as the physical processes of interest occur in the region where the concentrated stress field due to chip-packaging interaction dominates. It is the same driving force that motivates all of the flaws. Therefore, the different interface cracks with same size and same orientation but on different interfaces should have similar energy release rates provided that the cracks are much smaller than the macroscopic length. We calculate the energy release rate and the mode angle of crack on the chip-package interface based on the asymptotic linear elastic stress field. The asymptotic solution agrees with finite element calculation very well for crack length varying several orders of magnitude. We discuss the simplified model and results in context of real applications.

In Chapter 5, a remedy to reduce the singularity and to suppress the debonding in flexible electronics is proposed—applying coating. A flexible electronic system may consist of a polymeric substrate and an array of stiff islands, on which devices are fabricated. When the substrate is stretched, the devices on the islands experience small strains, but the islands may debond if they exceed a critical size. We show that a thin layer of polymer coating, covering the islands and the substrate, can markedly increase the critical island size.

In Chapter 6, we turn our direction to study the voiding in conductor lines in

interconnects of copper/low-permittivity dielectrics. Both the electromigration and thermal strains due to mismatch in coefficients of thermal expansion can cause voids to grow in conductor lines. This long-standing failure mode is exacerbated by the recent introduction of low-permittivity dielectrics. We describe a method to calculate the volume of a saturated void, attained in a steady state when each point in a conductor line is in a state of hydrostatic pressure, and the gradient of the pressure along the conductor line balances the electron wind. Moreover, the effects of porous dielectrics and ultrathin liners are also investigated. We discuss the results in the context of interconnect design.

The last chapter gives concluding remarks and suggests possible future work.

References:

1. Abtew M, and Selvaduray G, “lead-free solders in microelectronics”, Materials Science & Engineering R-Reports 27(5-6): 95-141, 2000.
2. Black, J.R. “Mass transport of aluminum by momentum exchange with conducting electrons”, Proc. Sixth Ann. Reliability Physics Symp, 1967, pp 148 - 59.
3. Bretts, G., Kozol, J., and Lanspert, H. “Failure physics and accelerated testing”, Physics of failure in electronics, 2: 189-207, 1963.
4. Donson, G.A., and Howard, B.T.. “High stress aging to failure of semiconductor devices”, Proc. Seventh Nat’l Symp. Reliability and Quality Control, 1961, pp262-272.
5. Ebel, G.H. “High temperature reverse bias testing at wafer level”. Proc. Tenth Ann. Reliability Physics Symp, 1972, pp204-207.
6. Ebel G.H., “Reliability physics in electronics: A historical view”, IEEE Transactions on Reliability 47(3-SP): 379-389, 1998.
7. International SEMATECH Inc., Critical reliability challenges for the International Technology Roadmap for Semiconductors (ITRS), technology transfer #03024377A-TR, March 31, 2003.
8. Libove, C. “Rectangular flat-pack lids under external pressure-formula for screening arid design”, Proc. Thirteenth Int’l Reliability Physics Symp, 1975, pp38-47.

9. Lloyd J.R., and Thompson C.V., “materials reliability in microelectronics”, MRS Bulletin 18(12): 16-16, 1993.

10. Murarka S.P., “Multilevel interconnections for ULSI and GSI era”, Materials Science & Engineering R-Reports 19(3-4): 87-151, 1997.

11. Ogawa E.T., Lee K.D., Blaschke V.A., et al., electromigration reliability issues in dual-damascene cu interconnections , IEEE Transactions on Reliability 51(4): 403-419, 2002.

12. Patrick W.J., Guthrie WL, Standley CL, et al., “Application of chemical mechanical polishing to the fabrication of VLSI circuit interconnections”, Journal of The Electrochemical Society 138(6): 1778-1784, 1991.

13. Patridge, J. “On the extrapolation of accelerated stress conditions to normal stress conditions on germanium transistors”, Physics of Failure in Electronics, 2: 208-225, 1963.

14. Peck, D.S. “The analysis of data from accelerated stress tests”, Proc. Ninth Ann. Reliability Physics Symp, 1971, pp 69 - 78.

15. Reuss R.H. and Chalamala B.R., “Microelectronics packaging and integration”, MRS Bulletin 28(1):11-15, 2003.

16. Semiconductor Industry Association, International Technology Roadmap for Semiconductors (ITRS), 2005. Available at http://public.itrs.net.

17. Suo Z., “Reliability of Interconnect Structures”, in Volume 8: Interfacial and Nanoscale Failure (W. Gerberich, W. Yang, Editors), Comprehensive Structural Integrity (I. Milne, R.O. Ritchie, B. Karihaloo, Editors-in-Chief), Elsevier, Amsterdam, 2003, pp.265-324.

18. Trai, C.S., Lee, C.C., and Wang, J.K. “Diagnosis of hybrid microelectronics using transmission acoustic microscopy”, Proc. Seventeenth .ht ’1 Reliability Physics Symp, 1979, pp178-182.

19. Tu K.N., “recent advances on electromigration in very-large-scale-integration of interconnects”, Journal of Applied Physics 94(9): 5451-5473, 2003.

20. Zakraysek, L. “lntermetallic characterization”, Proc. Eleventh Ann. Reliability Physics Symp, 1973, pp 6 - 9.

21. Zeng K, and Tu K.N., “Six cases of reliability study of Pb-free solder joints in electronic packaging technology”, Materials Science & Engineering R-Reports 38(2): 55-105, 2002.

22. Zierdt, C.H. Jr. “Some circuit considerations and operating precautions for accelerated HTRB and operating testing of semiconductor devices”, Proc. Ninth Ann. Reliability Physics Symp, 1971, pp 79 - 83.

Chapter 2 Split Singularities and Cracking Path Selection

For a crack impinging upon a bimaterial interface at an angle, the singular stress field is a linear superposition of two modes, usually of unequal exponents, either a pair of complex conjugates, or two unequal real numbers. In the latter case, a stronger and a weaker singularity coexist, known as *split singularities*. We define a dimensionless parameter, called the *local mode mixity*, to characterize the proportion of the two modes at the length scale where the processes of fracture occur. We show that the weaker singularity can readily affect whether the crack will penetrate, or debond, the interface.

2.1 Introduction

It is well known that, for a crack in a homogeneous elastic material under the plane strain conditions, the singular stress field is a linear superposition of two modes, both having the exponent of ½. Despite its central importance in fracture mechanics, a crack in a homogeneous material is a particular case among many configurations of

bonded wedges of dissimilar elastic materials; see Akisanya and Fleck (1997), Reedy (2000), Mohammed and Liechti (2000) and Labossiere et al. (2002) for reviews of literature. For such a configuration, the singular stress field may still consist of two modes, but usually of *unequal exponents*, either a pair of complex conjugates, or two unequal real numbers. The two exponents may degenerate to one real number for special choices of the materials and the geometry, but a perturbation in the parameters characterizing the materials and the geometry often lifts the degeneracy, leading to two unequal exponents. Thus, unequal exponents are a rule rather than an exception.

The case of complex-conjugate exponents has been extensively discussed within the context of a crack lying on a bimaterial interface (e.g., Rice, 1988). This chapter will focus on the case that the two modes have unequal real exponents. That is, a stronger and a weaker singularity coexist, a situation known as the split singularities. It is sometimes suggested that the stronger singularity should be used to formulate failure criteria. However, Liu et al. (1999) have shown that the stronger singularity may dominate only within an exceedingly small zone, and argued that both singularities can be important. Labossiere et al. (2002) have included both modes in studying fracture initiated from a bimaterial corner.

This chapter aims to show the significance of the split singularities in a particular context. Figure 2-1 illustrates two elastic materials bonded at an interface, and a crack impinging upon the interface at angle ω, with the edge of the crack lying on the interface. For many combinations of the materials and the impinging angle, the two modes of the singular stress field have unequal real exponents (e.g., Bogy, 1971; Asbaugh, 1975; Fenner, 1976; Chen and Wang, 1996; Li et al., 1997). The impinging crack may either

penetrate across or debond the interface (Figure 2-2), a competition that has been extensively studied (e.g., Cook and Gordon, 1964; He and Hutchinson, 1989a; Thouless et al., 1989; Gupta et al., 1992; Martinez and Gupta, 1994; Lemaitre et al., 1996; Kovar et al., 1998; Davis et al., 2000; Leguillon et al., 2000 and 2001; Joyce et al., 2003; Roham et al., 2004; Parmigiani and Thouless, 2006). The effects of the split singularities on this competition, however, have never been considered. This chapter will show that the weaker singularity can readily alter the outcome of the penetration-debond competition.

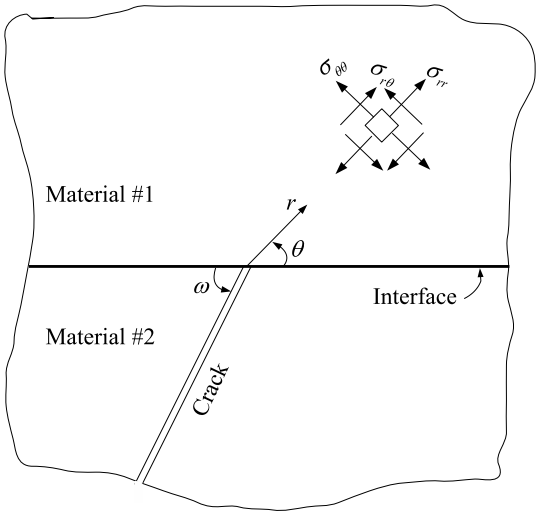

Figure 2-1:Two materials, #1 and #2, occupy two half spaces and are bonded at an interface. A crack pre-exists in material #2, impinging upon the interface at angle ω. The edge of the crack lies on the interface, and coincides with the *z*-axis of a polar coordinate system (r,θ,z).

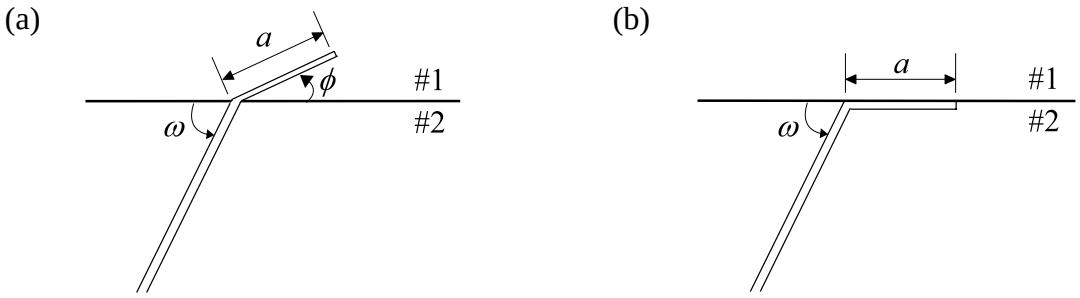

Figure 2-2:After a primary crack in material #2 hits the interface, the crack may go on to either (a) penetrate into material #1, or (b) debond the interface. The angle of penetration, ϕ, may be determined by the criterion that the penetrating crack is purely mode I. The length of the small cracks, *a*, may represent the size of flaws in material # 1 and on the interface.

2.2 Split singularities

To set the stage, this section describes the salient features of the singularities of a crack impinging on a bimaterial interface (Figure 2-1). The detailed solving procedure will be described in Section 2.7. When both materials are elastic and isotropic, for problems of this type Dundurs (1969) has shown that the stress field depends on elastic constants through two dimensionless parameters:

$$\alpha = \frac{\mu_1(1-\nu_2)-\mu_2(1-\nu_1)}{\mu_1(1-\nu_2)+\mu_2(1-\nu_1)}. \tag{2.1}$$

$$\beta = \frac{1}{2}\left[\frac{\mu_1(1-2\nu_2)-\mu_2(1-2\nu_1)}{\mu_1(1-\nu_2)+\mu_2(1-\nu_1)}\right]. \tag{2.2}$$

where μ is the shear modulus, and ν Poisson's ratio. The subscripts 1 and 2 refer to the

two materials, respectively. By requiring $0 \le \nu \le 0.5$ and $\mu > 0$, the Dundurs parameters are confined within a parallelogram in the (α, β) plane, with vertices at $(1, 0)$, $(1, 0.5)$, $(-1, 0)$ and $(-1, -0.5)$.

For the singular stress field around the edge of the crack, a component of the stress tensor, say $\sigma_{\theta\theta}$, takes the form of $\sigma_{\theta\theta} \sim r^{-\lambda}$. The exponent λ is a root of a transcendental equation given by Bogy (1971). The root is restricted as $0 < \mathrm{Re}(\lambda) < 1$, a restriction commonly adopted, with justifications critiqued by Hui and Ruina (1995) and Dunn et al. (2001). Depending on the Dundurs parameters α and β, as well as on the impinging angle ω, the solution of the exponent can be either two real numbers λ_1 and λ_2, or a pair of complex conjugates $\lambda_{1,2} = \xi \pm i\varepsilon$, where $i = \sqrt{-1}$.

For the impinging angle $\omega = 45^0$, for example, Figure 2-3 plots the contours of the exponents on the (α, β) plane. The parallelogram is divided into four regions by dark curves meeting at the center $\alpha = \beta = 0$. In the upper-left and lower-right regions, the exponents are real and unequal. The contours of larger exponent (λ_1) are labeled horizontally, and the contours of the smaller exponent (λ_2) are labeled vertically. When $\alpha < 0$, material #2 is stiffer than material #1, and $\lambda_1 > \lambda_2 \ge 0.5$. When $\alpha > 0$, material #1 is stiffer than material #2, and $\lambda_2 < \lambda_1 \le 0.5$. In the upper-right and lower-left regions, the exponents are a pair of complex conjugates, $\lambda_{1,2} = \xi \pm i\varepsilon$. The contours of the real part ξ are solid lines, and are strongly α-dependent. The contours of the imaginary part ε are dashed lines, and are strongly β-dependent. These four regions are separated by the four boundaries (i.e., the dark curves). At each point on the boundaries, the two

exponents degenerate to one number: when the point is approached from a region of real exponents, the two exponents become identical; when the point is approached from a region of complex-conjugate exponents, the imaginary part vanishes. At $\alpha = \beta = 0$, the two materials have the same elastic constants, and the two exponents are degenerate, $\lambda_1 = \lambda_2 = 0.5$, corresponding to the familiar two modes at the edge of a crack in a homogeneous material.

These contours change as the impinging angle ω varies. As a limiting case, first studied by Williams (1959), when the crack lies on the interface ($\omega = 0$), the exponents are a pair of complex conjugates:

$$\lambda_{1,2} = \frac{1}{2} \pm i \frac{1}{2\pi} \ln \frac{1-\beta}{1+\beta}. \tag{2.3}$$

In this case, the regions of complex conjugates expand to the whole (α, β) plane, except for the line $\beta = 0$, where $\lambda_1 = \lambda_2 = 0.5$. The interfacial crack has been extensively studied; see reviews by Rice (1988) and by Hutchinson and Suo (1992).

As another limiting case, first studied by Zak and Williams (1963), when the crack is perpendicular to the interface ($\omega = 90^0$), the two exponents degenerate to one real number, governed by the equation

$$\cos(\lambda\pi) = \frac{2(\beta-\alpha)}{(1+\beta)}(1-\lambda)^2 + \frac{\alpha+\beta^2}{1-\beta^2}. \tag{2.4}$$

Figure 2-4 plots the contours of λ on the (α, β) plane. In particular, the contour of $\lambda = 0.5$ is the straight line $\alpha = -\beta$. The crack perpendicularly impinges upon the interface has also been studied by other authors (e.g., Lu and Erdogan, 1983; Chen 1994; Kang and Lu, 2002; Nuller et al., 2006).

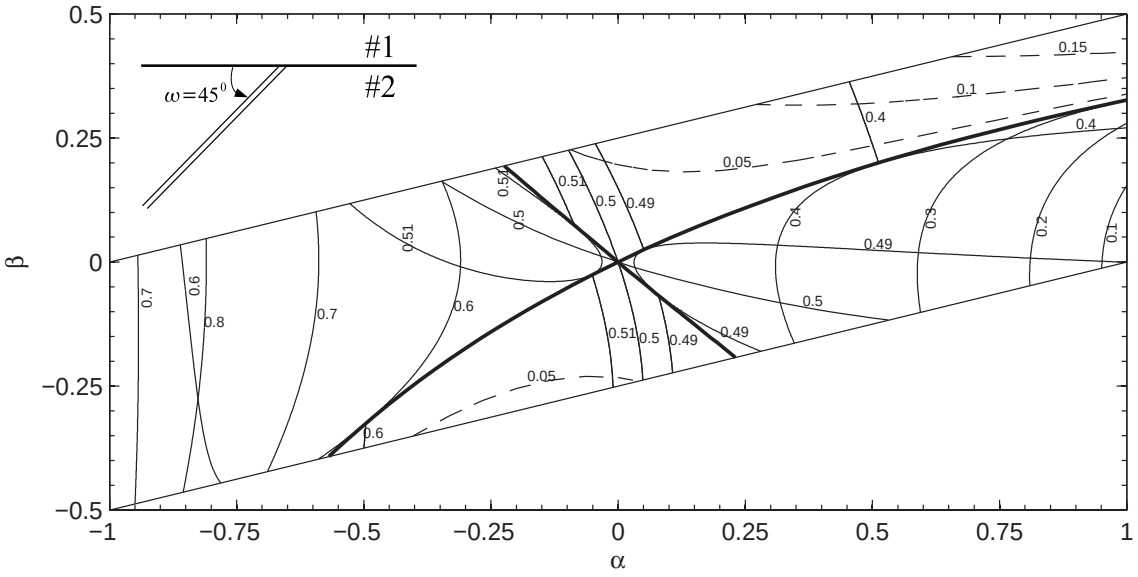

Figure 2-3:Contours of the exponents of the singular stress field around the tip of a crack impinging on the interface at angle $\omega = 45^0$, plotted on the plane of the Dundurs parameters (α, β), restricted in the parallelogram. The parallelogram is divided into four regions with the boundaries denoted by the dark curves. In the upper-left and lower-right regions, the exponents are two unequal real numbers, with the larger exponent λ_1 labeled horizontally, and the smaller exponent λ_2 labeled vertically. In the upper-right and lower-left regions, the exponents are a pair of complex conjugates, with the real part ξ plotted as solid lines, and the imaginary part ε as dashed lines. On the boundaries (the dark curves), the exponents of the two modes degenerate to one number.

When $\beta = 0$, the exponents are a pair of real numbers, regardless the values of α and ω. Figure 2-5 plots the exponents λ_1 and λ_2 as functions of the impinging angle ω, for two values of α. As ω changes from 0 to 90^0, the exponents degenerate to ½

when the crack lies on the interface, are two unequal numbers when the crack impinges upon the interface at an oblique angle, and degenerate again when the crack is perpendicular to the interface. Observe that the exponents vary significantly with the elastic mismatch and the impinging angle. As will become evident, the importance of the multiple modes should be assessed on a case-by case basis.

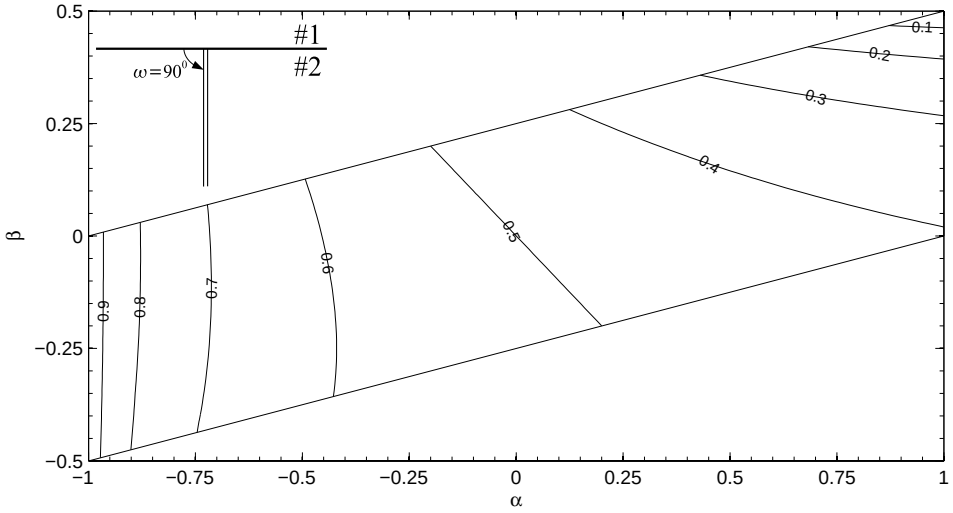

Figure 2-4:For a crack impinging perpendicularly on the interface, the two modes of the singular stress field have an identical exponent. Contours of the exponent are plotted on the plane of the Dundurs parameters (α, β).

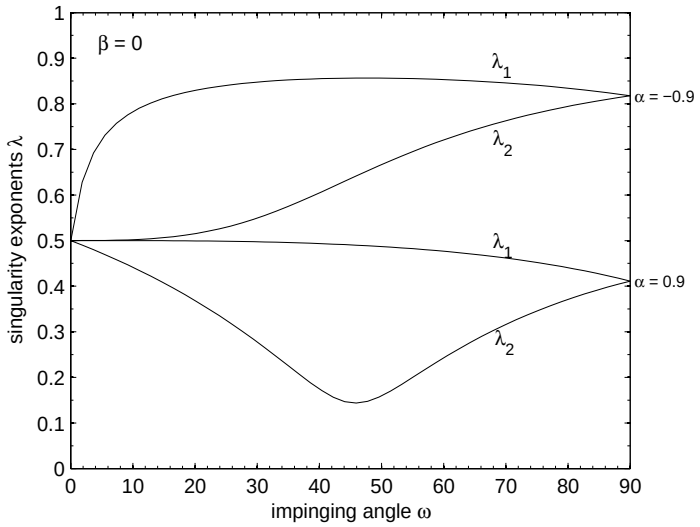

Figure 2-5:When $\beta = 0$, and for all values of α and the impinging angle ω, the two modes of the singular stress field are characterized by two real numbers, λ_1 and λ_2. The two exponents are plotted as functions of ω, for α = 0.9 and α = -0.9. The two exponents degenerate when the crack lies on the interface $(\omega = 0)$ and when the crack impinges perpendicularly to the interface $(\omega = 90^0)$.

2.3 Local mode mixity

In the remainder of this chapter, we will focus on the case of two unequal real exponents. As a reference, first recall the best-studied degenerate case: a crack in a homogeneous elastic material, for which the singular stress field is a linear superposition of two modes (e.g., Lawn, 1993):

$$\sigma_{ij}(r,\theta) = \frac{K_I}{\sqrt{2\pi r}}\Sigma_{ij}^{I}(\theta) + \frac{K_{II}}{\sqrt{2\pi r}}\Sigma_{ij}^{II}(\theta). \tag{2.5}$$

The plane of the crack is a plane of symmetry, with respect to which the mode I field is

symmetric and the mode II field is anti-symmetric. We adopt the conventional normalization: $\Sigma^{I}_{\theta\theta} = \Sigma^{II}_{r\theta} = 1$ directly ahead of the crack. The two modes have the same exponents, so that the proportion of the two modes is constant, independent of the distance from the edge of the crack, and can be specified by the ratio of the stress intensity factors, K_{II} / K_{I}.

For a crack impinging at an angle upon a bimaterial interface (Figure 2-1), when the exponents are unequal real numbers λ_1 and λ_2, the singular stress field around the edge of the crack is still a linear superposition of two modes:

$$\sigma_{ij}(r,\theta) = \frac{k_1}{(2\pi r)^{\lambda_1}} \Sigma^{1}_{ij}(\theta) + \frac{k_2}{(2\pi r)^{\lambda_2}} \Sigma^{2}_{ij}(\theta). \tag{2.6}$$

We adopt the normalization that directly ahead of the crack,

$$\Sigma^{1}_{\theta\theta}(\omega) = 1, \;\; \Sigma^{2}_{r\theta}(\omega) = 1. \tag{2.7}$$

When the two materials have different elastic constants, however, the plane of the crack is not a plane of symmetry, so that in general $\Sigma^{1}_{r\theta}(\omega) \neq 0$ and $\Sigma^{2}_{\theta\theta}(\omega) \neq 0$.

Note that one has to be careful to assess the suitability of the two-mode description, i.e., Equation (2.6), especially when the second mode is so weak that it may not be much different from the contribution of the non-singular modes. This aspect is not pursued in this chapter.

The two stress intensity factors, k_1 and k_2, have different dimensions, being $(\text{stress})(\text{lengh})^{\lambda_1}$ and $(\text{stress})(\text{lengh})^{\lambda_2}$, respectively. Figure 2-6 illustrates a representative boundary value problem, with T describing the applied stress, and L the length scale of the macroscopic geometry. Linearity and dimensional considerations dictate that the two stress intensity factors should take the form

$$k_1 = \kappa_1 T L^{\lambda_1}, \quad k_2 = \kappa_2 T L^{\lambda_2}. \tag{2.8}$$

where κ_1 and κ_2 are dimensionless coefficients.

Equation (2.6) suggests that, as the distance *r* from the edge of the crack varies, the proportion of the two modes also varies and can be specified by the dimensionless parameter $(k_2/k_1)r^{\lambda_1-\lambda_2}$ (Liu et al., 1999). This parameter is suitable to describe the mode mixity of the singular stress field, so long as an arbitrary length *r* is chosen, in the same spirit as Rice's (1988) suggestion for a crack lying on a bimaterial interface. Indeed, Labossiere et al. (2002) have used this mode mixity in describing their experimental data.

The singular stress field [Equation (2.6)] is obtained by assuming that the materials are elastic, and the geometry is perfect (Figure 2-1). Such assumptions are invalid in a process zone around the edge of the crack, either because the materials deforms plastically, or because the geometry is imperfect. Let Λ be the size of the process zone, within which the singular stress field is invalid. Also, the singular stress field is invalid at size scale *L*, where the external boundary conditions will change the stress distribution. However, provided the process zone is significantly smaller than the macroscopic length, $\Lambda << L$, the singular stress field [Equation (2.6)] prevails within an annulus, known as the *k*-annulus, of some radii bounded between Λ and *L*.

The microscopic processes of fracture occur within the process zone, but are driven by the singular stress field in the *k*-annulus. In discussing the effect of the mode mixity on failure processes, it is intuitive to select the length characterizing the size of the process zone, i.e., setting $r = \Lambda$. Thus, we specify a dimensionless parameter

$$\eta = (k_2/k_1)\Lambda^{\lambda_1-\lambda_2} = (\kappa_2/\kappa_1)(\Lambda/L)^{\lambda_1-\lambda_2}. \tag{2.9}$$

This parameter, to be called the *local mode mixity*, measures the relative contribution of

the two modes to the stress field at length scale Λ. The parameter η combines the effects of the loading mixity κ_2/κ_1, the length ratio Λ/L, and the difference of the two exponents λ_1 and λ_2.

As an illustration, consider a loading condition that $\kappa_2/\kappa_1 = 1$, so that the local mode mixity reduces to $\eta = (\Lambda/L)^{\lambda_1-\lambda_2}$, which is plotted in Figure 2-6 for the case $\omega = 45^0$ and $\beta = 0$. When the elastic mismatch is small (e.g., $\alpha = 0$), the two modes make comparable contributions for all values of Λ/L. When the elastic mismatch is modest (e.g., $\alpha = 0.5$), the two modes make comparable contributions if Λ/L is modest, but the weaker singularity makes a smaller contribution if $\Lambda/L << 1$. When the elastic mismatch is large (e.g., $\alpha = 0.9$), the weaker singularity makes negligible contribution so long as Λ is reasonably small compared to *L*.

As another example, consider a well-bonded interface of two brittle materials, e.g., a thin film epitaxially grown on a substrate. The process zone is taken to be some multiple of atomic dimension, say $\Lambda = 1\text{nm}$. Take *L* as the thickness of a film, say *L* = 100 nm. For a modest elastic mismatch, we may take $\lambda_1 - \lambda_2 = 0.2$ and $(\Lambda/L)^{\lambda_1-\lambda_2} = 0.4$. Consequently, a modest value of κ_2/κ_1 will bring the local mode mixity η to the order of unity.

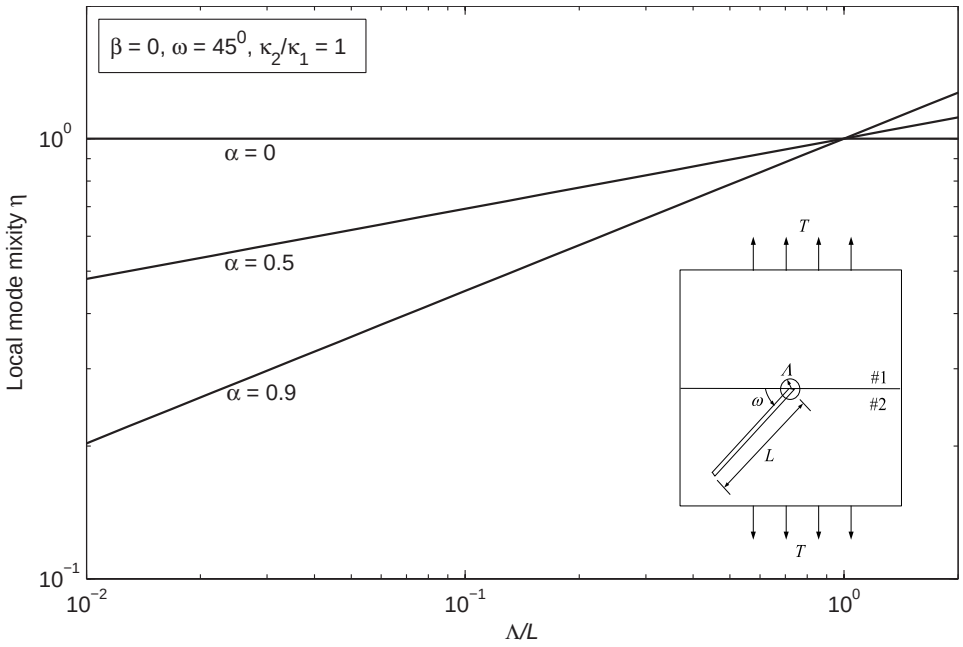

Figure 2-6:Inset illustrates a representative boundary value problem, with a macroscopic length L, an applied stress T, and a microscopic length Λ that characterizes the size of a zone in which processes of fracture occur. The proportion of the two modes of the singular stress field at length scale Λ is characterized by the local mode mixity, $\eta = (\kappa_2/\kappa_1)(\Lambda/L)^{\lambda_1-\lambda_2}$; see the body of the chapter for interpretation. The parameter η is plotted as a function of Λ/L for three values of α.

2.4 The competition between penetration and debond

We now analyze the effects of the split singularities on the penetrating and debonding cracks. For simplicity, we will take $\beta = 0$, so that the singular stress field for the crack impinging upon the interface is a superposition of two modes of unequal real exponents, i.e., Equation (2.6), with the stress intensity factors k_1 and k_2 given by Equation (2.8). The length Λ now is identified with the length a of the small cracks in

Figure 2-2, so that the local mode mixity is defined as $\eta = (\kappa_2 / \kappa_1)(a/L)^{\lambda_1 - \lambda_2}$.

2.4.1 Penetration

Consider the case that the impinging crack penetrates across the interface (Figure 2-2a). The size of the penetrating crack, *a*, is taken to be small compared to the macroscopic length scale *L*. The stress field around the edge of the penetrating crack is square-root singular, with the regular stress intensity factors K_I^p and K_{II}^p. At a distance much larger than *a*, in the *k*-annulus, the singular stress field [Equation (2.6)] prevails, with the stress intensity factors k_1 and k_2. Linearity and dimensional considerations relate the two sets of the stress intensity factors, (K_I^p, K_{II}^p) and (k_1, k_2), as

$$\frac{K_I^p}{\sqrt{a}} = b_{11} \cdot \frac{k_1}{a^{\lambda_1}} + b_{12} \cdot \frac{k_2}{a^{\lambda_2}}. \tag{2.10}$$

$$\frac{K_{II}^p}{\sqrt{a}} = b_{21} \cdot \frac{k_1}{a^{\lambda_1}} + b_{22} \cdot \frac{k_2}{a^{\lambda_2}}. \tag{2.11}$$

The coefficients b_{11}, b_{12}, b_{21} and b_{22} are dimensionless functions of the Dundurs parameter α, the impinging angle ω, and the penetrating angle ϕ. These coefficients are calculated using the finite element method (Section 2.9), and are listed in Table 2-1 for $\alpha = -0.5$, Table 2-2 for $\alpha = 0$ and Table 2-3 for $\alpha = 0.5$, respectively.

Taking the ratio of Equations (2.11) and (2.10), we obtain the mode angle of the penetrating crack, ψ^p, given by

$$\tan\psi^p = \frac{K_{II}^p}{K_I^p} = \frac{b_{21} + b_{22}\eta}{b_{11} + b_{12}\eta}. \tag{2.12}$$

Figure 2-7 plots the mode angle ψ^p as a function of the penetrating angle, ϕ, for

somevalues of η and α, with $\beta = 0$ and $\omega = 45^0$. We require that $K_I^p > 0$, i.e., $k_1 a^{1/2-\lambda_1}\left(b_{11} + b_{12} \cdot \eta\right) > 0$. When the two materials have dissimilar elastic constants, k_1 no longer stands for the stress intensity factor of opening mode, so it may be either positive or negative. In this chapter, we adopt $k_1 > 0$ for the presentation of the results.

If the toughness of material #1 is anisotropic, a cleavage plane may set the penetrating angle ϕ. If the toughness of material #1 is isotropic, however, the penetrating angle ϕ may be selected by requiring that the penetrating crack be purely mode I, namely, $K_{II}^p = 0$. Such a penetrating angle, denoted by ϕ^*, corresponds to the intersection of a curve in Figure 2-7 with the horizontal line $\psi^p = 0$. For example, if the contribution of k_2 is neglected, i.e., $\eta = 0$, the impinging crack prefers to deflect onto the interface when $\alpha \geq 0.5$ (Figure 2-7c), as stated in He and Hutchinson (1989a). When k_2 is included, however, the crack may penetrate across the interface.

Figure 2-8 plots penetrating angle ϕ^* as a function of the local mode mixity η. For the curve that the two materials have the same elastic constants, our results match well with those of Hayashi and Nemat-Nasser (1981) and He and Hutchinson (1988, 1989b). When $\eta = 0$, the impinging crack is under mode I loading and penetrates straight ahead, $\phi^* = 45^0$. When, $\eta > 0$ the impinging crack is under a mixed mode condition and may penetrate across the interface at an angle $\phi^* < 45^0$. When $\eta > 0.545$, however, ϕ^* becomes negative, so that the impinging crack can no longer penetrate across the interface. This feature is also observed for the case of $\alpha = 0.5$, where ϕ^* becomes negative when $\eta > 0.05$.

Table 2-1: Coefficients b_{11}, b_{12}, b_{21}, b_{22} in the range of $5^0 \le \phi \le 170^0$ for $\alpha = -0.5$ with $\beta = 0$ and $\omega = 45^0$.

	$\alpha = -0.5$			
ϕ (deg)	b_{11}	b_{12}	b_{21}	b_{22}
5	-0.640	3.525	-1.268	-0.798
10	-0.486	3.617	-1.359	-0.642
20	-0.153	3.737	-1.488	-0.282
30	0.205	3.759	-1.548	0.114
40	0.568	3.679	-1.537	0.517
45	0.747	3.601	-1.506	0.712
50	0.920	3.498	-1.458	0.900
60	1.246	3.224	-1.314	1.240
70	1.530	2.874	-1.115	1.516
80	1.761	2.466	-0.873	1.713
90	1.931	2.022	-0.600	1.823
100	2.035	1.565	-0.311	1.844
110	2.072	1.121	-0.024	1.780
120	2.044	0.707	0.251	1.642
130	1.957	0.338	0.501	1.445
140	1.818	0.028	0.715	1.209
150	1.630	-0.222	0.889	0.947
160	1.411	-0.405	1.015	0.690
170	1.161	-0.531	1.090	0.446

Table 2-2: Coefficients b_{11}, b_{12}, b_{21}, b_{22} in the range of $5^0 \le \phi \le 170^0$ for $\alpha = 0$ with $\beta = 0$ and $\omega = 45^0$.

	$\alpha = 0$			
ϕ (deg)	b_{11}	b_{12}	b_{21}	b_{22}
5	0.840	0.921	-0.291	0.652
10	0.876	0.831	-0.264	0.728
20	0.935	0.624	-0.199	0.856
30	0.978	0.387	-0.124	0.948
40	0.999	0.131	-0.042	0.995
45	1.002	0.000	0.000	1.002
50	0.999	-0.131	0.042	0.996
60	0.978	-0.387	0.124	0.949
70	0.935	-0.625	0.199	0.859
80	0.876	-0.832	0.264	0.731
90	0.801	-1.003	0.315	0.574
100	0.715	-1.128	0.350	0.399
110	0.623	-1.206	0.369	0.217
120	0.528	-1.236	0.371	0.039
130	0.435	-1.221	0.358	-0.124
140	0.347	-1.165	0.331	-0.264
150	0.266	-1.075	0.294	-0.375
160	0.197	-0.960	0.250	-0.449
170	0.138	-0.828	0.202	-0.486

Table 2-3: Coefficients b_{11}, b_{12}, b_{21}, b_{22} in the range of $5^0 \le \phi \le 170^0$ for $\alpha = 0.5$ with $\beta = 0$ and $\omega = 45^0$.

	$\alpha = 0.5$			
ϕ (deg)	b_{11}	b_{12}	b_{21}	b_{22}
5	1.418	1.098	-0.007	0.886
10	1.412	0.954	0.054	0.970
20	1.381	0.631	0.159	1.121
30	1.322	0.269	0.252	1.221
40	1.240	-0.112	0.331	1.258
45	1.191	-0.302	0.364	1.252
50	1.138	-0.490	0.393	1.229
60	1.022	-0.848	0.438	1.137
70	0.897	-1.166	0.465	0.989
80	0.769	-1.430	0.474	0.798
90	0.642	-1.630	0.466	0.578
100	0.519	-1.761	0.442	0.345
110	0.406	-1.821	0.406	0.119
120	0.303	-1.815	0.360	-0.089
130	0.213	-1.750	0.307	-0.263
140	0.137	-1.638	0.250	-0.392
150	0.076	-1.491	0.190	-0.470
160	0.030	-1.327	0.133	-0.491
170	-0.002	-1.157	0.080	-0.461

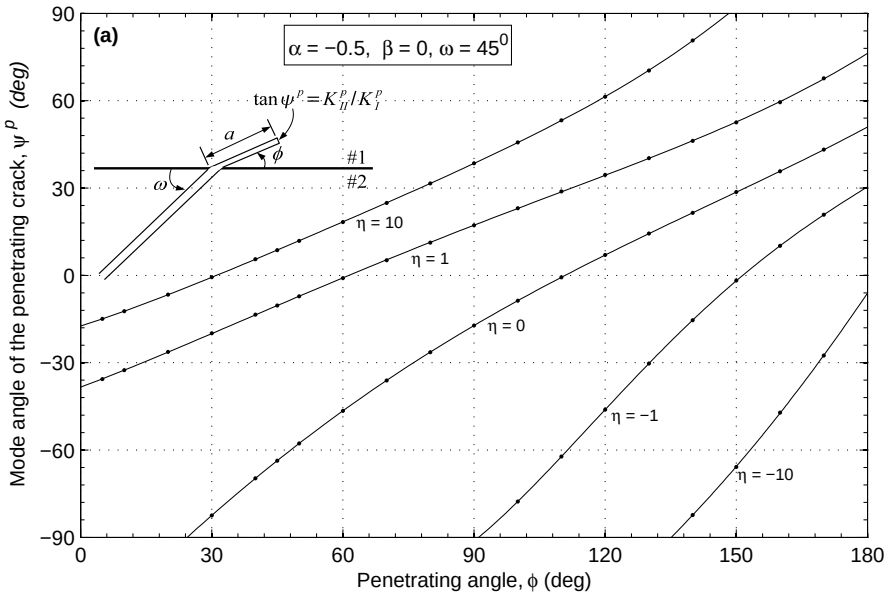

Figure 2-7(a):Mode angle of a penetrating crack, ψ^p, is plotted as a function of the penetrating angle ϕ, for several values of the local mode mixity η for $\alpha = -0.5$.

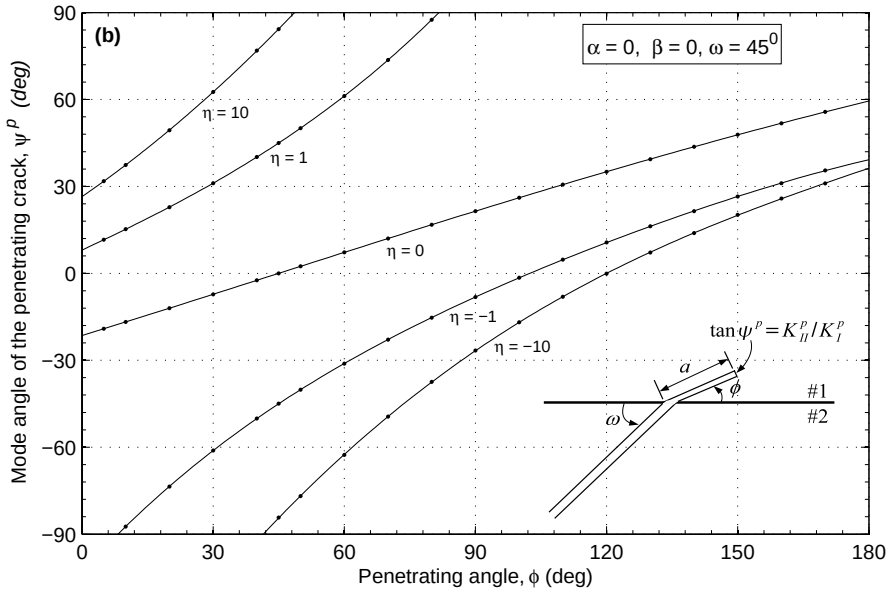

Figure 2-7(b):Mode angle of a penetrating crack, ψ^p, is plotted as a function of the penetrating angle ϕ, for several values of the local mode mixity η for $\alpha = 0$.

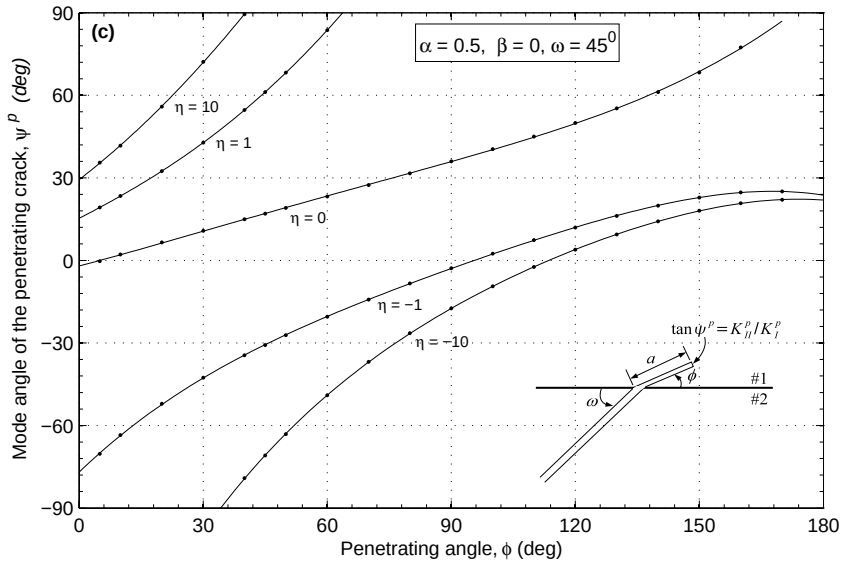

Figure 2-7(c):Mode angle of a penetrating crack, ψ^p, is plotted as a function of the penetrating angle ϕ, for several values of the local mode mixity η for $\alpha = +0.5$.

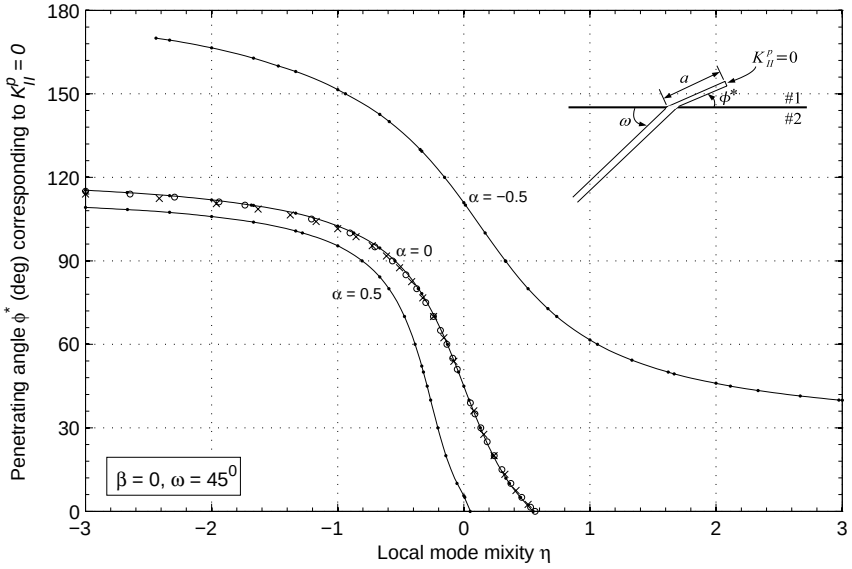

Figure 2-8:Penetrating angle ϕ^* corresponding to $K_{II}^p = 0$ is plotted as a function of the local mode mixity η. For the case of $\alpha = 0$, the results by Hayashi and Nemat-Nasser (1981) are marked by crosses, and those by He and Hutchinson (1988,1989b) by open circles.

2.4.2 Debond

We next consider the case that the impinging crack causes the interface to debond (Figure 2-2b). When $\beta = 0$, the stress field at the edge of the interfacial crack is square-root singular, with the regular stress intensity factors, $\left(K_I^d, K_{II}^d\right)$. They relate to the stress intensity factors of the impinging crack $\left(k_1, k_2\right)$ as

$$\frac{K_I^d}{\sqrt{a}} = c_{11} \cdot \frac{k_1}{a^{\lambda_1}} + c_{12} \cdot \frac{k_2}{a^{\lambda_2}}. \tag{2.13}$$

$$\frac{K_{II}^d}{\sqrt{a}} = c_{21} \cdot \frac{k_1}{a^{\lambda_1}} + c_{22} \cdot \frac{k_2}{a^{\lambda_2}}. \tag{2.14}$$

The dimensionless parameters c_{11}, c_{12}, c_{21} and c_{22} are functions of α and ω. The results calculated using the finite element method are listed in Table 2-4. For the case of $\alpha = 0$, we can compare our results with those of He and Hutchinson (1988), and the difference is within 2%.

Taking the ratio of Equations (2.14) and (2.13), we obtain the mode angle of the debonding crack, ψ^d, as given by

$$\tan\psi^d = \frac{K_{II}^d}{K_I^d} = \frac{c_{21} + c_{22}\eta}{c_{11} + c_{12}\eta}. \tag{2.15}$$

Figure 2-9 plots the mode angle of the debond crack, ψ^d as a function of the local mode mixity η for $\alpha = -0.5$, 0, 0.5, with $\beta = 0$ and $\omega = 45^0$.

Table 2-4: Coefficients c_{11}, c_{12}, c_{21} and c_{22} for different α with $\beta = 0$ and $\omega = 45^0$.

α	-0.5	0	0.5
c_{11}	-0.859	0.801	0.989
c_{12}	4.248	0.999	0.924
c_{21}	-1.466	-0.315	-0.166
c_{22}	-0.852	0.571	0.493

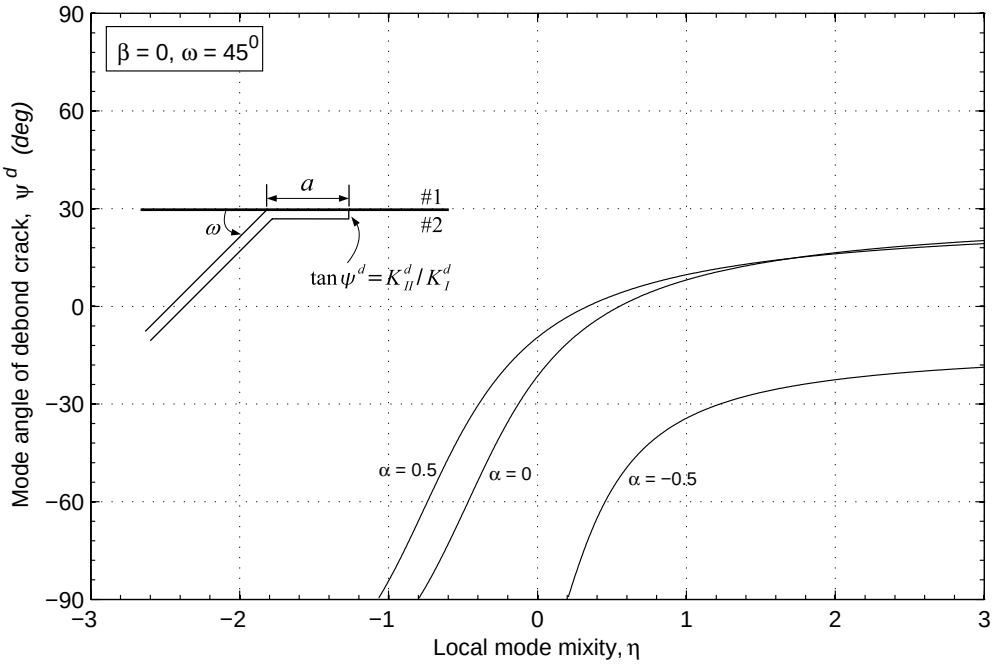

Figure 2-9:Mode angle of the debond crack, ψ^d, is plotted as a function of local mode mixity η.

2.4.3 The competition between penetration and debond

For the penetrating crack, the energy release rate relates to the stress intensity factors as (Irwin 1957)

$$G^p = \frac{(1-\nu_1)}{2\mu_1}\left[\left(K_I^p\right)^2 + \left(K_{II}^p\right)^2\right]. \tag{2.16}$$

For the interfacial crack, the energy release rate relates to the stress intensity factors as (Malyshev and Salganik, 1965)

$$G^d = \left(\frac{1-\nu_1}{4\mu_1} + \frac{1-\nu_2}{4\mu_2}\right)\left[\left(K_I^d\right)^2 + \left(K_{II}^d\right)^2\right]. \tag{2.17}$$

The ratio of the energy release rate of the debonding crack to that of the penetrating crack is

$$\frac{G^d}{G^p} = \frac{1}{1-\alpha}\cdot\frac{\left(c_{11}^2 + c_{21}^2\right) + 2\left(c_{11}c_{12} + c_{21}c_{22}\right)\eta + \left(c_{12}^2 + c_{22}^2\right)\eta^2}{\left(b_{11}^2 + b_{21}^2\right) + 2\left(b_{11}b_{12} + b_{21}b_{22}\right)\eta + \left(b_{12}^2 + b_{22}^2\right)\eta^2}\ . \tag{2.18}$$

Here we have assumed that the sizes of flaws in material #1 and on the interface take the same value *a*. The mode angle of the penetration crack is selected by requiring $K_{II}^p = 0$, as discussed above. Figure 2-10 plots the ratio G^d / G^p as a function of η for $\alpha = -0.5$, 0, 0.5 with $\beta = 0$ and $\omega = 45^0$. For each value of α, the curve is limited in an interval of η to ensure that both the penetrating crack and the debonding crack are open, i.e., $K_I^p > 0$ and $K_I^d > 0$. For the case $\alpha = 0$, we have confirmed our results with those of Hayashi and Nemat-Nasser (1981) and He and Hutchinson (1988, 1989b).

Let Γ_1 be the fracture energy of material #1 under the mode I condition, and Γ_i be the fracture energy of the interface at the mode angle ψ^d. If $\Gamma_i / \Gamma_1 > G^d / G^p$, the impinging crack will penetrate across the interface, rather than debond the interface.

Otherwise, the impinging crack will debond the interface, rather than penetrate across the interface.

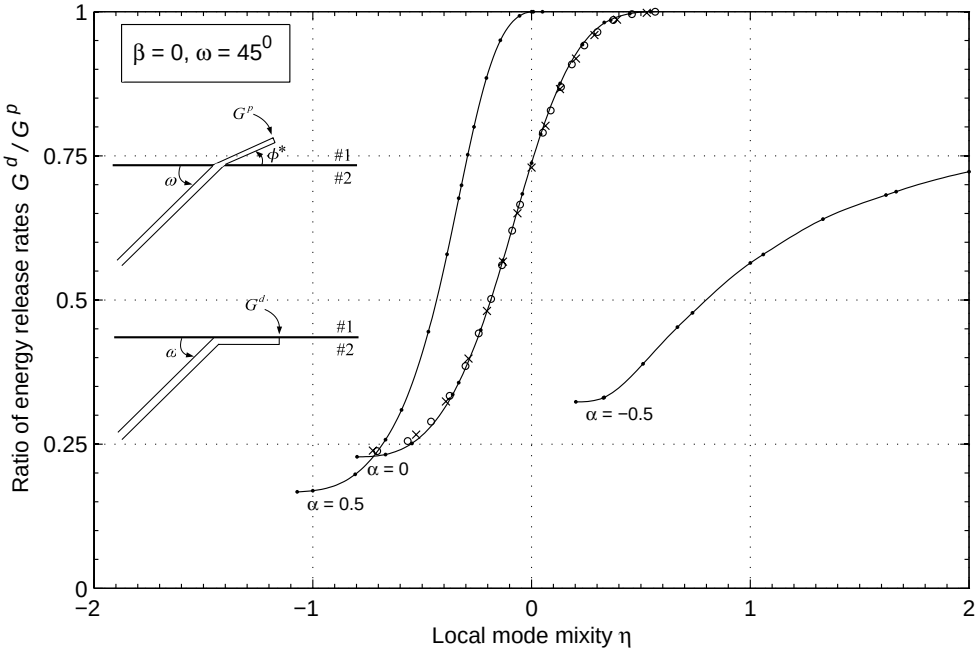

Figure 2-10:Ratio of the energy release rate of the debond crack, G^d, to the energy release rate of the penetration crack, G^p, is plotted as a function of the local mode mixity η. For the case of $\alpha = 0$, the results by Hayashi and Nemat-Nasser (1981) are marked by crosses, and those by He and Hutchinson (1988,1989b) by open circles.

2.5 Discussions

2.5.1 Will the weaker singularity affect the competition between penetration and debond?

The relative magnitude of the two modes of singularities is characterized by the local mode mixity $\eta = (\kappa_2 / \kappa_1)(a/L)^{\lambda_1 - \lambda_2}$. Thus, the effect of the weaker singularity on the penetration-debond competition will depend on how sensitive the competition depends on η, and on how large η is. We next address these two questions.

The local mode mixity η affects the penetration-debond competition in two ways. First, η affects the mode angle of the debonding crack (Figure 2-9). The mode angle, in its turn, affects the fracture energy of the interface (e.g., Hutchinson and Suo, 1992). Second, η affects the ratio G^d / G^p (Figure 2-10). Consequently, the weaker singularity may readily alter the outcome of the penetration-debond competition, provided the local mode mixity η is not too small.

The value of η will depend on the ratio κ_2 / κ_1, which in turn depends on the external geometry and loads. In practice, the ratio κ_2 / κ_1 can be anywhere from $-\infty$ to ∞. When the elastic constants of the two materials are not too different, the two exponents will be nearly the same, so that $(a/L)^{\lambda_1 - \lambda_2} \approx (a/L)^0 = 1$, and the local mode mixity reduces to the mode mixity for a crack in a homogeneous material, $\eta = \kappa_2 / \kappa_1$. When the elastic constants of the two materials are very different, however, the local mode mixity will vary with *a/L*, as illustrated in Figure 2-6. If *a* is much smaller than *L*, so that $\eta << 1$, then the weaker singularity should have little effect on the penetration-debond

competition, in which case the value of a is irrelevant. On the other hand, if η is large, then the value of a influences the outcome of the competition. In this case, because the flaw size is statistical, we expect that the outcome of the competition is also statistical.

2.5.2 Alternative models and interpretations of Λ

Following He and Hutchinson (1989a), we have assumed that (i) small cracks, of some length a, pre-exists on the interface and in material #1, and (ii) the materials are elastic to the scale somewhat below a, so that fracture mechanics can be applied to the small cracks. These assumptions may not be valid in applications. For example, the material and the bonding may be of such a high quality that no small cracks are present in the zone of influence of the impinging crack. In such a case, if the materials are elastic to some size scale, we may directly use the stress field [Equation (6)] to estimate the stresses just outside the inelastic zone. Thus, the parameter $\eta = (\kappa_2/\kappa_1)(\Lambda/L)^{\lambda_1-\lambda_2}$ still characterizes the mode mixity at the length scale of the inelastic zone, but with Λ interpreted as the size of the inelastic zone. To determine whether the crack will penetrate across, or debond, the interface, the ratio of the strength of the interface and the strength of the material may be compared with the ratio of the corresponding stresses predicted from Equation (6) at distance $r = \Lambda$. Such a stress-based model has long been used (e.g., Cook and Gordon, 1964, Gupta et al., 1992), and can be extended to include the effect of the split singularities.

As another example, the inelastic zone may be large compared to the small cracks, but still small compared to the macroscopic length L. In such a case, one may include

inelastic process explicitly in the model. One approach is to use cohesive laws to represent the fracture process in materials and on the interface (Mohammed and Liechti, 2000; Parmigiani and Thouless, 2006). In such a model, Λ may be identified as $\Lambda = E\Gamma / S^2$, where E is Young's modulus of a material, Γ the fracture energy, and S the theoretical strength. Even in such a case, the notion of split singularities is still important, as they set the mode mixity at the relevant length scale.

2.5.3 The size of the flaw on the interface may be different from that in the material.

In reaching Equation (18), we have assumed that the flaws on the interface and in material #1 have an equal size. In reality, these flaws may have different sizes, say, a^d and a^p, respectively. Consequently, Equations (16) and (17) leads to

$$\frac{G^d}{G^p} = \frac{1}{1-\alpha} \cdot \frac{\left(c_{11}^2 + c_{21}^2\right) + 2\left(c_{11}c_{12} + c_{21}c_{22}\right)\eta^d + \left(c_{12}^2 + c_{22}^2\right)\left(\eta^d\right)^2}{\left(b_{11}^2 + b_{21}^2\right) + 2\left(b_{11}b_{12} + b_{21}b_{22}\right)\eta^p + \left(b_{12}^2 + b_{22}^2\right)\left(\eta^p\right)^2} \left(\frac{a^d}{a^p}\right)^{1-2\lambda_1} . \qquad (2.19)$$

If the elastic mismatch of the two materials is not extremely large, λ_1 will be not too far from ½ and the difference in λ_1 and λ_2 is not too large; see Figures 2-3, 2-4 and 2-5. Consequently, for a modest difference in a^d and a^p, $\left(a^d / a^p\right)^{1-2\lambda_1} \approx 1$ and $\eta^d / \eta^p = \left(a^d / a^p\right)^{\lambda_1 - \lambda_2} \approx 1$, so that (2.19) reduces to (2.18). On the other hand, when the elastic mismatch or the difference in a^d and a^p is large, one should use Equation (2.19) instead of (2.18). In this case, because the flaw sizes are usually unknown, the outcome of penetration-debond competition should be statistical.

2.5.4 The case of exponents being a pair of complex conjugates

In the above, we have focused on the case that the exponents are two distinct real numbers. When the exponents are complex conjugates, $\lambda_{1,2} = \xi \pm i\varepsilon$, we write the stress field around the crack tip as

$$\sigma_{ij}(r,\theta) = \frac{\mathrm{Re}\left(kr^{i\varepsilon}\right)}{(2\pi r)^{\xi}}\Sigma_{ij}^{1}(\theta) + \frac{\mathrm{Im}\left(kr^{i\varepsilon}\right)}{(2\pi r)^{\xi}}\Sigma_{ij}^{2}(\theta). \tag{2.20}$$

where the complex stress intensity factor *k*, of the dimension $[stress][length]^{\xi - i\varepsilon}$, is defined such that the angular functions $\Sigma_{ij}^{1}(\theta)$ and $\Sigma_{ij}^{2}(\theta)$ satisfy Equation (2.6). For a representative boundary value problem illustrated in the inset of Figure 2-6, linearity and dimensional considerations dictate that the two stress intensity factors should take the form

$$k = \kappa T L^{\xi - i\varepsilon} \exp(i\Psi). \tag{2.21}$$

where κ and Ψ are dimensionless real numbers. Inspecting (2.20) and (2.21), we may measure the relative contribution of the two modes to the stress field at the scale of the process zone size *a* by the ratio

$$\eta' = \frac{\mathrm{Im}\left(ka^{i\varepsilon}\right)}{\mathrm{Re}\left(ka^{i\varepsilon}\right)} = \tan\left(\Psi + \varepsilon \ln\frac{a}{L}\right). \tag{2.22}$$

Treatment along this line would be analogous to that of Rice (1988) for a crack lying on an interface. Many of his comments, including those on the solution of Comninou (1977), should apply. It is possible to study the significance of this local mode mixity on the penetration-debond completion by following the approach developed in this chapter, which we will not pursue here.

2.6 Summary

The singular stress field around the edge of a crack impinging on a bimaterial interface is a linear superposition of two modes, often of unequal exponents, λ_1 and λ_2. So long as the process zone size Λ is small compared with the macroscopic length *L*, the singular field prevails in an annulus of some radii bounded between Λ and *L*. We characterize the proportion of the two modes at the size scale Λ by a dimensionless parameter, $\eta = (\kappa_2 / \kappa_1)(\Lambda / L)^{\lambda_1 - \lambda_2}$, called the local mode mixity. We show that the weaker singularity may readily affect whether the crack will penetrate across, or debond, the interface. Because the split singularities occur in many configurations of cracks and wedges, the approach outlined in this chapter may find broad applications.

2.7 Appendix A: Solving procedure of eigenvalue problem

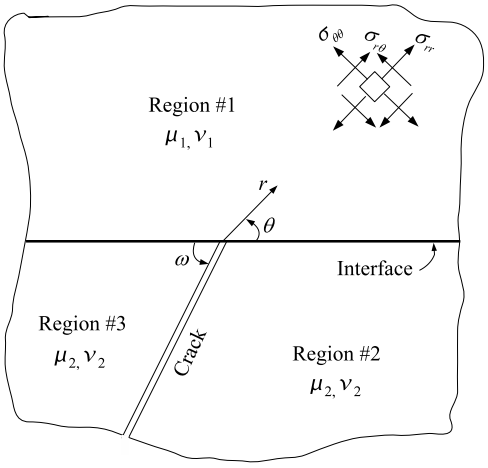

Figure 2-11: A semi-infinite crack impinging on the bimaterial interface.

Airy stress functions are used to solve this linear elastic problem. Let (r,θ) be polar coordinates centered at the crack tip. The Airy function ϕ is biharmonic, i.e., $\nabla^2\nabla^2\phi = 0$. And then the stresses can be expressed by

$$\sigma_{rr} = \frac{1}{r^2}\frac{\partial^2\phi}{\partial\theta^2} + \frac{1}{r}\frac{\partial\phi}{\partial r} \tag{2.23}$$

$$\sigma_{\theta\theta} = \frac{\partial^2\phi}{\partial r^2} \tag{2.24}$$

$$\tau_{r\theta} = -\frac{\partial}{\partial r}\left(\frac{1}{r}\frac{\partial\phi}{\partial\theta}\right) \tag{2.25}$$

The function ψ is harmonic, i.e. $\nabla^2\psi = 0$, and relates to ϕ by

$$\nabla^2\phi = \frac{\partial}{\partial r}\left(r\frac{\partial\psi}{\partial\theta}\right) \tag{2.26}$$

And the displacements can be expressed by

$$2\mu\, u_r = -\frac{\partial\phi}{\partial r} + \frac{1}{4}(1+\kappa)\, r\frac{\partial\psi}{\partial\theta} \tag{2.27}$$

$$2\mu\, u_\theta = -\frac{1}{r}\frac{\partial\phi}{\partial\theta} + \frac{1}{4}(1+\kappa)\, r^2\frac{\partial\psi}{\partial r} \tag{2.28}$$

where $\kappa = (3-\nu)/(1+\nu)$ for plane stress and $\kappa = 3-4\nu$ for plane strain. The symbols μ and ν are shear modulus and Poisson's ratio.

The Airy stress functions are chosen of a separable form:

$$\phi = r^{-\lambda+2}F(\theta) \tag{2.29}$$

And $$\psi = r^{-\lambda}G(\theta) \tag{2.30}$$

Note that Laplacian operator is $\nabla^2 = \partial^2/\partial r^2 + (1/r)\partial/\partial r + (1/r^2)\partial^2/\partial\theta^2$ in polar coordinates, and so

$$\nabla^2\nabla^2\phi = r^{-\lambda-2}\left[\lambda^2+\frac{d^2}{d\theta^2}\right]\left[(\lambda-2)^2+\frac{d^2}{d\theta^2}\right]F(\theta)=0\,. \tag{2.31}$$

$$\nabla^2\psi = r^{-\lambda-2}\left[\lambda^2+\frac{d^2}{d\theta^2}\right]G(\theta)=0 \quad (2.32) \tag{2.32}$$

Eqs.(6) and (7) satisfy for arbitrary r, so

$$\left[\lambda^2+\frac{d^2}{d\theta^2}\right]\left[(\lambda-2)^2+\frac{d^2}{d\theta^2}\right]F(\theta)=0 \tag{2.33}$$

$$\left[\lambda^2+\frac{d^2}{d\theta^2}\right]G(\theta)=0 \tag{2.34}$$

Assume $F(\theta)=\exp(\xi\theta)$, and so the eigenvalues are $\xi=\pm i\lambda$ and $\xi=\pm i(\lambda-2)$, and so the solution of $F(\theta)$ can be expressed as follows:

$$F(\theta)=A\sin(\lambda-2)\theta+B\cos(\lambda-2)\theta+C\sin\lambda\theta+D\cos\lambda\theta \tag{2.35}$$

Assume $G(\theta)=\exp(\zeta\theta)$, and so the eigenvalues are $\zeta=\pm i\lambda$, and on account of Equation(2), the solution of $G(\theta)$ can be expressed as follows:

$$G(\theta)=\frac{4}{\lambda}(D\sin\lambda\theta-C\cos\lambda\theta) \tag{2.36}$$

The constants *A, B, C* and *D* are to be determined by boundary conditions. The stresses relate to the Airy function as follows:

$$\sigma_{rr}=r^{-\lambda}\left[F''(\theta)-(\lambda-2)F(\theta)\right] \tag{2.37}$$

$$\sigma_{\theta\theta}=r^{-\lambda}(\lambda-1)(\lambda-2)F(\theta) \tag{2.38}$$

$$\tau_{r\theta}=r^{-\lambda}(\lambda-1)F'(\theta) \tag{2.39}$$

The displacements are given by

$$2\mu u_r=r^{-\lambda+1}\left[(\lambda-2)F(\theta)+\frac{1+\kappa}{4}G'(\theta)\right] \tag{2.40}$$

$$2\mu u_\theta = r^{-\lambda+1}\left[-F'(\theta)-\frac{1+\kappa}{4}\lambda G(\theta)\right] \tag{2.41}$$

That is,

$$\sigma_{rr} = -r^{-\lambda}(\lambda-1)\begin{Bmatrix}(\lambda-2)\left[A\ \sin(\lambda-2)\theta + B\ \cos(\lambda-2)\theta\right]..\\ +(\lambda+2)\left[C\ \sin\lambda\theta + D\ \cos\lambda\theta\right]\end{Bmatrix} \tag{2.42}$$

$$\sigma_{\theta\theta} = r^{-\lambda}(\lambda-2)(\lambda-1)\begin{bmatrix}A\ \sin(\lambda-2)\theta + B\ \cos(\lambda-2)\theta...\\ +C\ \sin\lambda\theta + D\ \cos\lambda\theta\end{bmatrix} \tag{2.43}$$

$$\tau_{r\theta} = r^{-\lambda}(\lambda-1)\begin{Bmatrix}(\lambda-2)\left[A\ \cos(\lambda-2)\theta - B\ \sin(\lambda-2)\theta\right]..\\ +\lambda\left[C\ \cos\lambda\theta - D\ \sin\lambda\theta\right]\end{Bmatrix} \tag{2.44}$$

$$u_r = \frac{r^{-\lambda+1}}{2\mu}\begin{Bmatrix}(\lambda-2)\left[A\ \sin(\lambda-2)\theta + B\ \cos(\lambda-2)\theta\right].\\ +(\lambda+\kappa-1)\left[C\ \sin\lambda\theta + D\ \cos\lambda\theta\right]\end{Bmatrix} \tag{2.45}$$

$$u_\theta = \frac{r^{-\lambda+1}}{2\mu}\begin{Bmatrix}(\lambda-2)\left[-A\ \cos(\lambda-2)\theta + B\ \sin(\lambda-2)\theta\right]..\\ +(\lambda-\kappa-1)\left[-C\ \cos\lambda\theta + D\ \sin\lambda\theta\right]\end{Bmatrix} \tag{2.46}$$

The interface and the crack divide the whole plane into three regions. In each region, there are four coefficients $A^{(j)}$, $B^{(j)}$, $C^{(j)}$, and $D^{(j)}$, where $j = 1, 2, 3$ denotes the region's number. Select the branch cut along the crack from origin to infinity, and so the angular range is $-\pi+\omega \le \theta \le \pi+\omega$. Then the twelve coefficients are determined by the following boundary conditions:

1). On $\theta = 0$ and $\theta = \pi$, tractions and displacements are continuous,

$$\sigma_{\theta\theta}^{(1)} = \sigma_{\theta\theta}^{(2)}\Big|_{\theta=0},\ \tau_{r\theta}^{(1)} = \tau_{r\theta}^{(2)}\Big|_{\theta=0},\ u_\theta^{(1)} = u_\theta^{(2)}\Big|_{\theta=0},\ u_r^{(1)} = u_r^{(2)}\Big|_{\theta=0} \tag{2.47}$$

$$\sigma_{\theta\theta}^{(1)} = \sigma_{\theta\theta}^{(3)}\Big|_{\theta=\pi},\ \tau_{r\theta}^{(1)} = \tau_{r\theta}^{(3)}\Big|_{\theta=\pi},\ u_\theta^{(1)} = u_\theta^{(3)}\Big|_{\theta=\pi},\ u_r^{(1)} = u_r^{(3)}\Big|_{\theta=\pi} \tag{2.48}$$

2). On $\theta = \pi+\omega$ and $\theta = -\pi+\omega$, tractions are free,

$$\sigma_{\theta\theta}^{(3)}\Big|_{\theta=\pi+\omega} = 0,\ \tau_{r\theta}^{(3)}\Big|_{\theta=\pi+\omega} = 0 \tag{2.49}$$

$$\sigma_{\theta\theta}^{(2)}\Big|_{\theta=-\pi+\omega}=0,\ \tau_{r\theta}^{(2)}\Big|_{\theta=-\pi+\omega}=0 \tag{2.50}$$

The above boundary conditions consist of a system of homogeneous linear equations and is written as $M\cdot x=0$, where vector x is composed of the twelve coefficients by means of $x=\left(A^{(1)},B^{(1)},C^{(1)},D^{(1)},A^{(2)},B^{(2)},C^{(2)},D^{(2)},A^{(3)},B^{(3)},C^{(3)},D^{(3)}\right)^T$ (superscript T means transpose) and the components of 12×12 matrix M are:

$$M_{12}=1,\ M_{14}=1,\ M_{16}=-1,\ M_{18}=-1,$$

$$M_{21}=\lambda-2,\ M_{23}=\lambda,\ M_{25}=-(\lambda-2),\ M_{27}=-\lambda,$$

$$M_{32}=(\lambda-2)\mu_2/\mu_1,\ M_{34}=(\lambda+\kappa_1-1)\mu_2/\mu_1,$$

$$M_{36}=-(\lambda-2),\ M_{38}=-(\lambda+\kappa_2-1),$$

$$M_{41}=(\lambda-2)\mu_2/\mu_1,\ M_{43}=(\lambda-\kappa_1-1)\mu_2/\mu_1,$$

$$M_{45}=-(\lambda-2),\ M_{47}=-(\lambda-\kappa_2-1),$$

$$M_{51}=\sin(\lambda\pi),\ M_{52}=\cos(\lambda\pi),\ M_{53}=\sin(\lambda\pi),\ M_{54}=\cos(\lambda\pi),$$

$$M_{59}=-\sin(\lambda\pi),\ M_{5,10}=-\cos(\lambda\pi),\ M_{5,11}=-\sin(\lambda\pi),\ M_{5,12}=-\cos(\lambda\pi),$$

$$M_{61}=(\lambda-2)\cos(\lambda\pi),\ M_{62}=-(\lambda-2)\sin(\lambda\pi),$$

$$M_{63}=\lambda\cos(\lambda\pi),\ M_{64}=-\lambda\sin(\lambda\pi),$$

$$M_{69}=-(\lambda-2)\cos(\lambda\pi),\ M_{6,10}=(\lambda-2)\sin(\lambda\pi),$$

$$M_{6,11}=-\lambda\cos(\lambda\pi),\ M_{6,12}=\lambda\sin(\lambda\pi),$$

$$M_{71}=(\lambda-2)\sin(\lambda\pi)\mu_2/\mu_1,\ M_{72}=(\lambda-2)\cos(\lambda\pi)\mu_2/\mu_1,$$

$$M_{73}=(\lambda+\kappa_1-1)\sin(\lambda\pi)\mu_2/\mu_1,\ M_{74}=(\lambda+\kappa_1-1)\cos(\lambda\pi)\mu_2/\mu_1,$$

$$M_{79}=-(\lambda-2)\sin(\lambda\pi),\ M_{7,10}=-(\lambda-2)\cos(\lambda\pi),$$

$$M_{7,11} = -(\lambda + \kappa_2 - 1)\sin(\lambda\pi),\ M_{7,12} = -(\lambda + \kappa_2 - 1)\cos(\lambda\pi),$$

$$M_{81} = -(\lambda - 2)\cos(\lambda\pi)\mu_2/\mu_1,\ M_{82} = (\lambda - 2)\sin(\lambda\pi)\mu_2/\mu_1,$$

$$M_{83} = -(\lambda - \kappa_1 - 1)\cos(\lambda\pi)\mu_2/\mu_1,\ M_{84} = (\lambda - \kappa_1 - 1)\sin(\lambda\pi)\mu_2/\mu_1,$$

$$M_{89} = (\lambda - 2)\cos(\lambda\pi),\ M_{8,10} = -(\lambda - 2)\sin(\lambda\pi),$$

$$M_{8,11} = (\lambda - \kappa_2 - 1)\cos(\lambda\pi),\ M_{8,12} = -(\lambda - \kappa_2 - 1)\sin(\lambda\pi),$$

$$M_{99} = \sin[(\lambda - 2)\omega + \lambda\pi],\ M_{9,10} = \cos[(\lambda - 2)\omega + \lambda\pi],$$

$$M_{9,11} = \sin[\lambda(\omega + \pi)],\ M_{9,12} = \cos[\lambda(\omega + \pi)],$$

$$M_{10,9} = (\lambda - 2)\cos[(\lambda - 2)\omega + \lambda\pi],\ M_{10,10} = -(\lambda - 2)\sin[(\lambda - 2)\omega + \lambda\pi],$$

$$M_{10,11} = \lambda\cos[\lambda(\omega + \pi)],\ M_{10,12} = -\lambda\sin[\lambda(\omega + \pi)],$$

$$M_{11,5} = \sin[(\lambda - 2)\omega - \lambda\pi],\ M_{11,6} = \cos[(\lambda - 2)\omega - \lambda\pi],$$

$$M_{11,7} = \sin[\lambda(\omega - \pi)],\ M_{11,8} = \cos[\lambda(\omega - \pi)],$$

$$M_{12,5} = (\lambda - 2)\cos[(\lambda - 2)\omega - \lambda\pi],\ M_{12,6} = -(\lambda - 2)\sin[(\lambda - 2)\omega - \lambda\pi],$$

$$M_{12,7} = \lambda\cos[\lambda(\omega - \pi)],\ M_{12,8} = -\lambda\sin[\lambda(\omega - \pi)],$$

All others $M_{ij} = 0$.

For nontrivial solution of *x*, the determinant of *M* must vanish, i.e., $\det(M) = 0$, which is a nonlinear equation of λ with parameters μ_2/μ_1, κ_1, κ_2, ω, where the subscripte 1 and 2 denote the material's number. Due to Dundurs' theory, the dependence on three dimensionless materials properties μ_2/μ_1, κ_1, κ_2 can be converted to two dimensionless parameters α and β, which are defined as:

$$\alpha = \frac{\mu_1(\kappa_2 + 1) - \mu_2(\kappa_1 + 1)}{\mu_1(\kappa_2 + 1) + \mu_2(\kappa_1 + 1)} \tag{2.51}$$

$$\beta = \frac{\mu_1(\kappa_2 - 1) - \mu_2(\kappa_1 - 1)}{\mu_1(\kappa_2 + 1) + \mu_2(\kappa_1 + 1)} \tag{2.52}$$

For a plain strain problem, $\kappa = 3 - 4\nu$; if $\nu_1 = \nu_2 = 1/3$, then $\beta = \alpha/4$; if $\nu_1 = \nu_2 = 1/2$, then $\beta = 0$. For a plain stress problem, $\kappa = (3-\nu)/(1+\nu)$; if $\nu_1 = \nu_2 = 1/2$, then $\beta = \alpha/4$; the case of $\beta = 0$ is possible since $\nu_1 = \nu_2 = 1$ is not allowed.

The singularity exponents λ, with restriction $0 \le \mathrm{Re}(\lambda) \le 1$, are the root of the equation $\det(M) = 0$. After algebraic calculation (Bogy 1971), the determinant $\det(M)$ can be expressed in the following:

$$\begin{aligned}\det(M) = {} & c_1\beta^4 + (c_2\alpha + c_3)\beta^3 + (c_4\alpha^2 + c_5\alpha + c_6)\beta^2 \ldots \\ & + (c_7\alpha^2 + c_8\alpha + c_9)\beta + (c_{10}\alpha^2 + c_{11}\alpha + c_{12})\end{aligned} \tag{2.53}$$

where

$$\begin{aligned}c_1(\lambda,\omega) = {} & 4(\lambda-1)^4\sin^4\omega - 4(\lambda-1)^2\sin^2\omega - \sin^2[(\lambda-1)(\pi-2\omega)] - \sin^2[(\lambda-1)\pi] \ldots \\ & + 2 - 2\left[2(\lambda-1)^2\sin^2\omega - 1\right]\left\{\sin^2[(\lambda-1)(\pi-\omega)] + \sin^2[(\lambda-1)\omega] - 1\right\}\end{aligned}$$

$$c_2(\lambda,\omega) = 4(\lambda-1)^2\sin^2\omega\left\{-2(\lambda-1)^2\sin^2\omega + \sin^2[(\lambda-1)(\pi-\omega)] + \sin^2[(\lambda-1)\omega]\right\}$$

$$c_3(\lambda,\omega) = c_2$$

$$c_4(\lambda,\omega) = 4(\lambda-1)^4\sin^4\omega + \sin^2[(\lambda-1)(\pi-2\omega)]$$

$$c_5(\lambda,\omega) = 2\left[1 - 2(\lambda-1)^2\sin^2\omega\right]\left\{\begin{array}{l} -4(\lambda-1)^2\sin^2\omega + \sin^2[(\lambda-1)(\pi-\omega)] \ldots \\ +\sin^2[(\lambda-1)\omega] - 1 \end{array}\right\} + 2$$

$$\begin{aligned}c_6(\lambda,\omega) = {} & 4(\lambda-1)^4\sin^4\omega + \sin^2[(\lambda-1)(\pi-\omega)] - 2\left\{1 - \sin^2[(\lambda-1)\pi]\right\} \ldots \\ & + 2\left[2(\lambda-1)^2\sin^2\omega - 1\right]\left\{\sin^2[(\lambda-1)(\pi-\omega)] + \sin^2[(\lambda-1)\omega] - 1\right\}\end{aligned}$$

$$c_7(\lambda,\omega) = 4(\lambda-1)^2\sin^2\omega\left[1 - 2(\lambda-1)^2\sin^2\omega\right]$$

$$c_8(\lambda,\omega) = 4(\lambda-1)^2\sin^2\omega\left\{2-2(\lambda-1)^2\sin^2\omega-\sin^2[(\lambda-1)(\pi-\omega)]-\sin^2[(\lambda-1)\omega]\right\}$$

$$c_9(\lambda,\omega) = 4(\lambda-1)^2\sin^2\omega\left\{1-\sin^2[(\lambda-1)(\pi-\omega)]-\sin^2[(\lambda-1)\omega]\right\}$$

$$c_{10}(\lambda,\omega) = 4(\lambda-1)^4\sin^4\omega-4(\lambda-1)^2\sin^2\omega-\sin^2[(\lambda-1)(\pi-2\omega)]+1$$

$$c_{11}(\lambda,\omega) = 2\left[2(\lambda-1)^2\sin^2\omega-1\right]\left\{\sin^2[(\lambda-1)(\pi-\omega)]+\sin^2[(\lambda-1)\omega]-1\right\}$$

$$c_{12}(\lambda) = 1-\sin^2[(\lambda-1)\pi]$$

Implementing the above equations in Matlab code, the eigenvalues and the associated eigenvectors can be obtained numerically.

2.8 Appendix B: Determination of coefficients b_{11}, b_{12}, b_{21}, b_{22}, c_{11}, c_{12}, c_{21} and c_{22}

We solve four boundary value problems sketched in Figure 2-12 and Figure 2-13, using the finite element code ABAQUS 6.5. Plane strain conditions are assumed, and Poisson's ratios of both materials are set to be 0.5, so that $\beta = 0$. The stress intensity factors of the primary crack, k_1 and k_2, are obtained by fitting Equation (2.6) with the stresses calculated for problems in Figure 2-12, along $\theta = \omega$ within $10^{-3} < r/R < 10^{-2}$. For the problems in Figure 2-13, the size of the penetrating crack *a* is set to be *R*/1000. The stress intensity factors of the penetrating crack, K_I^p, K_{II}^p, are read from the outputs of contour integrals. Two kinds of loading conditions (biaxial tension and pair-force stretch) give out two sets of (k_1, k_2) and (K_I^p, K_{II}^p). These stress intensity factors, along with the linear relations (2.10) and (2.11), allow us to solve the coefficients b_{11}, b_{12}, b_{21}

and b_{22}. Similarly, we use the finite element code to solve the boundary value problems in Figure 2-12 and Figure 2-14, which allow us to determine the coefficients c_{11}, c_{12}, c_{21} and c_{22} in (2.13) and (2.14).

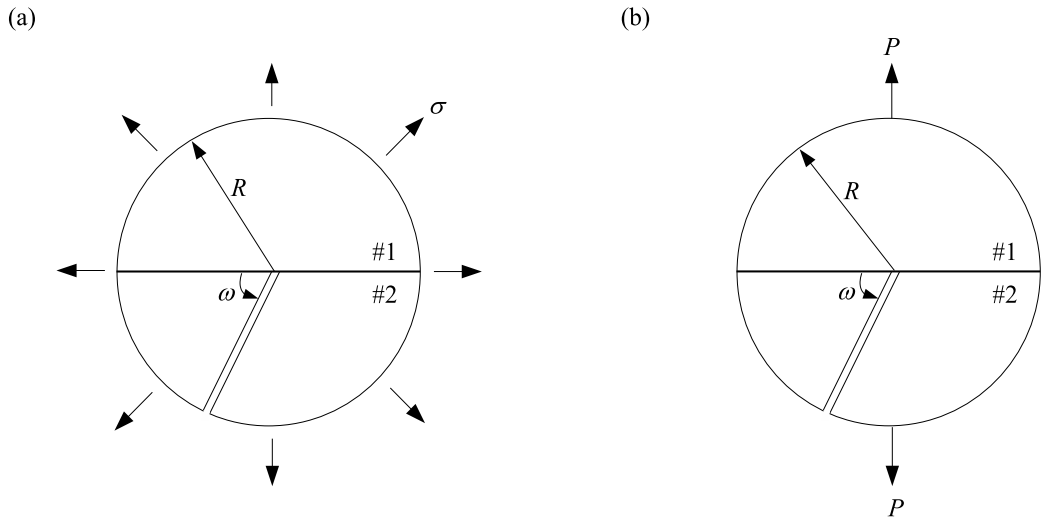

Figure 2-12:The geometry and loading conditions for the primary crack. (a) Biaxial tension. (b) Stretch by a pair of forces.

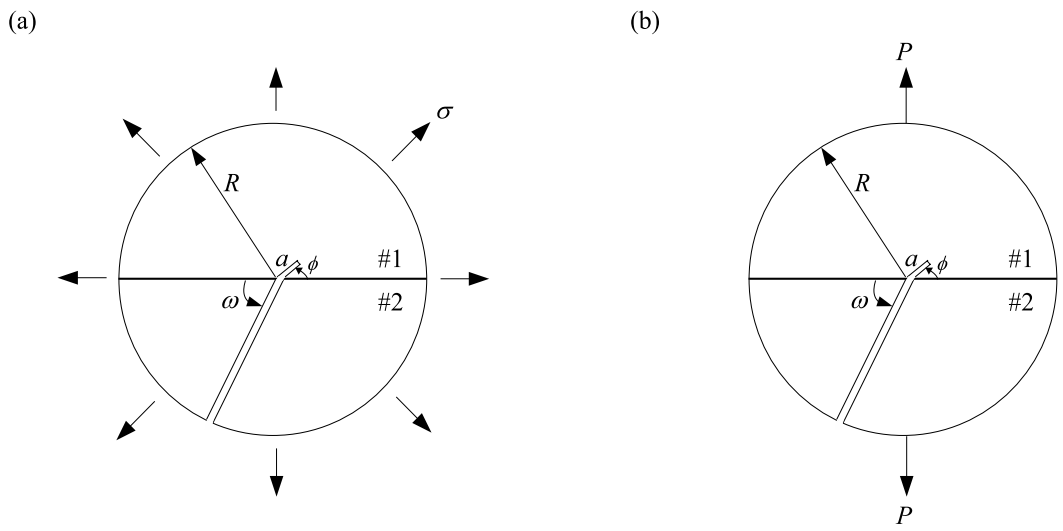

Figure 2-13:The two loading cases for the primary crack to penetrate across the interface. (a) Biaxial tension. (b) Stretch by a pair of forces.

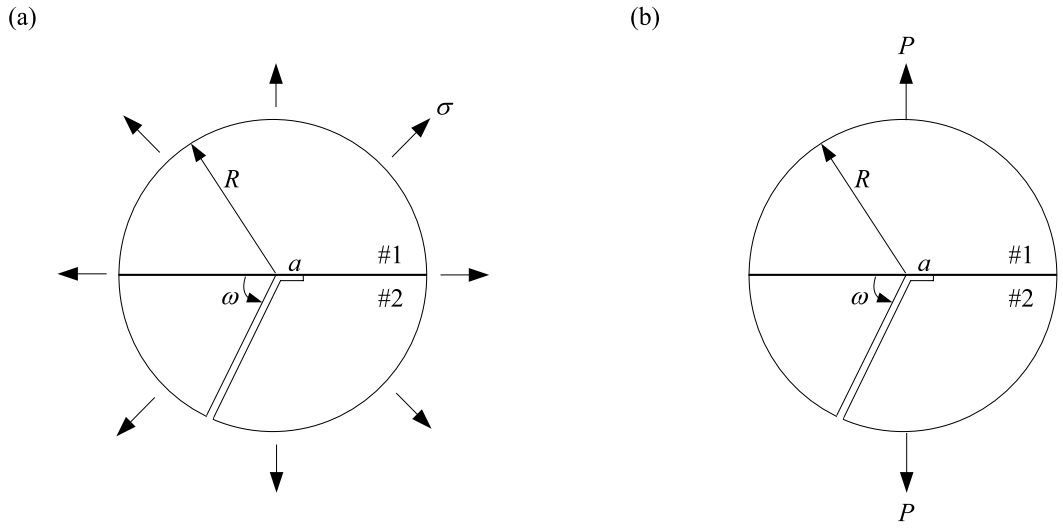

Figure 2-14:The two loading cases for the primary crack to deflect and debond the interface. (a) Biaxial tension. (b) Stretch by a pair of forces.

References:

1. Akisanya, A.R. and Fleck, N.A., 1997. Interfacial cracking from the free-edge of a long bi-material strip. Int. J. Solids Structures **34**, 1645-1665.
2. Ashaugh, N. E., 1975. Stress solution for a crack at an arbitrary angle to an interface. Int. J. Fract., **11**, 205-219.
3. Bogy, D.B., 1971. On the plane elastostatic problem of a loaded crack terminating at a material interface. J. Appl. Mech. **38**, 911-918.
4. Chen, D.H., 1994. A crack normal to and terminating at a bimaterial interface. Eng. Fract. Mech. **49**(4), 517-532.
5. Chen, J.-T. and Wang, W.-C., 1996. Experimental analysis of an arbitrarily inclined semi-infinite crack terminated at the bi-material interface. Experimental Mechanics **36**(1), 7-16.
6. Cook, J. and Gordon, J.E., 1964, A mechanism for the control of crack propagation in all-brittle systems. Proc. R. Soc. London **A 282**(139), 508-520.
7. Davis, J.B., Kristoffersson, A., Carlstrom, E. and Clegg, W.J., 2000. Fabrication and crack deflection in ceramic laminates with porous interlayers. J. Am. Ceram. Soc. **83**(10), 2369-2374.
8. Dundurs, J., 1969. Edge-bonded dissimilar orthogonal elastic wedges. J. Appl. Mech., **36**, 650-652.
9. Dunn, M.L., Hui, C.Y., Labossiere P.E.W. and Lin Y.Y., 2001. Small scale geometric and material features at geometric discontinuities and their role in fracture analysis. Int. J. Fract. **110**, 101-121.

10. Fenner, D.N., 1976. Stress singularities in composite materials and an arbitrary oriented crack meeting an interface. Int. J. Fract. **12**, 705-721.

11. Gupta, V., Argon, A.S. and Suo, Z., 1992. Crack deflection at an interface between two orthotropic media. J. Appl. Mech. **59**, S79-S87.

12. Hayashi, K., and Nemat-Nasser, S., 1981. Energy-release rate and crack kinking under combined loading. J. Appl. Mech. **48**, 520-524.

13. He, M-Y., and Hutchinson, J.W., 1988. Kinking of a crack out of an interface: Tabulated Solution Coefficients. Harvard University Report MECH-113A.

14. He, M-Y and Hutchinson, J.W., 1989a. Crack deflection at an interface between dissimilar elastic materials. Int. J. Solids Structures, **25**(9), 1053-1067.

15. He, M.-Y. and Hutchinson, J. W., 1989b. Kinking of a crack out of an interface. J. Appl. Mech. **56**, 270-278.

16. Hutchinson, J.W. and Suo Z., 1992. Mixed mode cracking in layered materials. Advances in Applied Mechanics **29**, 63-191.

17. Hui, C.Y. and Ruina, A., 1995. Why K? High order singularities and small scale yielding. Int. J. Fracture **72**, 97-120.

18. Irwin, G. R., 1957. Analysis of stresses and strains near the end of a crack traversing a plate. J. Appl. Mech. **24**, 361-364.

19. Joyce, M.R., Reed, P.A.S., and Syngellakis, S., 2003. Numerical modeling of crack shielding and deflection in a multi-layered material system. Mat. Sci. Eng. **A 342**, 11-22.

20. Kang, Y. and Lu, H., 2002. Investigation of near-tip displacement fields of a crack normal to and terminating at a bimaterial interface under mixed-mode loading. Eng. Fract. Mech. **69**, 2199-2208.

21. Kovar, D., Thouless, M.D., and Halloran, J.W., 1998. Crack deflection and propagation in layered silicon nitride/boron nitride ceramics. J. Am. Ceram. Soc. **81**(4), 1004-1012.

22. Labossiere, P.E.W., Dunn, M.L., and Cunningham, S.J., 2002. Application of bimaterial interface corner failure mechanics to silicon/glass anodic bonds. J. Mech. Phys. Solids **50**, 405-433.

23. Lawn, B., 1993. Fracture of Brittle Solids, 2nd ed., Cambridge University Press.

24. Leguillon, D., Lacroix, C. and Martin, E., 2000. Interface debonding ahead of a primary crack. J. Mech. Phys. Solids **48**, 2137-2161.

25. Leguillon, D., Lacroix, C. and Martin, E., 2001. Crack deflection by an interface – asymptotics of the residual thermal stress. Int. J. Solids Struct. **38**, 7423-7445.

26. Lemaitre, J., Desmorat, R., Vidonne, M.P. and Zhang P., 1996. Reinitiation of a crack reaching an interface. Int. J. Fract. **80**, 257-276.

27. Li, J., Zhang, X.B. and Recho, N., 1997. Investigation of an arbitrarily oriented crack meeting an interface between two elastic materials. European Journal of Mechanics A-Solids **16** (5), 795-821.

28. Liu, X.H., Suo, Z. and Ma, Q., 1999, Split singularities: stress field near the edge of a silicon die on a polymer substrate. Acta Mater. **47**(1), 67-76.

29. Lu, M.C. and Erdogan, F., 1983. Stress intensity factors in two bonded elastic layers containing cracks perpendicular to and on the interface--- I. Analysis. Eng. Fract. Mech. **18**, 491-506.

30. Malyshev, B.M. and Salganik, R.L., 1965. The strength of adhesive joints using the theory of cracks. Int. J. Fract. Mech. **1**(2), 114-128.

31. Martinez, D. and Gupta, V., 1993. Energy criterion for crack deflection at an interface between two orthotropic media, II: Results and experimental verification. J. Mech. Phys. Solids. **42**, 1247-1271.

32. Mohammed, I. And Liechti, K.M., 2000. Cohesive zone modeling of crack nucleation at bimaterial corners. J. Mech. Phys. Solids **48**, 735-764.

33. Nuler, B., Ryvkin, M., Chudnovsky, A., 2006. Crack stability in a vicinity of interface. In press.

34. Parmigiani, J.P. and Thouless, M.D., 2006. The roles of toughness and cohesive strength on crack deflection at interfaces. J. Mech. Phys. Solids **54**, 266-287.

35. Reedy, E.D., 2000. Connection between interface corner and interfacial fracture analyses of an adhesively-bonded butt joint. Int. J. Solids Struct. **37**, 2429-2442.

36. Rice, J.R., 1988. Elastic fracture mechanics concepts for interfacial cracks. J. Appl. Mech. **55**, 98-103.

37. Roham, S., Hardikar, K. and Woytowitz, P., 2004. Crack penetratrion and deflection at a bimaterial interface in a four-point bend test. J. Mater. Res. **19**(10), 3019-3027.

38. Thouless, M.D., Cao, H.C. and Mataga, P.A., 1989. Delamination from surface cracks in composite materials. J. Mater. Sci., **24**, 1406-1412.

39. Williams, M.L., 1959. The stress around a fault or crack in dissimilar media. Bulletin of the Seismological Society of America **49**(2), 199-204.

40. Zak, A.R. and Williams, M.L., 1963. Crack point singularities at a bi-material interface. J. Appl. Mech. **31**, 142-143.

Chapter 3 Dislocation Injection from Sharp Features in Strained Silicon Structures

The mobility of charge carriers in silicon can be significantly increased when silicon is subject to a field of strain. However, a microelectronic device usually contains sharp features, e.g., edges and corners, which may intensify stresses, inject dislocations into silicon, and ultimately fail the device. The stress field at an edge is singular, and is often a linear superposition of two modes of different exponents. We characterize the relative contribution of the two modes by a mode angle, and determine the critical slip systems as the amplitude of the load increases. We calculate the critical residual stress in a thin-film stripe bonded on a silicon substrate.

The material system of SiN/silicon is a commonly adopted structure in semiconductor industry to manufacture strained silicon. For this specific material combination, we simplify the singular stress field to a single mode, and therefore, simplify the criterion of dislocation injection. In addition, we interpret available experiments of SiN pads on silicon substrates.

3.1 Introduction

Stresses inevitably arise in a microelectronic device due to mismatch in coefficients of thermal expansion, mismatch in lattice constants, and growth of materials. Moreover, in the technology of strained silicon devices, stresses have been deliberately introduced to increase mobility of electrons and holes; see Ieong et al. (2004) for a review. The strains, however, may cause mechanical failure. In particular, the devices usually contain sharp features like edges and corners, which may intensify stresses, inject dislocations into silicon, and fail the device (Dellith et al., 1996; Miyake and Takahashi, 1997). On the basis of singular stress fields near the sharp features, this chapter describes a method to predict conditions under which such sharp features do not emit dislocations (Zhang et al., 2006; Liu et al., 1999; Zhang and Suo, 2007).

We illustrate the method using an idealized structure shown in Figure 3-1. A blanket film, of thickness h and residual stress σ, is grown on the (001) surface of a single-crystal silicon substrate. The film is then patterned into a stripe of width L, with the side surfaces parallel to the (110) plane of silicon. When the film covers the entire surface of the substrate, the film is in a state of uniform stress, and the substrate is stress-free. When the film is patterned into a stripe, a field of stress builds up in the substrate, and concentrates at the root of each edge. It is this concentrated stress that injects dislocations into silicon substrate.

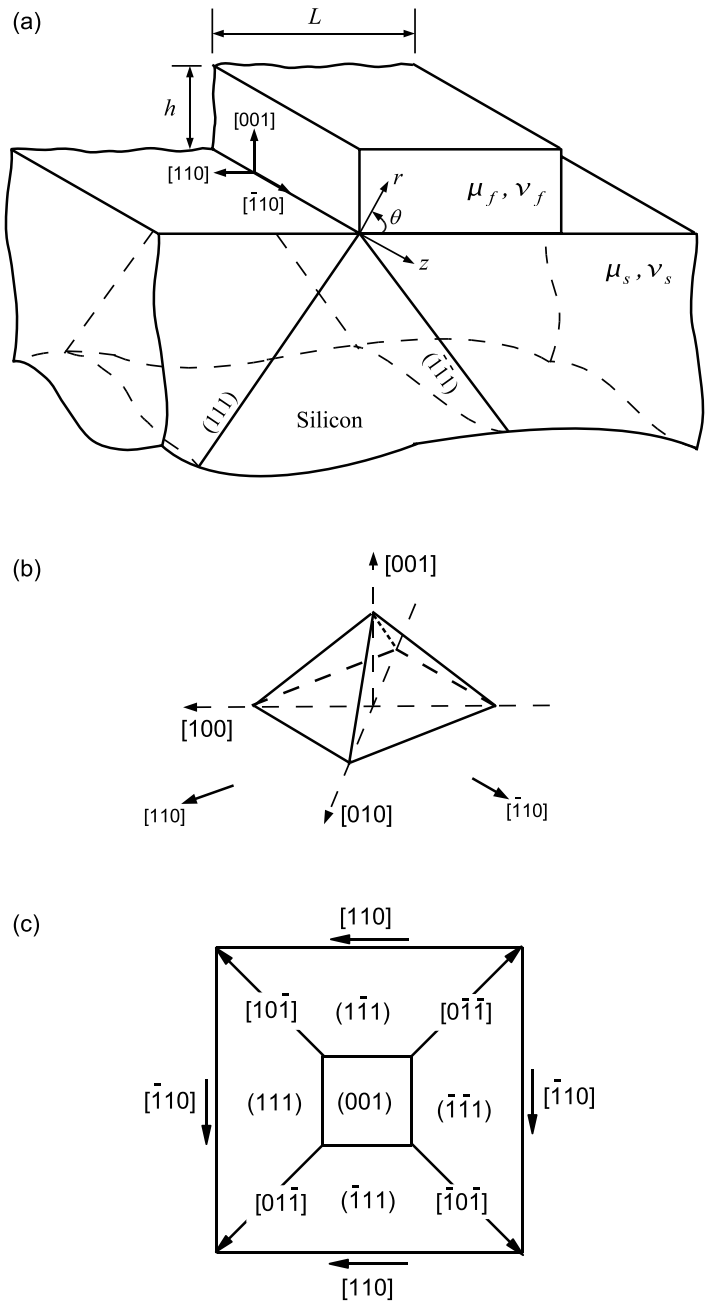

Figure 3-1:(a) A blanket thin film, of thickness *h* and residual stress σ, is grown on the (001) surface of a single-crystal silicon substrate. The film is then patterned into a stripe of width *L*, with the side surfaces parallel to the (110) plane of silicon. (b) The pyramid shows the crystal orientation. (c) Slip systems.

Early models of the stress field near an edge of a film have been reviewed in Hu (1991) and Jain et al. (1996). One model, for example, replaces the edge with a concentrated force acting on the surface of the substrate (Hu, 1978; Isomae, 1981; Vanhellemont et al., 1987a). Not surprisingly, the resulting stress field is inaccurate at a distance smaller than the film thickness, as demonstrated by a finite element analysis (Schwarz and Chidambarrao, 1999).

We will study the stress field using a method developed by Williams (1952), Bogy (1971) and others. The method has also been used to analyze the nucleation of a misfit dislocation from the edge of an epitaxial island (Johnson and Freund, 1997).

The structure in Figure 3-1 is similar to those studied in Kammler et al. (2005), Hu (1978, 1979, 1991), Isomae (1981), Vanhellemont et al (1987a, 1987b, 1988), Jain et al (1996), and Schwarz and Chidambarrao (1999). Here we use a long stripe, rather than a square pad, so that we can focus on the essentials of the method without the complication of three-dimensional corners of the pad. The latter will be considered elsewhere.

This chapter will examine a specific aspect: split singularities. It is well known that, at the tip of a crack in a homogeneous elastic material, under the plane strain conditions, the singular stress field is a linear superposition of two modes, the tensile mode and the shearing mode, both modes having the exponent of ½. More generally, at the tip of bonded wedges of dissimilar materials, the singular stress field may still consist of two modes, but usually of unequal exponents, either a pair of complex conjugates, or two unequal real numbers (Akisanya and Fleck, 1997; Mohammed and Liechti, 2000; Reedy, 2000; Labossiere et al., 2002; Zhang and Suo, 2007). The case of complex-

conjugate exponents has been extensively discussed within the context of a crack lying on a bimaterial interface (e.g., Rice, 1988). The present chapter will focus on the case that the two modes have unequal real exponents. That is, a stronger and a weaker singularity coexist. It has been shown that both singularities can be important in causing failure (Liu et al., 1999; Labossiere et al., 2002; Zhang and Suo, 2007). Section 3.2 will describe the linear superposition of two modes of singular stress fields. Section 3.3 will investigate which slip systems will be activated. Section 3.4 will calculate the critical residual stress in the thin-film stripe for injecting dislocations into the silicon substrate. Section 3.5 will consider the specific material system of SiN/silicon. The concluding remarks are given in Section 3.6.

3.2 Split singularities and measure of mode mixity

The inset of Figure 3-2 illustrates an edge of the thin film bonded on the substrate, along with a system of polar coordinates (r,θ,z). In this view focused on the root of the edge, the film takes the quarter space, $0^0 \le \theta \le 90^0$, and the substrate takes the half space, $-180^0 \le \theta \le 0^0$. The two materials are bonded along the interface, $\theta = 0^0$. Both materials are taken to be elastic and isotropic. For problems of this type, Dundurs (1969) showed that the stress field depends on elastic constants through two dimensionless parameters:

$$\alpha = \frac{\mu_f(1-\nu_s)-\mu_s(1-\nu_f)}{\mu_f(1-\nu_s)+\mu_s(1-\nu_f)}. \tag{3.1}$$

$$\beta = \frac{1}{2}\left[\frac{\mu_f(1-2\nu_s)-\mu_s(1-2\nu_f)}{\mu_f(1-\nu_s)+\mu_s(1-\nu_f)}\right]. \tag{3.2}$$

where μ is the shear modulus, and ν Poisson's ratio. The subscripts *f* and *s* refer to the film and the silicon substrate, respectively. By requiring $0 \le \nu \le 0.5$ and $\mu > 0$, the Dundurs parameters are confined within a parallelogram in the (α, β) plane, with vertices at $(1, 0)$, $(1, 0.5)$, $(-1, 0)$ and $(-1, -0.5)$.

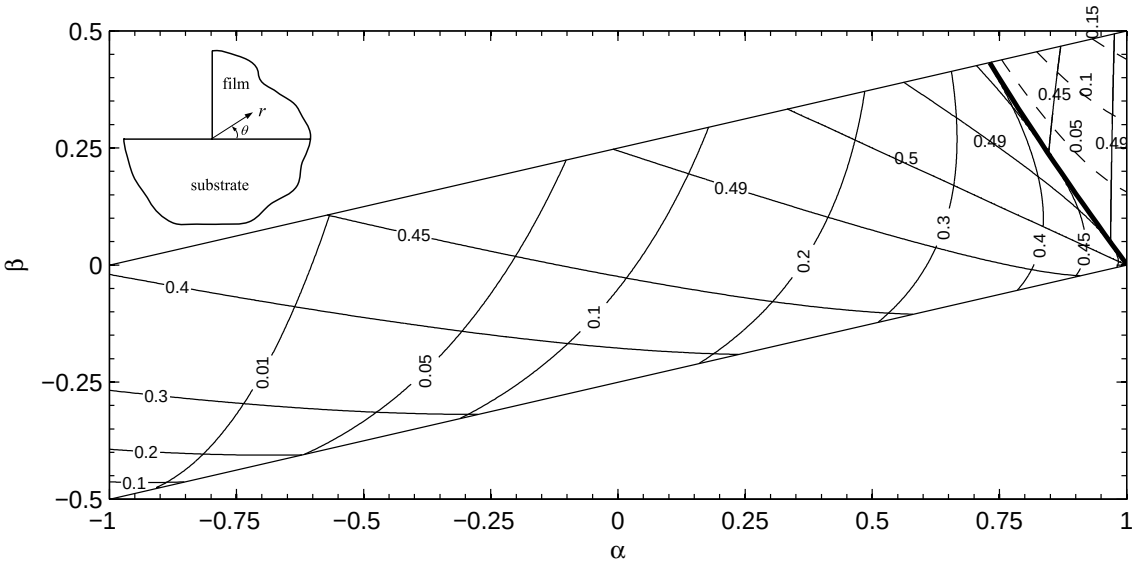

Figure 3-2:The inset shows the root of an edge of a thin film bonded on a substrate. Contours of the singular exponents are plotted on the plane of the Dundurs parameters (α , β). The parallelogram is divided into two regions by a dark curve. In the lower-left region, the exponents are two unequal real numbers, with the larger one labeled horizontally and the smaller one labeled vertically. In the upper-right region, the exponents are a pair of complex conjugates, with real part depicted by solid lines and labeled horizontally, and the imaginary part depicted by dashed line and labeled vertically.

For a singular field around the root of the edge, each component of the stress tensor, say $\sigma_{\theta\theta}$, takes the form of $\sigma_{\theta\theta} \sim r^{-\lambda}$. This singular stress field is determined by an eigenvalue problem, resulting in a transcendental equation that determines the exponent λ (Williams, 1952; Bogy, 1971; Liu et al., 1999). The exponent is restricted as $0 < \mathrm{Re}(\lambda) < 1$, a restriction commonly adopted, with justifications critiqued in Hui and Ruina (1995) and Dunn et al. (2001). For the specific geometry illustrated in the inset, Figure 3-2 plots the contours of the exponents on the (α, β) plane. The parallelogram is divided into two regions by a dark curve. In the lower-left region, the exponents are two unequal real numbers, one stronger (λ_1) and the other weaker (λ_2). The values for λ_1 are labeled horizontally, and those for λ_2 are labeled vertically. In the whole region, $\lambda_2 < \lambda_1 \le 0.5$. In the upper-right region, the exponents are a pair of complex conjugates, $\lambda_{1,2} = \xi \pm i\varepsilon$. The real part is depicted by solid lines and labeled horizontally, while the imaginary part is depicted by dashed lines and labeled vertically. At each point on the boundary (i.e., the dark curve), the two exponents degenerate to one number: when the point is approached from a region of real exponents, the two real exponents become identical; when the point is approached from a region of complex-conjugate exponents, the imaginary part vanishes. When $\alpha = 1$, i.e, the film is rigid, the singularity exponents are the same as those for an interfacial crack, $\lambda_{1,2} = 0.5 \pm i\varepsilon$, with $\varepsilon = 1/(2\pi) \ln[(1-\beta)/(1+\beta)]$ (Lu et al., 2007).

As noted in Liu et al. (1999), when the two materials have similar elastic constants, i.e., when $\alpha = \beta = 0$, the two modes of singular fields can be interpreted readily. In this case, the line bisecting the angle of the wedge is a line of symmetry. The

stronger mode corresponds to a stress field symmetric about this line (i.e., the tensile mode). The weaker mode corresponds to a stress field anti-symmetric about this line (i.e., the shearing mode). When the two materials have dissimilar elastic constants, however, the symmetry is broken, and the two modes may not be interpreted in such a simple way.

Following a common practice, in this chapter we will use α to represent the elastic mismatch, and neglect the effect of β by setting $\beta = 0$. When $\beta = 0$, the exponents are two unequal real numbers, regardless the values of α.

We next paraphrase several fundamental ideas in fracture mechanics (Lawn, 1993). Once we retain the two unequal exponents, the stress field around the root of the edge is a linear superposition of the two modes:

$$\sigma_{ij}(r,\theta) = \frac{k_1}{(2\pi r)^{\lambda_1}} \Sigma_{ij}^1(\theta) + \frac{k_2}{(2\pi r)^{\lambda_2}} \Sigma_{ij}^2(\theta). \tag{3.3}$$

The angular functions $\Sigma_{ij}^1(\theta)$ and $\Sigma_{ij}^2(\theta)$ are normalized such that $\Sigma_{r\theta}^1(0) = \Sigma_{r\theta}^2(0) = 1$, and their full expressions are listed in Section 3.7 in this chapter. The stress intensity factors, k_1 and k_2, are determined by the external boundary conditions, as described in Section 3.4.

The actual stress field around the root deviates from Eq.(3.3) within a zone, known as the process zone, because materials deform inelastically and because the root is not perfectly sharp. We are interested in a conservative condition for dislocations to be emitted, and assume that the root is atomistically sharp. Let Λ be the size of the process zone, within which the singular stress field (3.3) is invalid. Also, the singular stress field (3.3) is invalid at size scale h, where the external boundary conditions will change the stress distribution. However, provided the process zone is significantly smaller than the

macroscopic length, $\Lambda << h$, the singular stress field (3.3) prevails within an annulus, known as the *k*-annulus, of some radii bounded between Λ and *h*.

The two parameters, k_1 and k_2, have different dimensions, $(\text{stress})(\text{length})^{\lambda_1}$ and $(\text{stress})(\text{length})^{\lambda_2}$, respectively. We introduce a convention by writing

$$k_1 = S\Lambda^{\lambda_1}\cos\psi\,, \qquad k_2 = S\Lambda^{\lambda_2}\sin\psi\,. \tag{3.4}$$

This convention is illustrated in Figure 3-3. Here S and ψ characterizes the stress field at length scale Λ, with S characterizing the amplitude of the stress field, and ψ characterizing the relative contribution of the two modes. Since both k_1 and k_2 can be either positive or negative, the mode angle can be in the entire range of $0 \le \psi < 360^0$.

The microscopic process of dislocation emission occurs within the process zone, but is driven by the stress field (3.3) in the *k*-annulus. Dislocations emit from the root when the amplitude S reaches a critical value S_c, namely,

$$S(\psi) = S_c(\psi). \tag{3.5}$$

The amplitude S and the mode angle ψ are determined by the external boundary conditions, by solving a boundary value problem of linear elasticity. The critical condition $S_c(\psi)$ is determined either by experimental measurement or by computation from a microscopic model of the emission process.

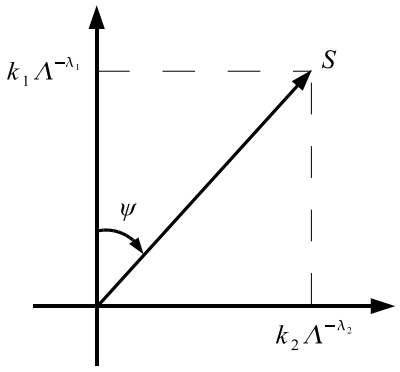

Figure 3-3:The graphical representation of the amplitude S and the mode angle ψ.

3.3 Selection of critical slip system

The twelve slip systems in silicon are depicted in Figure 3-1(c) graphically and listed in Table 3-1. Given a mode angle, ψ, as the amplitude S increases, some slip systems will activate earlier than others. We select the critical slip systems by the following procedure. For each slip system, we use the stress field (3.3) to calculate the resolved shear stress at distance $r = \Lambda$. The slip system with the maximum resultant shear stress is taken to be the critical slip system.

For a given slip system, let n_i be the unit vector normal to the slip plane, and b_j be the Burgers vector. Under a general state of stress σ_{ij}, the resolved shear stress on the slip system is

$$\tau_{nb} = \left|\sigma_{ij} n_i b_j\right| / b . \tag{3.6}$$

A combination of (3.3), (3.4) and (3.6) gives the resolved shear stress at the distance $r = \Lambda$ by

$$\frac{\tau_{nb}}{S} = \left| \cos\psi \frac{\Sigma_{ij}^{1}(\theta) n_i b_j}{(2\pi)^{\lambda_1} b} + \sin\psi \frac{\Sigma_{ij}^{2}(\theta) n_i b_j}{(2\pi)^{\lambda_2} b} \right|. \tag{3.7}$$

Because this procedure only invokes the magnitude, not the direction, of the resolved shear stress, a simultaneous change in the sign of the two stress intensity factors k_1 and k_2 will not change the condition of dislocation emission. Consequently, we can restrict the range of the mode angle to $-90^0 \le \psi \le 90^0$. Indeed, the right-hand side of (3.7) is a function of ψ with a period of 180^0.

An inspection of Figure 3-1 shows that the slip systems $\frac{1}{2}(111)[\bar{1}10]$ and $\frac{1}{2}(\bar{1}\,\bar{1}1)[\bar{1}10]$ are of zero resolved shear stress. The slip systems $\frac{1}{2}(111)[10\bar{1}]$ and $\frac{1}{2}(111)[01\bar{1}]$ are of identical resolved shear stress and with fixed polar angle $\theta = -125.26^0$. Other similar pairs of slip systems are listed in Table 3-1. By contrast, the resolved shear stress for slip systems $\frac{1}{2}(1\bar{1}\,\bar{1})[110]$ and $\frac{1}{2}(\bar{1}11)[110]$ is a function of polar angle θ. As an example, in Figure 3-4(a), the resolved shear stress is plotted as a function of θ for $\psi = 0$ and $\alpha = 0.5$. The polar angle θ^* corresponding to the maximum resolved shear stress is selected as the critical angle where the potential dislocation is nucleated. In Figure 3-4(b), the critical polar angle θ^* in the loading range $-90^0 \le \psi \le 90^0$ is plotted for $\alpha = 0.5$. This procedure can be repeated for all values of α.

For $\alpha = 0.5$, Figure 3-5(a) plots the resolved shear stresses as a function of the mode angle ψ for all twelve slip systems. The slip system with largest resolved shear stress is the potential slip system on which dislocations are firstly injected. The slip systems so selected are marked as the critical slip system for the whole range value of

$-90^0 \le \psi \le 90^0$. Obviously, different slip systems can be activated for different values of mode angle ψ. Similarly, the critical slip systems for any material combination under any mode angle can be selected, such as shown in Figure 3-5(b) for $\alpha = 0$ and in Figure 3-5(c) for $\alpha = -0.5$.

Table 3-1:The twelve slip systems and the corresponding critical polar angles are listed.

Slip plane, n	Slip direction, b	Critical polar angle, θ^*
(111)	$[\bar{1}10]$	-125.26°
	$[10\bar{1}]$	-125.26°
	$[01\bar{1}]$	-125.26°
$(1\bar{1}1)$	$[110]$	*Figure 3-4
	$[10\bar{1}]$	-125.26°
	$[0\bar{1}\bar{1}]$	-54.74°
$(\bar{1}\bar{1}1)$	$[\bar{1}10]$	-54.74°
	$[0\bar{1}\bar{1}]$	-54.74°
	$[\bar{1}0\bar{1}]$	-54.74°
$(\bar{1}11)$	$[110]$	*Figure 3-4
	$[\bar{1}0\bar{1}]$	-54.74°
	$[01\bar{1}]$	-125.26°

*For slip systems $\frac{1}{2}(1\,\bar{1}\,1)[110]$ and $\frac{1}{2}(\bar{1}\,11)[110]$, the critical polar angle, i.e. the polar angle for which the resolved shear stress has a maximum, depends on the mode angle. This dependence is depicted in Figure 3-4.

(a)

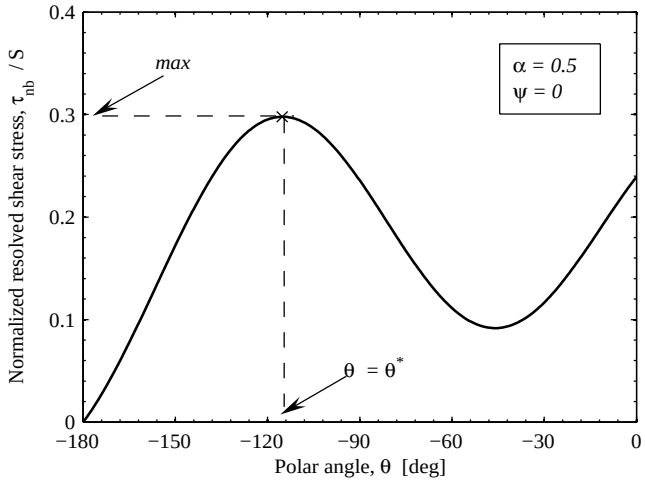

(b)

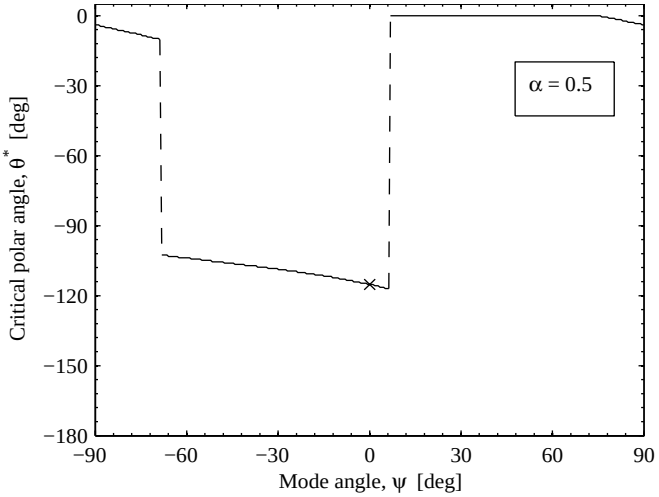

Figure 3-4:The normalized resolved shear stress for slip systems $\frac{1}{2}(1\bar{1}1)[110]$ and $\frac{1}{2}(\bar{1}11)[110]$ is a function of the polar angle θ. As an example, in (a), the normalized shear stress is plotted as a function of θ. The polar angle θ^* corresponding to maximum resolved shear stress is selected and marked by "$\times$" as the critical angle where the potential dislocation is nucleated. In (b), all the critical polar angle θ^* in the range $-90^0 \le \psi \le 90^0$ is plotted for $\alpha = 0.5$.

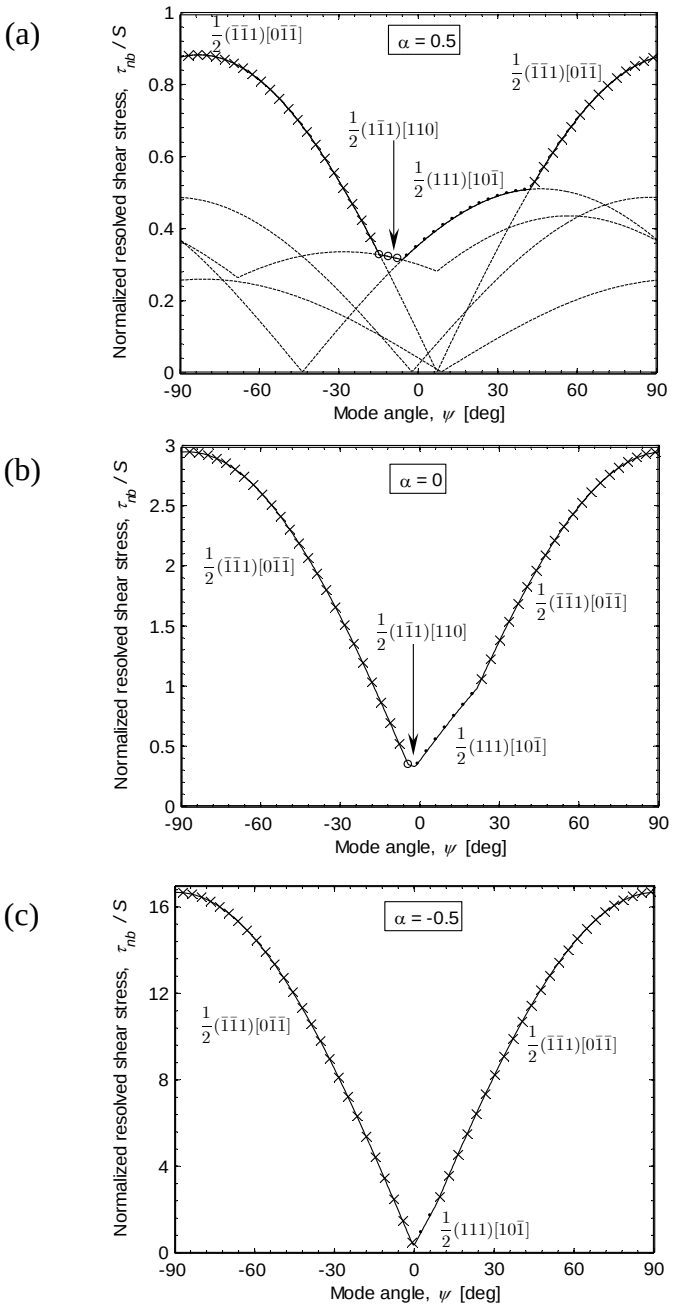

Figure 3-5:Normalized resolved shear stresses are plotted as a function of mode angle for all of the twelve slip systems. The slip system with largest resolved shear stress is the potential slip system on which the dislocation is firstly injected, so those slip systems are selected and marked for the whole range of the mode angle, $-90^0 \le \psi \le 90^0$. (a) $\alpha = 0.5$ (b) $\alpha = 0$ (c) $\alpha = -0.5$.

3.4 Critical condition for dislocation injection

The stress field around the root of the edge is described by Eq.(3.3). Linearity and dimensional consideration dictate that the stress intensity factors k_1 and k_2 should take the form

$$k_1 = \sigma h^{\lambda_1} f_1(L/h,\alpha), \quad k_2 = \sigma h^{\lambda_2} f_2(L/h,\alpha) \tag{3.8}$$

where the dimensionless functions $f_1(L/h,\alpha)$ and $f_2(L/h,\alpha)$ are determined as follows. We calculate the full stress field in the structure by using the finite element package ABAQUS6.6, then fit the interfacial shear stress close to the root, say $10^{-3} < r/h < 10^{-2}$, to the equation

$$\sigma_{r\theta}(\theta = 0) = \frac{k_1}{(2\pi r)^{\lambda_1}} + \frac{k_2}{(2\pi r)^{\lambda_2}}, \tag{3.9}$$

with k_1 and k_2 as fitting parameters. The two functions so calculated are plotted in Figure 3-6. The trend is understood as follows. Although the stress field intensifies at the root, the side surface of the stripe is traction-free. When the stripe is very narrow, $L/h \to 0$, the stress in the stripe is almost fully relaxed. When the stripe is very wide, $L/h \to \infty$, the stress field near one edge of the stripe no longer feels the presence of the other edge, so f_1 and f_2 attain plateaus.

A combination of (3.4) and (3.8) gives the mode angle ψ as

$$\tan\psi = \frac{f_2}{f_1}\left(\frac{\Lambda}{h}\right)^{\lambda_1-\lambda_2} \tag{3.10}$$

Obviously, $\eta = \tan\psi$ is the mode mixity defined in Chapter 2.

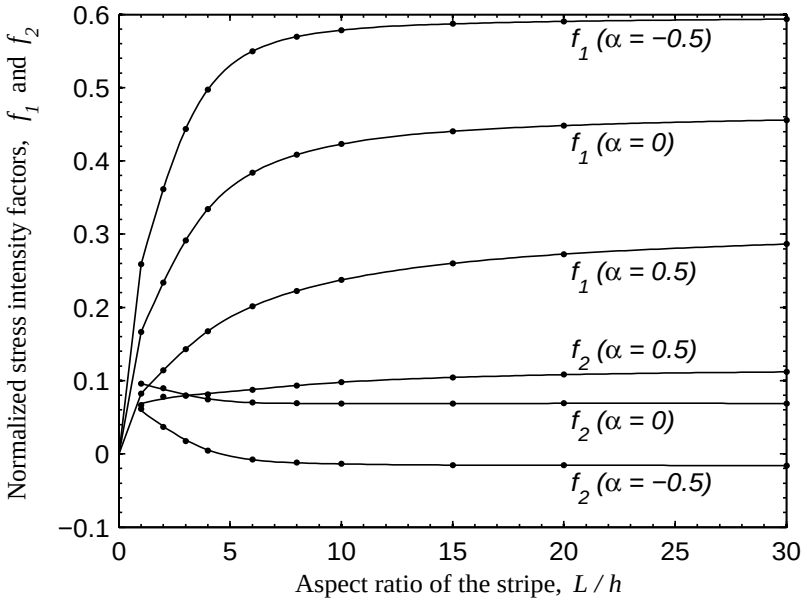

Figure 3-6:The normalized stress intensity factors, f_1 and f_2, are plotted as a function of the aspect ratio, L/h, of the stripe on the silicon substrate.

Take the typical value of film thickness $h = 100\,\text{nm}$, and take the process zone size Λ to be the Burgers vector in silicon $b = 0.383\text{nm}$. Figure 3-7 plots the mode angle ψ as a function of the Dundurs parameter α for aspect ratio of the stripe, $L/h = 2$ and 20. We observe that for the values of $\alpha < 0$, i.e. when the film is more compliant than the substrate, both the elastic mismatch and the aspect ratio have negligible effects on the mode angle ψ, and the weaker singular term in Eq.(3.3) is negligible, so that the singular stress field (3.3) can be simplified to the single mode. However, for positive values of α, i.e., when the film is stiffer than the substrate, the mode angle ψ increases very fast, and both singular terms in (3.3) should be taken into account.

We now calculate the critical residual stress in the thin-film stripe to inject dislocations into silicon. We assume that the critical condition is reached when the the

maximum resolved shear stress reaches the theoretical shear strength at distance $r = b$. The theoretical shear strength is estimated by $\tau_{th} = 0.2\mu$, where μ is the shear modulus of silicon (Hirth and Lothe, 1992). Setting $\tau_{nb}(b) = \tau_{th}$, a combination of Eqs. (3.3), (3.6) and (3.8) gives a scaling relation between the critical residual stress and the feature sizes:

$$\frac{\sigma_c}{\mu} = 0.2\left\{\left|\left[\left(\frac{h}{b}\right)^{\lambda_1}\frac{\Sigma_{ij}^1(\theta)}{(2\pi)^{\lambda_1}}f_1 + \left(\frac{h}{b}\right)^{\lambda_2}\frac{\Sigma_{ij}^2(\theta)}{(2\pi)^{\lambda_2}}f_2\right]\frac{n_i b_j}{b}\right|\right\}^{-1} . \tag{3.11}$$

Figures 3-5 and 3-7 show that the critical slip systems are $\frac{1}{2}(111)[01\bar{1}]$ and $\frac{1}{2}(111)[10\bar{1}]$. In Figure 3-8, we plot the normalized critical stresses as a function of the aspect ratio *L/h* for Dundurs $\alpha = 0.5$, 0, -0.5. A plateau is reached for large values of the aspect ratio *L/h*. When the aspect ratio is decreased, the critical stress will drastically improve, implying the fact that a narrow stripe might not inject dislocations into the silicon substrate, while a wide stripe could inject dislocations. Also evident is that the critical stress increases as the film becomes stiffer. This is because the same level of residual stress in a stiff film will induce a low level of stress if the substrate is relatively compliant.

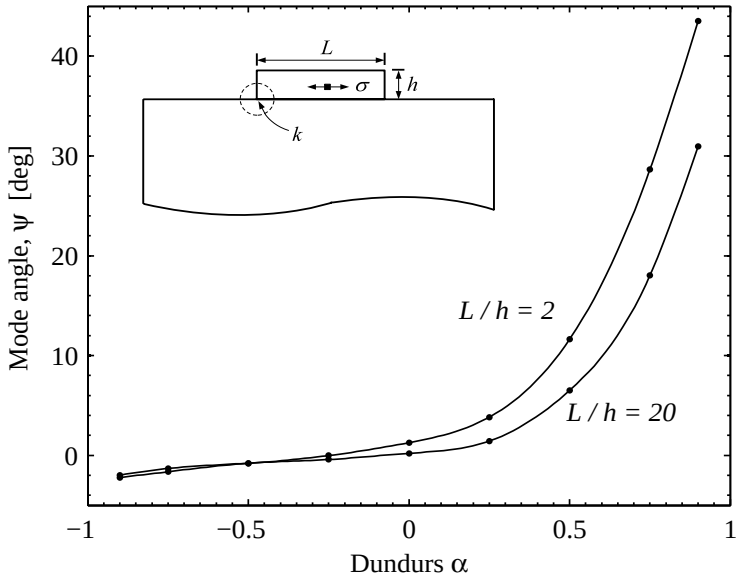

Figure 3-7:Mode angle ψ is plotted as a function of Dundurs parameter α for aspect ratio of the stripe, $L/h = 2$ and 20.

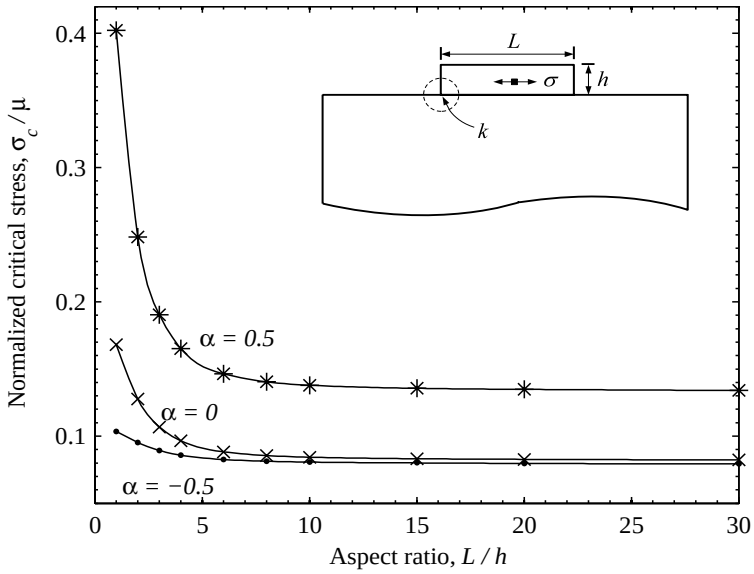

Figure 3-8:Normalized critical stresses are plotted as a function of the aspect ratio *L/h* for Dundurs parameter $\alpha = 0.5$, 0, -0.5.

3.5 SiN/silicon system

In semiconductor industry, SiN films are typically used as a "stressor" to apply strain in silicon to increase the mobility of electrons and holes (Hu, 1978; Isomae, 1981; Vanhellemont et al., 1987; Jain et al., 1999; Schwarz and Chidambarrao, 1999; Kammler et al., 2005). In this section, we will investigate the special aspects for the material system of SiN/silicon.

3.5.1 Single mode dominance

The SiN stripe is of shear modulus 54.3GPa and Poisson's ratio 0.27. The silicon substrate is of shear modulus 68.1GPa and Poisson's ratio 0.22. Both materials are taken to be isotropic since anisotropy in the elasticity of silicon plays little role in the singular stress field (Suwito et al., 1999). The elastic mismatch is small, $\alpha = -0.079 \approx 0$. The singularity exponents are $\lambda_1 = 0.4514$ and $\lambda_2 = 0.0752$. Still taking $h = 100$ nm and $b = 0.383$nm, from Figure 3-7, we obtain that $\psi = 0.2^0$ for $L/h = 20$, and $\psi = 1.27^0$ for $L/h = 2$. Evidently, in this case the weaker singularity makes negligible contribution. From Figure 3-5(b), we identify the critical slip systems are $\frac{1}{2}(111)[01\bar{1}]$ and $\frac{1}{2}(111)[10\bar{1}]$.

Hence, the stress field around the root takes the form

$$\sigma_{ij}(r,\theta) = \frac{k}{(2\pi r)^{\lambda}} \Sigma_{ij}(\theta). \tag{3.12}$$

with $\lambda = 0.4514$. The corresponding angular functions are listed in Section 3.7 in this chapter, with the coefficients in silicon substrate to be $A = 0.9874$, $B = 0.3534$, $C = -0.6503$, and $D = 1.8348$. The quantity k is known as the stress intensity factor. Linearity and dimensional consideration dictate that k should take the form

$$k = \sigma h^{\lambda} f(L/h). \tag{3.13}$$

The stress intensity factor scales with the residual stress σ and with h^{λ}; the dimensionless function $f(L/h)$ is determined by fitting the interfacial shear stress close to the root, say $10^{-3} < r/h < 10^{-2}$, the same as in Section 3.4 except that the fitted equation becomes:

$$\sigma_{r\theta} = k/(2\pi r)^{\lambda}. \tag{3.14}$$

with k as the single fitting parameter. The resulting normalized value of k is plotted in Figure 3-9 as a function of the aspect ratio of the stripe. The trend is the same as in Figure 3-6 and the magnitude is similar to f_1 for the case of $\alpha = 0$.

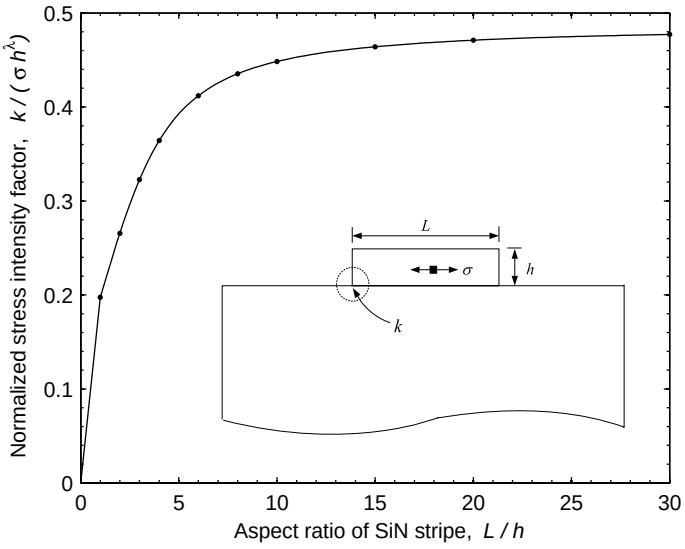

Figure 3-9:The normalized stress intensity factor, $k/(\sigma h^{\lambda})$, is shown as a function of the aspect ratio, L/h, of the nitride stripe.

3.5.2 Criterion of dislocation injection

We now paraphrase a fundamental idea in fracture mechanics (Lawn, 1993). The overall loading is set by the residual stress and the geometry of the stripe, while the atomic process of emitting dislocations occurs within the process zone. The effect of the overall loading on the atomic process is characterized by a single parameter: the stress intensity factor *k*. Consequently, dislocations are emitted from the root when the stress intensity factor reaches a critical value,

$$k = k_c . \tag{3.15}$$

The value of k_c is a constant specific to the materials and the wedge angle (90^0 in this section), but is independent of loading (e.g., the residual stress) and overall geometry (e.g., the thickness and the width of the stripe).

Upon setting $k = k_c$ in Eq. (3.13), we note that the critical condition for the root to emit dislocations depends on the residue stress σ and the feature sizes *h* and *L*. For a given deposition process, the magnitude of the residual stress in the blanket film, σ, is fixed. According to Eq. (3.13), it is more likely for the root to emit dislocations when the stripe is thicker and wider.

Emitting a dislocation is a thermally-activated atomic process, an analysis of which is beyond the scope of this letter. A crude estimate of k_c, however, can be made by letting the resolved shear stress τ_{nb} at distance $r = b$, calculated from Eq. (3.12), equal the theoretical shear strength τ_{th}. For a given slip system with the Burgers vector b_i and the unit normal vector n_i of the slip plane, under a general state of stress σ_{ij}, the resolved shear stress is $\tau_{nb} = \sigma_{ij} n_i b_j / b$. Of the twelve slip systems in Figure 3-1(c), the

two systems $\frac{1}{2}(111)[01\bar{1}]$ and $\frac{1}{2}(111)[10\bar{1}]$ are found to have the largest resolved shear stress, given by

$$\tau_{nb}(r) = \frac{k}{(2\pi r)^{\lambda}} \Sigma_{r\theta}(\theta) \cos 30^0 . \tag{3.16}$$

For the (111) plane, $\theta = -125.27^0$, giving $\Sigma_{r\theta} = -1.0317$.

The theoretical shear strength can be estimated by $\tau_{th} = 0.2\mu$, where μ is the shear modulus of silicon. Setting $|\tau_{nb}(b)| = \tau_{th}$, we obtain that an estimate of the critical stress intensity factor:

$$k_c = 0.5\mu b^{\lambda} . \tag{3.17}$$

We may as well view Eq. (3.17) as a result of a dimensional analysis, leaving the pre-factor adjustable by any specific atomic process of emitting a dislocation.

3.5.3 Experimental observations

A combination of Eqs. (3.13) and (3.17) gives a scaling relation between the critical stress and the feature sizes:

$$\sigma_c = \frac{0.5\mu}{f(L/h)} \left(\frac{b}{h}\right)^{\lambda} . \tag{3.18}$$

From Figure 3-9, when the aspect ratio of the Si_3N_4 stripe varies from 1 to ∞, the function $f(L/h)$ varies in the range $f = 0.2 \sim 0.48$. Taking $\mu = 68.1$ GPa, $b = 3.83$ Å and $h = 1\mu$m, the critical residue stress varies in the range $\sigma_c = 4.9\text{GPa} \sim 2.03\text{GPa}$. If $h = 100$nm, however, the critical stress varies in the range $\sigma_c = 13.8\text{GPa} \sim 5.75\text{GPa}$.

In an experiment by Kammler et al (2005), a Si_3N_4 film, of thickness 500 nm and

residual stress 6 GPa, was grown on a silicon substrate, and was then patterned into large ($10\mu\text{m}\times 10\mu\text{m}$) and small ($1\mu\text{m}\times 1\mu\text{m}$) square pads. Kammler et al showed that dislocations emitted from the large pads, but not from the small ones [experimental picture is shown in Figure 3-10(a)]. According to our Eq. (3.18), the critical stresses for the two cases are 2.8 GPa and 5.0 GPa, respectively.

Isomae (1981) reported that dislocations emitted from the edges of a $3\text{mm}\times 3\text{mm}$ Si_3N_4 pads of thickness 200 nm under residual stress 0.92 GPa. The critical residual stress predicted from Eq. (3.18) is 4.2 GPa. Isomae also observed that dislocations injected into the region of the substrate not covered by the pad [experimental picture is shown in Figure 3-10(b)], and noted that this observation was inconsistent with the concentrated-force model, which predicted that dislocations were equally likely to be emitted on both (111) and $(\bar{1}\,\bar{1}\,1)$ planes. We note that this experimental observation is consistent with the analysis our model. Indeed, the shear stress on the $(\bar{1}\,\bar{1}\,1)$ plane is only 0.26 times that on the (111) plane, since for the $(\bar{1}\,\bar{1}\,1)$ plane, $\theta = -54.73^0$, giving $\Sigma_{r\theta} = -0.266$.

Our model predicts correct trends and orders of magnitude. However, we recognize that the good agreement with some of the experimental observations may be fortuitous. Our procedure to estimate k_c is crude, and can be improved by using more advanced model such as those due to Rice (1992) and others. We also note two effects that can act in opposite directions: thermal activation will decrease the value of k_c, while blunt edge roots will increase the value of k_c.

(a)

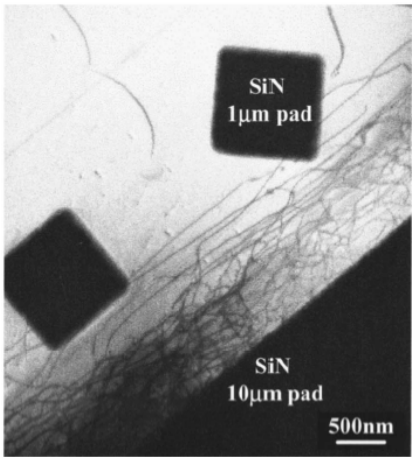

(b)

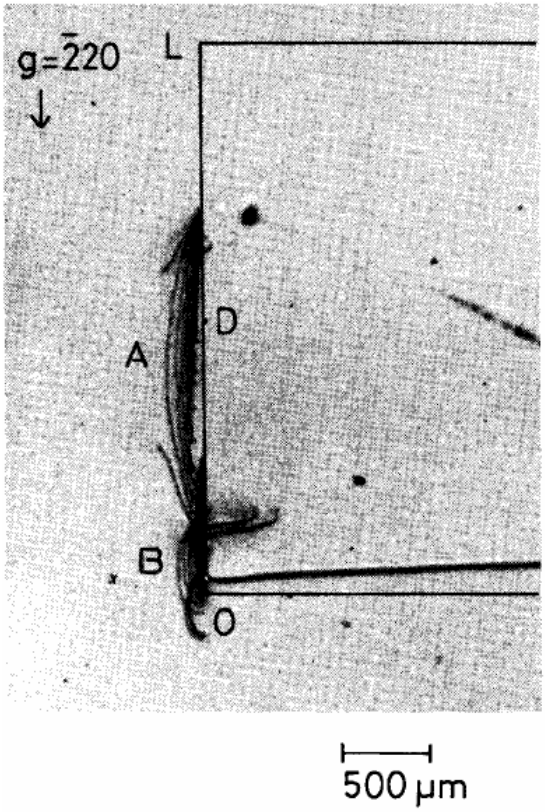

FIG. 14. X-ray traverse topograph of a sample ($\mathbf{g} = \bar{2}20$). In order to observe dislocations generated at the film edge, Si_3N_4 film was removed from the sample using a diluted hydrofluoric acid after heat treatment. Burgers vectors of dislocations *A* and *B* are $a/2[10\bar{1}]$ and $a/2[01\bar{1}]$, respectively.

Figure 3-10:Experimental observations of dislocation injection. (a) Kammler et al. (2005) (b) Isomae (1981).

We should also remark that, given the uncertainty in the sharpness of the edge root in an actual structure, the value of k_c may have a statistical distribution. One may as well forego the unreliable theoretical estimate of k_c, and simply use the experiments, such as those described above, as a means to determine the value of k_c and its statistical distribution. The approach is analogous to that of experimental determination of fracture toughness. Once the statistical distribution of k_c is determined by using samples of one set of σ, h and L, one can predict the statistical distribution of critical values of σ, h and L by using Eq. (3.13). The procedure is analogous to a procedure to evaluate failure statistics of interconnects due to electromigration (He et al., 2004).

3.5.4 Comparison with the results by cohesive zone model

The dislocation emission from a sharp edge can also be considered under Peierls-Nabarro framework (Peierls, 1940; Nabarro, 1947), the same idea as Rice (1992) dealt with dislocation emission from a crack tip. That is, a periodic relation is assumed to hold between shear stress and sliding displacement along a crystal slip plane emanating from the edge, and a solution is then derived for the critical residue stress that corresponds to dislocation nucleation. As we find out in the pervious sections, the slip systems $\frac{1}{2}(111)[01\bar{1}]$ and $\frac{1}{2}(111)[10\bar{1}]$ are most critical, and the resolved shear stress is given by Eq.(3.16). As depicted in Figure 3-11, the simplest periodic relation is Frenkel (1926) sinusoidal function:

$$\tau_{nb} = \frac{\mu b}{2\pi d}\sin\left(\frac{2\pi\delta}{b}\right) \tag{3.19}$$

where μ is the shear modulus, b the Burger's vector, d the spacing of (111) planes, and δ the sliding displacement (or slip) of one atomic plane relative to another at the slip surface. The amplitude is selected such that Eq.(3.19) is reduced to linear elastic relation $\tau_{nb} = \mu\delta / d$ for small deformation. Hence, the cohesive energy γ is the area under the curve from 0 to $b/2$, i.e.,

$$\gamma = \left(\mu b^2\right)/\left(2\pi^2 d\right). \tag{3.20}$$

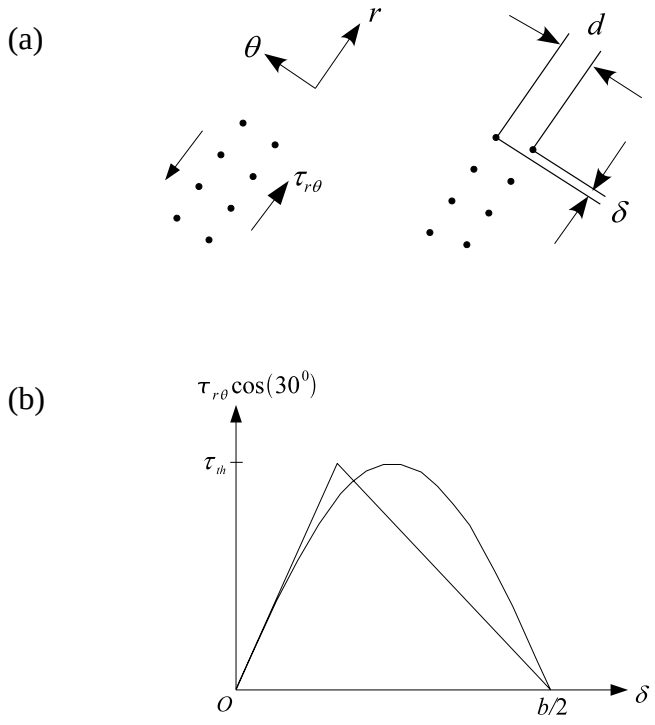

Figure 3-11:(a) Schematic of lattice, showing the measures of relative atomic slip in shear direction. (b) Cohesive zone models are used.

As pointed out in Suo, Ho and Gong (1993), the shape of cohesive zone model is not important, and what matter are the amplitude and the cohesive energy under the curve. In addition, for such a dislocation nucleation problem, the shear stress τ_{nb} has to overcome the shear strength τ_{th} and the relative sliding δ has to attain half of Burger's vector $b/2$, then a full dislocation is nucleated. Hence, in order to easily implement in FEM calculation in ABAQUS6.6, we adopt a triangular shape with height $\tau_{th} = \mu b/(2\pi d)$ and width $b/2$, as shown in Figure 3-11. Hence, the cohesive energy becomes

$$\gamma = (\mu b^2)/(8\pi d). \tag{3.21}$$

which is quite close to Eq.(3.20) based on Frenkel's relation.

Figure 3-12 shows the close-up of finite element mesh around the corner used in calculation. The slip plane (111) is modeled as thin layer with thickness of the lattice spacing, $d_{(111)} = \sqrt{\frac{2}{3}}b$, by cohesive element COH2D4 in green color, and the rest parts by plane strain element CPE4I, SiN in pink and silicon in white.

The numerical results are presented in Figure 3-13, in which the normalized critical residue stress is plotted as a function of aspect ratio. Two curves, one based on singular stress analysis, the other based on cohesive zone model, show the same trend and are quite close to each other with reasonable discrepancy. Hence, we verify the singular stress analysis in some sense. Dislocation nucleation is the behavior at atomic level, while the cohesive zone model is based on continuum mechanics. The singular stress analysis is also from continuum mechanics. They both give correct results with reasonable error.

Note that in FEM, a cohesive element is deleted automatically even if this element

fails only in shearing direction. That is, it not only loses the ability to sustain shear stress, but also the normal stress. Once the cohesive element breaks, it cannot be used to model dislocation any more.

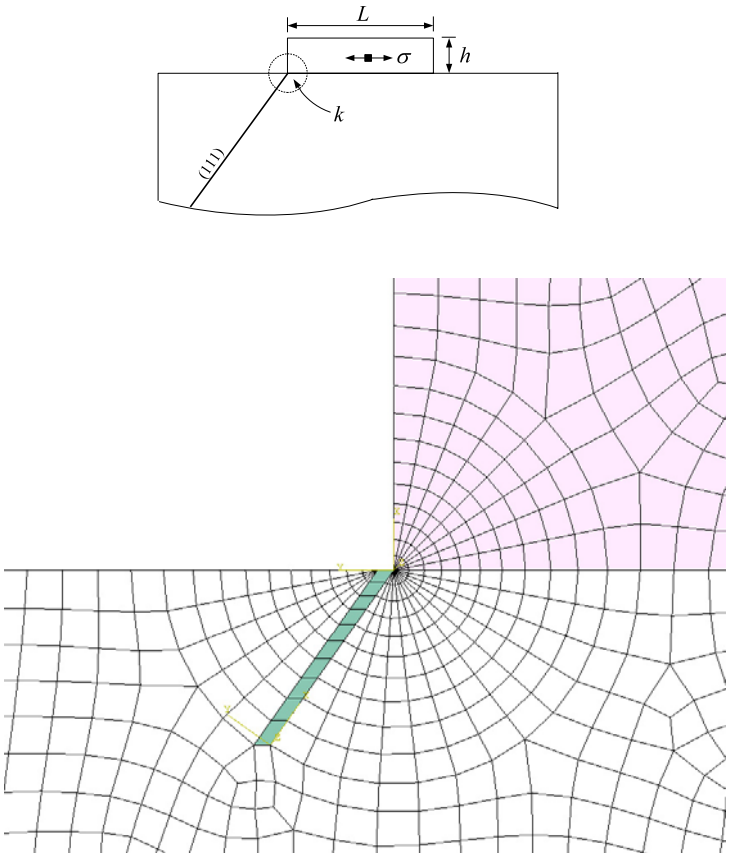

Figure 3-12:The close-up of finite element mesh around the corner used in calculation. The slip plane (111) is modeled as thin layer with thickness of the lattice spacing, $d_{(111)}$, by cohesive element COH2D4, in green color, and the rest parts by solid plane strain element CPE4I, SiN in pink and silicon in white. The inset shows the whole structure.

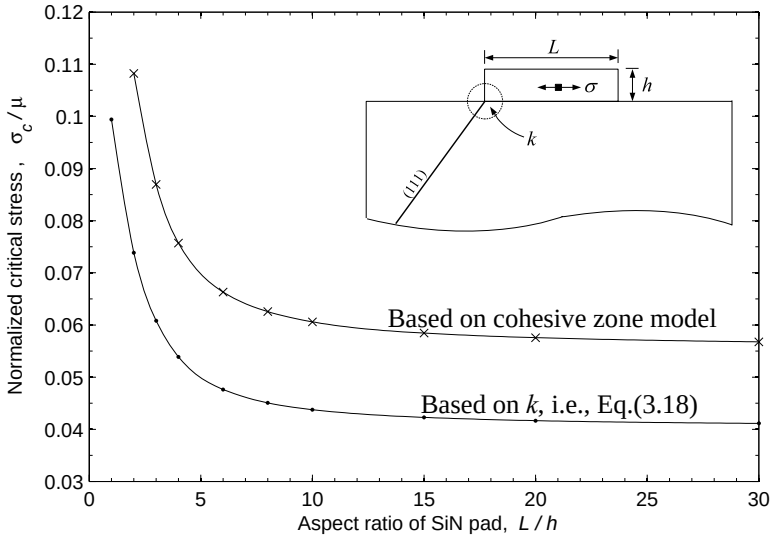

Figure 3-13:The normalized critical stresses, σ_c / μ, calculated using a finite element method based on both stress intensity factor and cohesive zone model, are shown as a function of the aspect ratio, L/h, of the nitride stripe.

3.5.5 Spacing effect in periodic structure

In practice, the SiN stripes or pads are periodically patterned on silicon, so the spacing effect on dislocation injection from sharp features deserves attention. As in Figure 3-14, the SiN stripes with residue stress σ, of width L and thickness h, are periodically patterned with spacing S. Consider one of the corners, the stress field around the corner root is the same as Eq. (3.12), but with the stress intensity factor, k, to be

$$k = \sigma h^{\lambda} f\left(L/h, S/h\right). \tag{3.22}$$

where $\lambda = 0.4514$.

The resulting value of $f\left(L/h, S/h\right) = k/\left(\sigma h^{\lambda}\right)$ is plotted in Figure 3-15 as a function of the ratio of spacing to thickness of the stripe for different aspect ratios L/h=2

and 20. The effect of spacing is quite small for both the large stripe pattern (*L/h*=20) and the small one (*L/h*=2), except that the spacing becomes too small, say $S \le h$. But the effect of aspect ratio (*L/h*) is quite obvious, as shown by the difference between two curves in Figure 3-15, which is consistent with the conclusion in the above subsections.

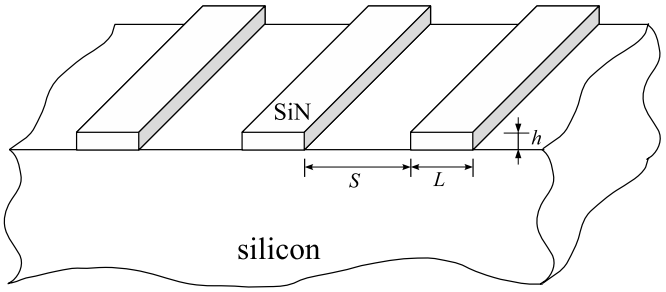

Figure 3-14: The SiN stripes are periodically patterned with spacing *S.*

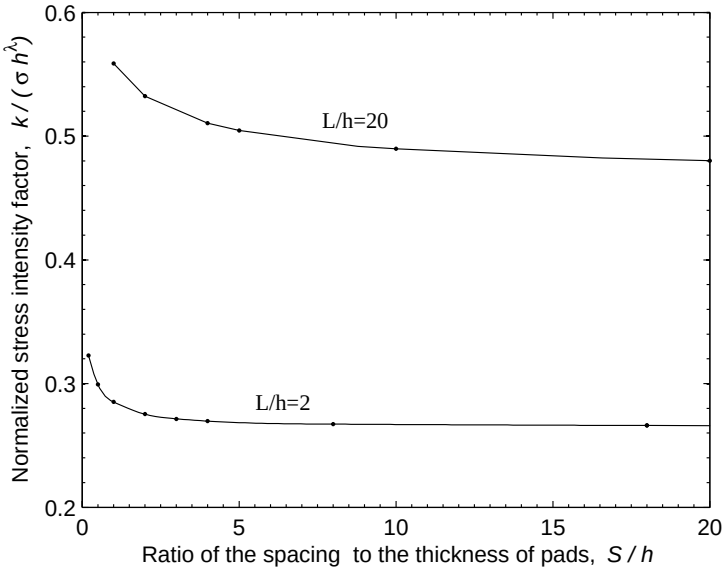

Figure 3-15:The dimensionless function, $f(L/h, S/h)$, is shown as a function of the ratio of spacing to thickness, S/h, of the nitride stripe for $L/h = 2$ and 20.

3.6 Summary

In summary, we have described a method to analyze dislocations emission from sharp features in strained silicon structures based on the singular stress field. The singular stress field at a root of an edge is a linear superposition of two modes, with different exponents. A mode angle is introduced to measure the relative contribution of the two modes to the failure conditions. The two exponents are very different when the film is compliant relative to silicon, and are very similar when the film is stiff relative to silicon. Consequently, the weaker singular field is negligible when the film is compliant, but is significant when the film is stiff. For the full range of the mode angle, we describe a procedure to select the critical slip systems. On the basis of the criterion that dislocations nucleate when the resolved shear stress at distance b from the root of the thin-film edge reaches the theoretical strength, we calculate the critical residual stress in the stripe, and show that the critical stress is low when the stripe is wide or compliant.

For the specific material combination of SiN/silicon, the method predicts the correct orders of magnitude of the critical stress, and gives a scaling relation between the stress level and feature sizes. These predictions call for more systematic comparison between the theory and experiments.

Our approach can be applied to other crystallographic orientations, material combinations, and sharp features. The estimate of k_c may be improved significantly. The approach may ultimately contribute to the design of strained silicon devices.

3.7 Appendix: stress components in polar coordinates and crystal coordinates

The singular stress field Eq.(3.3) is solved by the eigenvalue problem outlined in Bogy (1971) and Liu et al. (1999), the same method as in Section 2.7 of Chapter 2 except different boundary conditions. For the structure as shown in the inset of Figure 3-2, the eigenfunctions $\Sigma_{ij}(\theta)$ associated with the eigenvalue λ are expressed in polar coordinates (r,θ,z) as:

$$\Sigma_{rr}(\theta) = -(\lambda-1)\begin{Bmatrix}(\lambda-2)[A\sin(\lambda-2)\theta + B\cos(\lambda-2)\theta] \\ +(\lambda+2)[C\sin\lambda\theta + D\cos\lambda\theta]\end{Bmatrix}, \tag{3.20}$$

$$\Sigma_{\theta\theta}(\theta) = (\lambda-1)(\lambda-2)\begin{bmatrix}A\sin(\lambda-2)\theta + B\cos(\lambda-2)\theta \\ +C\sin\lambda\theta + D\cos\lambda\theta\end{bmatrix}, \tag{3.21}$$

$$\Sigma_{r\theta}(\theta) = (\lambda-1)\begin{Bmatrix}(\lambda-2)[A\cos(\lambda-2)\theta - B\sin(\lambda-2)\theta] \\ +\lambda[C\cos\lambda\theta - D\sin\lambda\theta]\end{Bmatrix}, \tag{3.22}$$

$$\Sigma_{zz}(\theta) = -4\nu(\lambda-1)[C\sin\lambda\theta + D\cos\lambda\theta], \tag{3.23}$$

$$\Sigma_{rz} = \Sigma_{\theta z} = 0. \tag{3.24}$$

The eigenvalue λ and its associated coefficients *A, B, C* and *D* in the film and the substrate are solved by the following boundary conditions:

1). On $\theta = 0$, tractions and displacements are continuous,

$$\sigma_{\theta\theta}^{f} = \sigma_{\theta\theta}^{s}\big|_{\theta=0},\ \tau_{r\theta}^{f} = \tau_{r\theta}^{s}\big|_{\theta=0},\ u_{\theta}^{f} = u_{\theta}^{s}\big|_{\theta=0},\ u_{r}^{f} = u_{r}^{s}\big|_{\theta=0} \tag{3.25}$$

2). On $\theta = \pi/2$, tractions are free,

$$\sigma_{\theta\theta}^{f}\big|_{\theta=\frac{\pi}{2}} = 0,\ \tau_{r\theta}^{f}\big|_{\theta=\frac{\pi}{2}} = 0 \tag{3.26}$$

3). On $\theta = -\pi$, tractions are free,

$$\sigma^{s}_{\theta\theta}\Big|_{\theta=-\pi} = 0,\ \tau^{s}_{r\theta}\Big|_{\theta=-\pi} = 0 \tag{3.27}$$

where the superscripts f and s indicates film and substrate, respectively.

In this chapter, the singular stress field in the silicon substrate around the root of the edge causes dislocation to be emitted, so that the eigenvalues and the associated coefficients only in the silicon substrate are listed in Table 3-2 (for $\alpha = 0.5$, 0, -0.5 with $\beta = 0$).

In calculating the resolved shear stress Eq.(3.6), the stress components in the crystal coordinates (x_1, x_2, x_3), σ_{ij}, are converted from those in the polar coordinates (r, θ, z). The relation of (x_1, x_2, x_3) and (r, θ, z) is depicted in Figure 3-1, and the matrix of conversion is

$$[Q] = \begin{bmatrix} -\cos\theta/\sqrt{2} & -\cos\theta/\sqrt{2} & \sin\theta \\ \sin\theta/\sqrt{2} & \sin\theta/\sqrt{2} & \cos\theta \\ -1/\sqrt{2} & 1/\sqrt{2} & 0 \end{bmatrix} \tag{3.28}$$

From $[\sigma]_{crystal} = [Q]^T [\sigma]_{polar} [Q]$, the stress components in crystal coordinates are

$$\sigma_{11} = \sigma_{22} = \left(\sigma_{rr}\cos^2\theta + \sigma_{\theta\theta}\sin^2\theta + \sigma_{zz} - \sigma_{r\theta}\sin 2\theta\right)/2 \tag{3.29}$$

$$\sigma_{12} = \sigma_{21} = \left(\sigma_{rr}\cos^2\theta + \sigma_{\theta\theta}\sin^2\theta - \sigma_{zz} - \sigma_{r\theta}\sin 2\theta\right)/2 \tag{3.30}$$

$$\sigma_{13} = \sigma_{31} = \sigma_{23} = \sigma_{32} = \left[\left(\sigma_{\theta\theta} - \sigma_{rr}\right)\sin 2\theta - 2\sigma_{r\theta}\cos 2\theta\right]/2\sqrt{2} \tag{3.31}$$

$$\sigma_{33} = \sigma_{rr}\sin^2\theta + \sigma_{\theta\theta}\cos^2\theta + \sigma_{r\theta}\sin 2\theta \tag{3.32}$$

Table 3-2: Singularity exponents and the associated coefficients in Eqs.(3.20)–(3.24) in silicon substrate for $\alpha = 0.5$, 0, -0.5 with $\beta = 0$.

α	-0.5		0		0.5	
λ	0.4314	0.0168	0.4555	0.0915	0.4783	0.2542
A	0.9803	-0.3775	0.9885	0.1427	0.9951	0.4213
B	0.2687	-9.6738	0.3695	-1.9826	0.4717	-0.9088
C	-0.5123	-105.1100	-0.6804	-9.0562	-0.8414	-2.3815
D	1.8693	4.1015	1.8201	-0.6517	1.7750	-1.1040

References:

1. A.R. Akisanya and N.A. Fleck, Int. J. Solids Structures **34**, 1645 (1997).
2. D. B. Bogy, J. Appl. Mech. **38**, 377 (1971).
3. M. Dellith, G.R. Booker, B.O. Kolbesen, W. Bergholz, and F. Gelsdorf, J. Electrochem. Soc. **143**, 210 (1996).
4. J. Dundurs, J. Appl. Mech. **36**, 650-652 (1969).
5. M.L. Dunn, C.Y. Hui, P.E.W. Labossiere and Y.Y. Lin, Int. J. Fract. **110**, 101 (2001).
6. J. Frenkel, Z. Phys. **37**, 572 (1926).
7. J. He, Z. Suo, T.N. Marieb, J.A. Maiz, Appl. Phys. Lett. **85**, 4639 (2004).
8. J. P. Hirth and J. Lothe, *Theory of dislocation*, 2nd ed. (Krieger Publishing Company, Malabar, Florida, 1992), p. 6.
9. C.Y. Hui and A. Ruina, Int. J. Fracture **72**, 97 (1995).
10. S. M. Hu, Appl. Phys. Lett. **32**, 5 (1978); J. Appl. Phys. **50**, 4661 (1979); **70**, R53 (1991).
11. M. Ieong, B Doris, J. Kedzierski, K. Rim, and M. Yang, Science **306**, 2057 (2004).
12. S. Isomae, J. Appl. Phys. **52**, 2782 (1981).
13. S.C. Jain, H.E. Maes, K. Pinardi, and I. De Wolf, J. Appl. Phys. **79**, 8145 (1996).
14. H.T. Johnson and L.B. Freund, J. Appl. Phys. **81**, 6081 (1997).
15. M. Kammler, D. Chidambarrao, K.W. Schwarz, C.T. Black, and F.M. Ross, Appl. Phys. Lett. **87**, 133116 (2005).

16. P.E.W. Labossiere, M.L. Dunn, and S.J. Cunningham, J. Mech. Phys. Solids **50**, 405 (2002).

17. B. Lawn, *Fracture of Brittle Solids*, 2nd ed., (Cambridge University Press, Cambridge, UK, 1993).

18. X. H. Liu, Z. Suo, and Q. Ma, Acta Mater. **47**(1), 67 (1999).

19. N. Lu, J. Yoon and Z. Suo, Int. J. Mat. Res., 2007 (in press).

20. M. Miyake and M. Takahashi, J. Electrochem. Soc. **144**, 1020 (1997).

21. I. Mohammed And K.M. Liechti, J. Mech. Phys. Solids **48**, 735 (2000).

22. F.R.N. Nabarro, Proc. Phys. Soc. **59**, 256 (1947).

23. R.E. Peierls, Proc. Phys. Soc. **52**, 34 (1940).

24. E.D. Reedy, Int. J. Solids Struct. **37**, 2429 (2000).

25. J.R. Rice, J. Appl. Mech. **55**, 98 (1988).

26. J.R. Rice, J. Mech. Phys. Solids, **40**(2), 239 (1992).

27. K.W. Schwarz and D. Chidambarrao, J. Appl. Phys. **85**, 7198 (1999).

28. Z. Suo, S. Ho, and X. Gong, J. Eng. Mat. Tech. **115**, 319 (1993).

29. W. Suwito, M. L. Dunn, S. J. Cunningham, and D. T. Read, J. Appl. Phys. **85**, 3519 (1999).

30. J. Vanhellemont, S. Amelinckx and C. Claeys, J. Appl. Phys. **61**, 2170 (1987); **61**, 2176 (1987); **63**, 5703 (1988).

31. M.L. Williams, J. Appl. Mech. **19**(4), 526 (1952).

32. Z. Zhang, J. Yoon, and Z. Suo, Appl. Phys. Lett. **89**, 261912 (2006).

33. Z. Zhang and Z. Suo, Int. J. Solids Struct. **44,** 4559 (2007).

Chapter 4 Chip-Package Interaction and Interfacial Delamination

In flip-chip package, the mismatch of thermal expansion coefficients between the silicon die and packaging substrate induces concentrated stress field around the edges and corners of silicon die during assembly, testing and services. The concentrated stresses result in delamination on many interfaces on several levels of structures, in various length scales from tens of nanometers to hundreds of micrometers. A major challenge to model flip-chip packages is the huge variation of length scales, the complexity of microstructures, and diverse materials properties. In this chapter, we simplify the structure to be silicon/substrate with wedge configuration, and neglect the small local features of integrated circuits. This macroscopic analysis on package level is generic with whatever small local features, as long as the physical processes of interest occur in the region where the concentrated stress field due to chip-packaging interaction dominates. Because it is the same driving force that motivates all of the flaws. Therefore, the different interface cracks with same size and same orientation but on different interfaces should have similar energy release rates provided that the cracks are much

smaller than the macroscopic length. We calculate the energy release rate and the mode angle of crack on the chip-package interface based on the asymptotic linear elastic stress field. In a large range of crack length, the asymptotic solution agrees with finite element calculation very well. We discuss the simplified model and results in context of real applications.

4.1 Introduction

After integration of billions of transistors, capacitors, resistors, inductors, etc. on its surface, the silicon die is flipped over facedown and connected to substrate by solder joints array, with the gap filled by underfill. This is so called “flip-chip package”, as shown in Figure 4-1(a). In such a package, the length scale of functional electronic components varies from centimeters to nanometers. The packaging substrate is several centimeters wide and about 1 mm thick. The silicon die is about 1 cm wide and 0.8 mm thick. The size of solder joints and the thickness of underfill are about tens of microns in the current technology and will be smaller in the future [Figure 4-1(b)]. If we look into the interconnects on the silicon die, the width and thickness of copper line are about tens of nanometers [Figure 4-1(c)]. The smallest transistor channel length can be several nanometers.

(a)

(b)

(c)

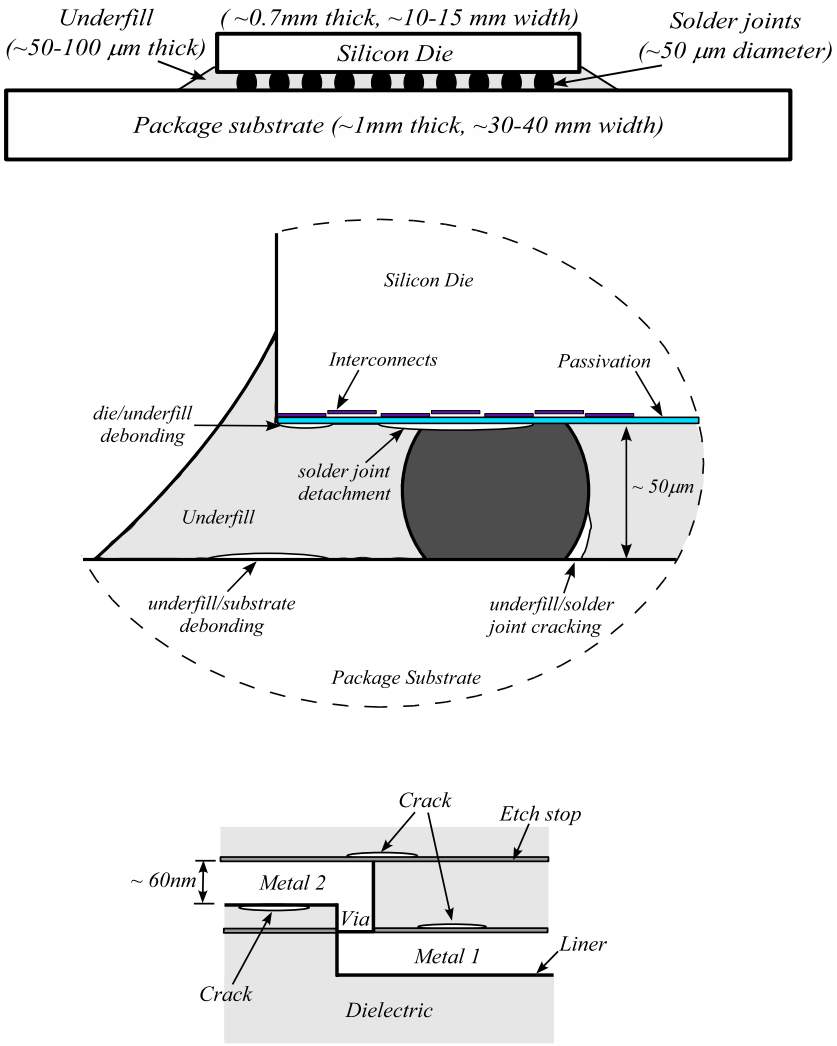

Figure 4-1:(a) Typical structure of flip-chip package. The Cu/low-*k* interconnects are integrated on the silicon die and passivated, then silicon die is flipped upside down and bonded to substrate by solder joints array, with the gap filled by underfill material. (b) Magnified view of chip-package corner with typical failures phenomena is illustrated. The flaw size is about tens of microns. (c) Magnified view of Cu/low-*k* interconnects around the die corner with typical interfacial delamination is depicted. The flaw size is about tens of nanometers.

As the market demands on maximum performance and minimum cost, new designs, materials and processes are employed from transistor level to package level in the length scale from nanometer to centimeter. For example, the source/drain channel in silicon is strained to increase the mobility of electrons or holes (Ieong et al., 2004). The Al/SiO_2 interconnects with shunt layer has been replaced by Cu/low-permittivity dielectrics dual-damascene interconnects to reduce the Resistance-Capacitance delay (Murarka, 1997). The number of silicon-to-package interconnects have increased more than six times over the past 5 years. The scaling demands are driving the size and pitch of solder joints to the limits of current technologies, shrinking from hundreds of microns to tens of microns. The packaging substrate changed from ceramic to organic laminates in the mid of 1990s for better performance at a lower cost because organic substrates are of lower dielectric constant and easy to process metallization (Atluri et al., 2003). In addition, the mismatch in coefficient of thermal expansion (CTE) between organic substrate and plastic motherboard is also reduced. More information can be found in a multi-author review of the microelectronics packaging and integration in MRS bulletin, edited by Reuss and Chalamala (2003).

However, as new technologies advance, new reliability challenges appear. On the package level, the large CTE mismatch between silicon die and organic substrate can induce bending or warping of the package during thermal excursion from packaging temperature (about 165^oC) to room temperature. Also huge stresses concentrate around the edges and corners of silicon die during packaging assembly, thermal cyclic testing and services. The huge stresses result in many failure modes as shown in Figure 4-1(b), such as the debonding of the interfaces of die/underfill, underfill/substrate or

underfill/solder joints (Semmens et al., 1998; Rzepka et al., 1998; Chen et al., 2001; Fan et al., 2001; Hirohata et al., 2002; Zhai et al., 2004); solder joints detachment or cracking (Zhang et al 2000; Chen et al., 2001; Zhai et al, 2003; Tummala et al., 2004); dielectric cracking, copper trace cracking, and die cracking (Tummala et al., 2004). On the interconnects level, as shown in Figure 4-1(c), the interfacial delamination of back-end-of-line (BEoL) (Mercado et al., 2003; Wang et al., 2003; Liu et al., 2007) becomes serious. On one hand, this is because the global CTE mismatch between silicon die and organic substrate on package level becomes larger compared to traditional combination of silicon die/ceramic substrate, meanwhile the local CTE mismatch between Cu and low-permittivity dielectrics on interconnects level also becomes larger. On the other hand, the low-permittivity dielectrics (e.g. CDO) is of low cohesive and adhesive energy, and so more susceptible to cracking and debonding.

A major challenge to model or simulate flip-chip packages is the huge variation in length scales, from several centimeters to tens of nanometers, with five or six orders of magnitude difference. Besides, the complication of structures and diverse materials interaction makes the modeling and simulation even harder. To overcome these difficulties, multi-scale FEM simulation or so-called global-local submodeling approach is adopted by many researchers to reconcile the huge length scale variation, such as Gu et al (2001), Mercado et al. (2003), and Wang et al. (2003). However, the simulation itself is hard and expensive.

As well known, the failure modes mentioned above become serious or more critical after packaging (Wang et al., 2003), especially with the use of organic substrate. The concentrated stresses around the edges and corners of silicon die due to die-package

mismatch are the *global* driving force; the stresses arising due to the local mismatch of materials' properties are *local* driving force (e.g. the stresses in stand-alone wafer before packaging). The local driving force is usually much smaller than global driving force (Wang et al., 2003). Hence, in this chapter, we will study the global driving force on interfacial delamination by analyzing the relation between the interface crack and the asymptotic singular stress field around the edges or corners of silicon die on package level. The delamination can occur at any possible site in this domain, including the examples shown in Figure 4-1(b) and 1(c). The relation is quite generic in the following sense. The linear elastic asymptotic singular stress solution matches the exact solution in a zone about one fifth or one quarter of the die thickness, i.e., the length scale is about 0.2mm. The flaw size in this zone can be as big as the size of solder joints, or can be as small as the width of Cu lines in interconnects. That is, the flaw size varies from tens of microns to nanometers, but is small compared to the singular stress region. So the physical processes of interest occur in the region where asymptotic singular stress solution applies. It is the same driving force that motivates all of the flaws to grow. The different interface cracks with same size and same orientation should have similar energy release rates but different fracture toughness. Hence, we adopt the simplified model as shown in Figure 4-2 to consider the interfacial delamination on package level. This macroscopic analysis is generic and the results are able to characterize chip-package interaction with whatever local features, such as solder joints, underfill, interconnects, as long as they are small.

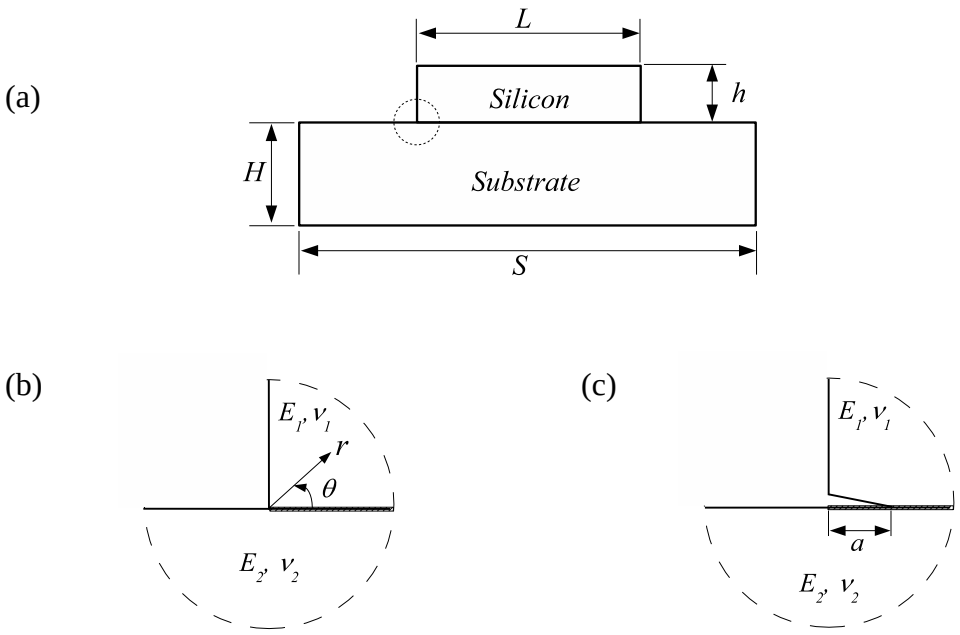

Figure 4-2: Geometry used in calculations: (a) Silicon die on package substrate; (b) Geometry near the die edge. (c) A preexisting small interface crack in the corner.

Following the introduction section, Section 4.2 briefly recaps the singularity features of bimaterial wedge and mode mixity. Section 4.3 investigates the interface delamination driven by the singular stress field due to chip-package interaction under thermal excursion. In Section 4.4, we compare with three-dimensional multi-level submodeling calculation by others, and discuss the validity of the simplified model and other related issues. Section 4.5 summarizes the main points.

4.2 Split singularities and local mode mixity

For a bimaterial wedge as the inset of Figure 4-3, the split singularities were

studied in Chapter 3, here we just recap the main features (Liu et al., 1999; Feron et al., 2007). Figure 4-3 plots the contours of the exponents on the (α, β) plane. The parallelogram is divided into two regions by a dark curve. In the lower-left region, the exponents are two unequal real numbers, one stronger (λ_1) and the other weaker (λ_2). The values for λ_1 are labeled horizontally, and those for λ_2 are labeled vertically. In the whole region, $\lambda_2 < \lambda_1 \le 0.5$. In the upper-right region, the exponents are a pair of complex conjugates, $\lambda_{1,2} = \xi \pm i\varepsilon$. The real part is depicted by solid lines and labeled horizontally, while the imaginary part is depicted by dashed lines and labeled vertically. At each point on the boundary (i.e., the dark curve), the two exponents degenerate to one number: when the point is approached from a region of real exponents, the two real exponents become identical; when the point is approached from a region of complex-conjugate exponents, the imaginary part vanishes.

Once we retain the two unequal real exponents, the stress field around the root of the wedge is a linear superposition of the two modes:

$$\sigma_{ij}(r,\theta) = \frac{k_1}{(2\pi r)^{\lambda_1}} \Sigma_{ij}^1(\theta) + \frac{k_2}{(2\pi r)^{\lambda_2}} \Sigma_{ij}^2(\theta). \tag{4.1}$$

The angular functions $\Sigma_{ij}^1(\theta)$ and $\Sigma_{ij}^2(\theta)$ are normalized such that $\Sigma_{r\theta}^1(0) = \Sigma_{r\theta}^2(0) = 1$, the same as what we did in Chapter 3. Similarly, if we assume the size of fracture process zone is Λ and the typical macroscopic length is the die thickness, *h*. Then, the singular stress field (4.1) is valid within the *k*-annulus of some radii bounded between Λ and *h*, only if $\Lambda << h$.

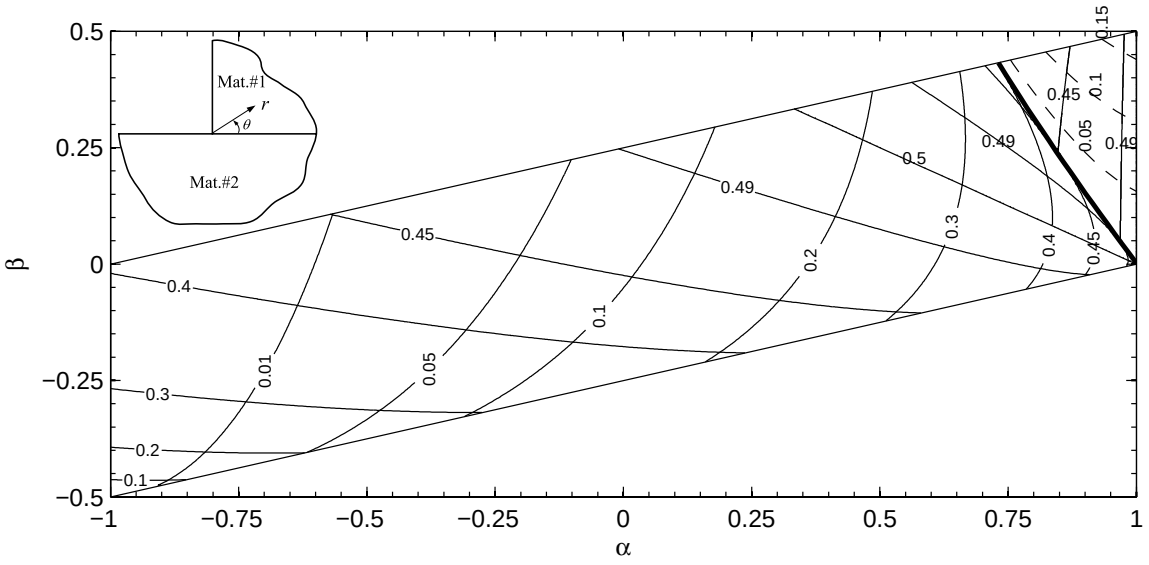

Figure 4-3: The inset shows the root of an edge of silicon die bonded on a substrate. Contours of the singular exponents are plotted on the plane of Dundurs parameters (α, β). The parallelogram is divided into two regions by a dark curve. In the lower-left region, the exponents are two unequal real numbers, with the larger one labeled horizontally, and the smaller one labeled vertically. In the upper-right region, the exponents are a pair of complex conjugates, with real part depicted by solid lines and labeled horizontally, and the imaginary part depicted by dashed line and labeled vertically.

The two stress intensity factors, k_1 and k_2, have different dimensions, being $(\text{stress})(\text{lengh})^{\lambda_1}$ and $(\text{stress})(\text{lengh})^{\lambda_2}$, respectively. As discussed in Chapter 2, the mode mixity is length dependent, and can be described by $(k_2/k_1)r^{\lambda_1-\lambda_2}$, so long as the distance *r* is chosen. The microscopic processes of fracture occur within the process zone, but are driven by the singular stress field (4.1) in the *k*-annulus. In discussing the relative

contribution of the two modes to the failure processes at length scale Λ, we use *local mode mixity*:

$$\eta = (k_2 / k_1)\Lambda^{\lambda_1 - \lambda_2}. \tag{4.2}$$

a dimensionless parameter defined in Chapter 2, as the measure of mode mixity.

4.3 Interfacial delamination due to chip-package interaction

We now analyze the delamination of chip-package interface. Consider two kinds of packages: flip-chip on ceramic substrate, and flip-chip on organic substrate. The typical organic substrate is epoxy-based laminates, such as FR4 or BT. However, the organic packages have fundamental limits, and so novel ceramic substrates are demanded (Tummala et al., 2004). Low Temperature Co-fired Ceramic (LTCC), a ceramic-glass composite with small CTE mismatch with silicon die, is the potential choice of package substrate (Frear and Thomas, 2003). LTCC is fired at sufficiently low temperature that Cu can be used in the metallization; and it offers the hermeticity and mechanical stability. We will use chip/FR4 and chip/LTCC packages as two typical examples to study the interfacial delamination due to chip-package interaction under thermal excursion from 165^0C to 25^0C. The material properties used in calculation are listed in Table 4-1. The geometric parameters are specified as $h = 0.7$ mm, $H = 1.65$ mm, $L = 10$ mm and $S = 20$ mm, as shown in Figure 4-2(a).

Table 4-1: Materials properties used in calculation.

	E (GPa)	ν	α (10^{-6} / ^{o}C)
Silicon	130	0.28	3.3
FR4 or BT [a)]	23	0.3	15
LTCC [b)]	120	0.3	5.8
Underfill	6	0.32	36
Solder	26	0.35	24

a) Both FR4 and BT are epoxy-based organic substrates.

b) Low Temperature Co-fired Ceramic.

For either chip/FR4 package or chip/LTCC package, we calculate the full stress field in the structure, i.e. Figure 4-2(a), by using the finite element code ABAQUS6.6, then fit the interfacial shear stress close to the root, say $10^{-3} < r/h < 10^{-2}$, to the equation

$$\sigma_{r\theta}(\theta = 0) = \frac{k_1}{(2\pi r)^{\lambda_1}} + \frac{k_2}{(2\pi r)^{\lambda_2}}. \tag{4.3}$$

with k_1 and k_2 as fitting parameters.

For this chip-package structure under thermal excursion, the bi-axial stress state in the silicon die away from the edges is $\sigma = E_{Si}\Delta\alpha\Delta T/(1-\nu_{Si})$, where $\Delta\alpha = \alpha_{sub} - \alpha_{Si}$, and $\Delta T = 140\ ^{0}$C. Linearity and dimensional considerations dictate that the two stress intensity factors should take the form

$$k_1 = \kappa_1 \sigma h^{\lambda_1}, \quad k_2 = \kappa_2 \sigma h^{\lambda_2}. \tag{4.4}$$

where κ_1 and κ_2 are dimensionless coefficients, h the silicon die thickness.

Assume an interfacial flaw preexists, as shown in Figure 4-2(c). The crack length

a is much smaller than die thickness h, i.e., $a << h$. The length Λ now is identified with the length a of the small crack, so that the local mode mixity is

$$\eta = (k_2 / k_1) a^{\lambda_1 - \lambda_2} = (\kappa_2 / \kappa_1)(a / h)^{\lambda_1 - \lambda_2}. \tag{4.5}$$

which describes the relative contribution of two modes at the length scale of crack size.

The stress field at the interfacial crack tip is characterized by the complex stress intensity factor K, which is related to the stress intensity factors of the wedge (k_1, k_2) linearly as follows:

$$\frac{\mathrm{Re}\left(K a^{i\varepsilon}\right)}{\sqrt{a}} = c_{11} \cdot \frac{k_1}{a^{\lambda_1}} + c_{12} \cdot \frac{k_2}{a^{\lambda_2}}. \tag{4.6}$$

$$\frac{\mathrm{Im}\left(K a^{i\varepsilon}\right)}{\sqrt{a}} = c_{21} \cdot \frac{k_1}{a^{\lambda_1}} + c_{22} \cdot \frac{k_2}{a^{\lambda_2}}. \tag{4.7}$$

where $\varepsilon = 1/(2\pi) \ln\left[(1-\beta)/(1+\beta)\right]$. The coefficients c_{11}, c_{12}, c_{21} and c_{22} only depend on material combination (α, β) and wedge angle (90^o in this study), and are tabulated in Table 4-2. The determination of the coefficients is stated in Appendix.

For such a bimaterial wedge configuration, the coefficients c_{11}, c_{12}, c_{21} and c_{22} are generic for any macroscopic structure, external loading, and boundary condition. Once we obtain them for the specific material combination (e.g., silicon/FR4 or silicon/LTCC), we can use them for different geometric parameters (e.g., die thickness) and loadings (e.g. thermal excursion, bending, etc.). This is an advantage compared to multi-scale submodeling approach, in which we have to recalculate again and again in order to study the parameter dependence.

Table 4-2: Coefficients c_{11}, c_{12}, c_{21} and c_{22} for two types of flip-chip packages.

Flip-chip package	α	β	λ_1	λ_2	c_{11}	c_{12}	c_{21}	c_{22}
Chip/FR4	0.696	0.196	0.499	0.318	0.951	-1.206	0.922	1.443
Chip/LTCC	0.034	0	0.457	0.100	1.965	-5.418	0.870	2.270

From Eqs. (4.4) to (4.7), the energy release rate G and the mode angle ψ of interfacial delaminated crack are:

$$G = \frac{1-\beta^2}{1-\alpha}\frac{\kappa_1^2\sigma^2 h}{\bar{E}_{Si}}\left(\frac{a}{h}\right)^{1-2\lambda_1}\left[\left(c_{11}+c_{12}\eta\right)^2+\left(c_{21}+c_{22}\eta\right)^2\right]. \tag{4.8}$$

and

$$\tan\psi = \frac{\mathrm{Im}\left(Ka^{i\varepsilon}\right)}{\mathrm{Re}\left(Ka^{i\varepsilon}\right)} = \frac{c_{21}+c_{22}\eta}{c_{11}+c_{12}\eta}. \tag{4.9}$$

To obtain G and ψ under any loading case, we just need to find out two stress intensity factors, k_1 and k_2. Then plug into Eqs.(4.8) and (4.9), we have G and ψ for any arbitrary interfacial flaw size a, only if $a << h$. In order to verify the relations given by Eqs.(4.8) and (4.9), we use finite element method (FEM) to directly calculate G and ψ of interfacial crack with different crack length a in the range of $10^{-4} < a/h < 10^{0}$ for both chip/FR4 and chip/LTCC packages under the thermal excursion from 165^0C to 25^0C. In order to plot Eqs.(4.8) and (4.9), we use FEM to calculate the stress field under the same thermal excursion of the full structure without crack [Figure 4-2(a)], and obtain κ_1 and κ_2 by curve fitting Eq.(4.3) with dimensional consideration of Eq.(4.4). For

chip/FR4 package, $\kappa_1 = -0.05$ and $\kappa_2 = -0.06$; for chip/LTCC package, $\kappa_1 = -0.23$ and $\kappa_2 = -0.11$.

In Figure 4-4, energy release rate *G* and mode angle ψ of interfacial crack are plotted as a function of normalized crack length *a/h* for both chip/FR4 and chip/LTCC packages under thermal excursion from 165^0C to 25^0C. The curves are plotted from Eqs.(4.8) and (4.9), and the data points with markers are from finite element calculation in ABAQUS6.6 by contour integral. For both packages, the FEM data and Eqs.(4.8) and (4.9) agree with each other very well when $a/h < 0.1 \sim 0.2$, i.e. the *k*-annulus regime, within which the asymptotic solution Eq.(4.1) applies. For chip/FR4 package, the shear mode dominates in the range of crack length, while for chi/LTCC package, the opening mode plays more role. As we know, the driving force is due to CTE mismatch of die-package. Hence, the energy release rate of interface flaws in chip/FR4 package is much larger than that in chip/LTCC package.

(a)

(b)

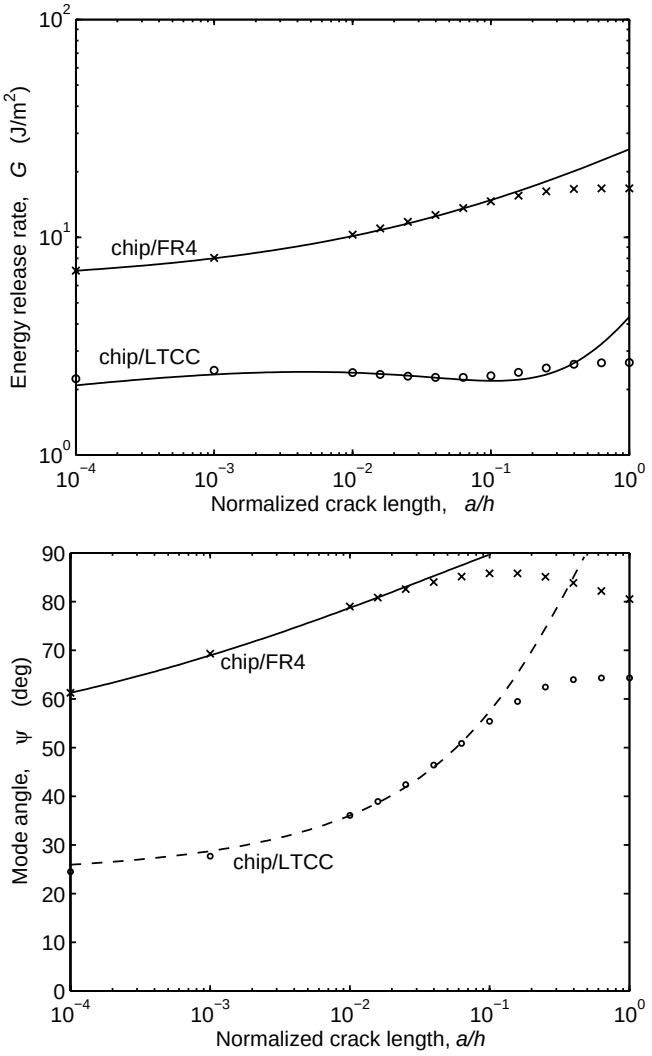

Figure 4-4: Energy release rate (a) and mode angle (b) of interfacial crack are plotted as a function of normalized crack length *a/h* for both chip/FR4 and chip/LTCC packages under thermal excursion from 165^0C to 25^0C. The curves are plotted from Eqs.(4.8) and (4.9), and the data points with markers are read out from finite element calculation in ABAQUS by contour integral.

4.4 Discussion

4.4.1 Global driving force and local driving force

In our model, we neglect the small local features, such as solder joints, underfill, Cu/low-*k* interconnects, etc., and also we neglect the elastic or CTE mismatch among them, since these small features and the associated local mismatch make less contribution to interfacial delamination provided that the global driving force dominates. For example, both Wang et al. (2003) and Liu et al. (2007) shown that the energy release rate of horizontal interfacial flaws within the Cu/low-*k* interconnects are about 1 J/m^2 or less under the typical thermal loading condition if the silicon die is standing alone. On the contrary, the energy release rate increases one order of magnitude larger after being packaged to the organic substrate. Therefore, neglecting the small features and local mismatch in interconnects, we can still obtain an accurate value by doing a macroscopic analysis on package level. Let us consider the following case. The flaws in interconnects are about 100 nm or less, the die thickness is about 1 mm, i.e. $a/h \sim 10^{-4}$, so the energy release rate is around 10 J/m^2 for chip/FR4 package, which is close to the values given by 3D multi-level submodeling technique in Wang et al. (2003).

Length scale varies five to six order of magnitude from interconnects level to package level. So does the size of the interfacial flaws. Our model supplies a reasonable estimate of energy release rates of interfacial flaws with huge variation in length scale without complexity of microstructures and diverse materials. This is based on the following argument. From the perspective of package level, asymptotic singular stress field (4.1) arises due to the CTE mismatch of silicon die and package substrate. The

stress intensity factors, k_1 and k_2, carrying information of macroscopic structure and loading condition, are independent of microstructures. As long as the crack growth under the global driving force is concerned, the energy release rates of interfacial cracks with same size and same orientation but on different interfaces have similar values only if they are much smaller than macroscopic length.

In order to improve the reliability of interconnects, the reduction of global driving force is one big gain. As shown in Figure 4-4(a), the replacement of compliant organic substrate (e.g., FR4) by stiff ceramic with small CTE (e.g. LTCC) decreases the energy release rate multiple-fold.

4.4.2 Underfill effect

In our model, we neglect the underfill effect. However, this effect could be significant (Suryanarayana et al., 1991; Rzepka et al., 1998; Chen et al., 2001; Zhai et al., 2004). Because in the previous technology, the size of solder joints and the thickness of underfill are over 100μm and the thickness of silicon die is about 700μm, therefore the underfill acts as a thick buffer to alleviate the concentrated stresses. From Figure 4-4, for chip/FR4 package, the energy release rate is about 20J/m^2 if the crack length is about 0.1h, which represents a typical crack along the die/underfill interface. However, this value could be reduced five-fold if underfill is considered (Zhai et al., 2004). In this case, we have to include underfill in our model to study such a wedge configuration that two-layered materials sit on substrate.

However, this buffer effect is tapering. Because the technology demands denser solder joints with smaller pitch and smaller size on the similar size of silicon die, and results in the decrease of the underfill thickness, which will be the case as our model

represents. Finally, this trend increases the global driving force.

The fillet height of underfill around the die corner can affect the reliability of the crack along the die/underfill interface (Zhai et al., 2004). This phenomenon can be explained qualitatively in the following, and more details can be found in Chapter 5. Physically the stress concentration around the wedge is due to the elastic mismatch and geometric discontinuity in this domain. If we use a fillet, the bimaterial wedge becomes a tri-material junction as shown in Figure 5-2(b), the singularity exponent λ becomes usually much smaller (Pageau et al., 1994).

In order to address our idea clearly, we do not use fillet. Therefore, the crack is edge crack. If fillet is considered, the crack is fully embedded. So the energy release rate should be smaller. More detailed study of fillet effect is beyond the scope of this chapter.

4.4.3 Relation of *k*-field and *K*-field

Eqs (4.8) and (4.9) agree with FEM data very well when crack size a is less than $0.2h$, as shown in Figure 4-4. If the crack becomes longer, Eqs. (4.8) and (4.9) goes away from FEM data. It can be understood as follows. The singular stress field of interfacial crack tip, characterized by complex stress intensity factor K, scales with the crack size. The singular stress field of 90^0 wedge, characterized by stress intensity factors k_1 and k_2, scales with the die thickness. When the crack is small, the K-field is embedded in the k-field, and so the linear relations (4.6) and (4.7) apply. When the crack has comparable size as the die thickness, the K-field goes beyond the k-field, and so the linear relations (4.6) and (4.7) break down. Meanwhile, the breakdown point in Figure 4-4 shows that the asymptotic stress field (4.1) is accurate within one fifth or one quarter of macroscopic length, similar to the solution of a finite crack in a homogeneous infinite sheet in the

classic linear elastic fracture mechanics.

4.4.4 Length dependent of local mode mixity and breakdown of power-law relation of *G~a*

It is well known that for such a structure that a thin film is bonded on substrate with interfacial crack [Figure 4-2], G=0 if a=0. When $0<a<h$, G depends on a; when $a>>h$, G attains steady state and so is independent of a. Therefore, the energy release rate should start from zero and increase monotonically to the steady-state value (Yu et al., 2001). However, from Figure 4-4, the energy release rate is far away from zero when $a/h=10^{-4}$. Even if we extend the plot to $a/h=10^{-7}$ that corresponds to a crack with atomic length, the energy release rate is still far from zero. The energy release rate G could go to zero unless we would let crack length a go to zero mathematically, but it is out of interest.

Eq.(4.8) also shows that the relation of G and a is not power-law since η is dependent of crack length a. And also the power $1-2\lambda_1 \approx 0$, so $(a/h)^{1-2\lambda_1} \to 1$ except $a=0$ exactly. Therefore, the curve of G~a can be wavy as shown in Figure 4-4(a) for the case of chip/LTCC package, and hardly goes to zero even if crack length a goes to atomically small.

4.5 Summary

The singular stress field around the edges and corners of flip-chip package arises due to the CTE mismatch of silicon die and packaging substrate. On package level, the

small features within the interconnects can be neglected. The cracks with same size and same orientation but on different interfaces should have similar energy release rates but different fracture toughness provided that the cracks are much smaller than the macroscopic length. We take delamination of chip-package interface as an example. We calculate the energy release rate of interface crack both from FEM and from asymptotic relations. The results show that the asymptotic relations agree with FEM data very well within a large range of crack length. From our results and others work, we can clearly see that the simplified model catch the essence without the complexity of 3D microstructure and diverse materials in the integrated circuits.

4.6 Appendix: Determination of coefficients by stretching and bending

We solve four boundary value problems sketched in Figure 4-5 and Figure 4-6, using the finite element code ABAQUS6.6. Let's consider two loading conditions for the flip-chip package: stretching and bending. Let P be the stretching force per unit thickness and M the bending moment per unit thickness. Plane strain conditions are assumed. The stress intensity factors of the bimaterial wedge of silicon chip on substrate, k_1 and k_2, are obtained by fitting Eq. (4.3) with the stresses calculated for problems in Figure 4-5, along $\theta = 0$ within $10^{-3} < r/h < 10^{-2}$. For the problems in Figure 4-6, the size of the interfacial crack a is set to be $0.01h$. The complex stress intensity factor of the interfacial crack, $K = K_I + iK_{II}$, is read out from the outputs of contour integrals. Using the linear relations (4.6) and (4.7), we obtain the coefficients c_{11}, c_{12}, c_{21} and c_{22} for both

chip/FR4 and chip/LTCC packages.

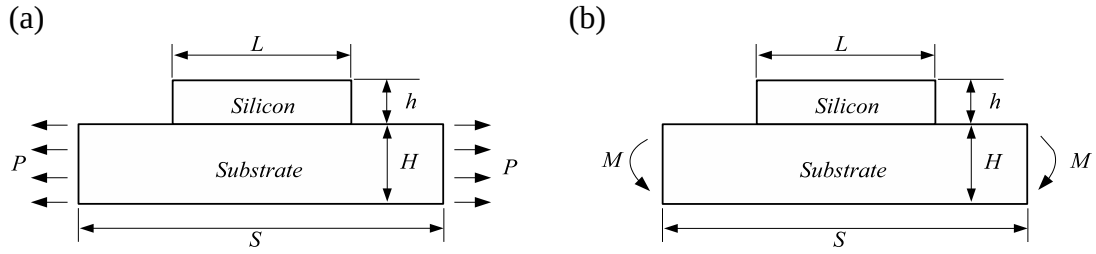

Figure 4-5: The flip-chip package *without crack* is under two loading conditions: stretching (a) and bending (b).

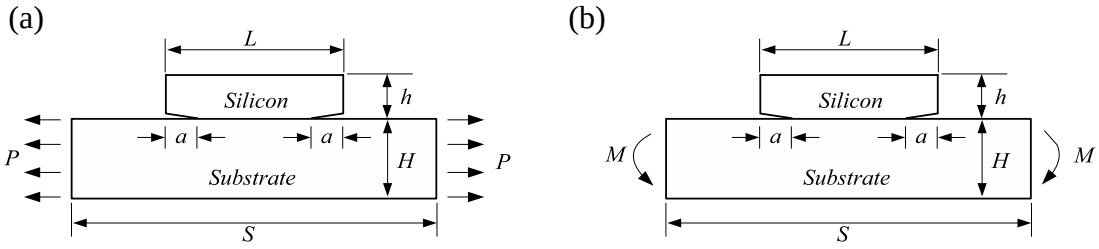

Figure 4-6: The flip-chip package *with interfacial crack* is under two loading conditions: stretching (a) and bending (b).

References:

1. Atluri, V.P., et al., “Critical aspects of high-performance microprocessor packaging”, *MRS Bulletin* **28**(1): 21-34, (2003).
2. Bogy, D. B., “Two edge-bonded elastic wedges of different materials and wedge angles under surface tractions”, *J. Appl. Mech*. **38**(6): 377-386, (1971).
3. Chen, L, Zhang, Q, Wang, G.Z., et al. “The effects of underfill and its material models on thermomechanical behaviors of a flip chip package”, *IEEE Transactions on Advanced Packaging* **24**(1): 17-24, (2001).
4. Dundurs, J., “Edge-bonded dissimilar orthogonal elastic wedges”, *J. Appl. Mech*., **36:** 650-652, (1969).
5. Dunn, M.L., Hui, C.Y., Labossiere P.E.W. and Lin Y.Y., “Small scale geometric and material features at geometric discontinuities and their role in fracture analysis”, *Int. J. Fract*. **110**: 101-121, (2001).
6. Fan X.J., Wang H.B., Lim T.B., “Investigation of the underfill delamination and cracking in flip-chip modules under temperature cyclic loading”, *IEEE Trans. Components Packaging Tech.* **24**(1): 84-91, (2001).
7. Feron, M., Zhang, Z., and Suo, Z., “Split singularities and dislocation injection in strained silicon”, *J. Appl. Phys.* (submitted). 2007.
8. Frear D.R. and Thomas S., “Emerging materials challenges in microelectronic packaging”, *MRS Bulletin* **28**(1): 68-74, (2003).

9. Gu Y, Nakamura T, Chen WT, et al. “Interfacial delamination near solder bumps and UBM in flip-chip packages”, *J. Electronic Packaging* **123**(3): 295-301, (2001).

10. Hirohata, K., et al., “Mechanical fatigue test method for chip/underfill delamination in flip-chip packages”, *IEEE Trans. Electronics Packaging Manuf.* **25**(3): 217-222, (2002).

11. Hui, C.Y. and Ruina, A., “Why *K* ? High order singularities and small scale yielding”, *Int. J. Fracture* **72**: 97-120, (1995).

12. Ieong, M., Doris, B., Kedzierski, J., Rim, K. and Yang, M., “Silicon device scaling to the sub-10-nm regime”, *Science* **306**: 2057, (2004).

13. Labossiere, P.E.W., Dunn, M.L., and Cunningham, S.J., “Application of bimaterial interface corner failure mechanics to silicon/glass anodic bonds”. *J. Mech. Phys. Solids* **50**: 405-433, (2002).

14. Liu, X.H., Lane, M.W., Shaw, T.M, and Simonyi, E., “Delamination in patterned films”, *Int. J. Solids Struct.* **44**(6): 1706-1718, (2007).

15. Liu, X.H., Suo, Z. and Ma, Q., “Split singularities: stress field near the edge of a silicon die on a polymer substrate”, *Acta Mater.* **47**(1): 67-76, (1999).

16. Mercado LL, Goldberg C, Kuo SM, et al., “Analysis of flip-chip packaging challenges on copper/low-k interconnects”, *IEEE Trans. Device & Mater. Reliability* **3**(4): 111-118, (2003).

17. Murarka S.P., “Multilevel interconnections for ULSI and GSI era”, *Materials Science & Engineering R-Reports* **19** (3-4): 87-151, 1997.

18. Pageau, S. S., Joseph, P. F., and Biggers, S. B. Jr., "The order of stress singularities for bonded and disbanded three-material junctions", *Int. J. Solids Struct*. **31**(21): 2979-2997, (1994).

19. Rice, J.R., "Elastic fracture mechanics concepts for interfacial cracks", *J. Appl. Mech*. **55**: 98, (1988).

20. Reuss R.H. and Chalamala B.R., "Microelectronics packaging and integration", *MRS Bulletin* **28**(1):11-15, (2003).

21. Rzepka S, Korhonen MA, Meusel E, et al., "The effect of underfill and underfill delamination on the thermal stress in flip-chip solder joints", *J. Electronic Packaging* **120** (4): 342-348, (1998).

22. Semmens, J.E. and Adams, T., "Flip chip package failure mechanism", *Solid State Technology* **41**(4): 59-64, (1998).

23. Suryanarayana D, Hsiao R, Gall TP, et al., "Enhancement of flip-chip fatigue life by encapsulation", *IEEE Trans. Components, Hybrids, & Manuf. Tech.* **14**(1): 218-223, (1991).

24. Tummala RR, Raj PM, Atmur S, et al., "Fundamental limits of organic packages and boards and the need for novel ceramic boards for next generation electronic packaging", *J. Electroceramics* **13**(1-3): 417-422, (2004).

25. Wang G., Merrill C., Zhao J.-H., et al. "Packaging effects on reliability of Cu/low-k interconnects", *IEEE Trans. Device Mater. Reliability* **3**(4): 119-128, (2003).

26. Williams, M.L., "Stress singularities resulting from various boundary conditions in angular corners of plates in extension", *J. Appl. Mech*. **19**(4): 526-528 (1952).

27. Yoon J., Zhang Z., Lu N., and Suo Z., "The effect of coating in increasing the critical size of islands on a compliant substrate", *Appl. Phys. Lett.* (accepted). 2007.

28. Yu, H.H., He M.Y., and Hutchinson J.W., "Edge effects in thin film delamination", *Acta Mater.* **49**: 93-107, 2001.

29. Zhai CJ, Sidharth, and Blish R, "Board level solder reliability versus ramp rate and dwell time during temperature cycling", *IEEE Trans. Device & Mater. Reliability* **3**(4): 207-212, (2003).

30. Zhai CJ, Sidharth, Blish RC, and Master R.N, "Investigation and minimization of underfill delamination in flip chip packages", *IEEE Trans. Device & Mater. Reliability* **4**(1): 86-91, (2004).

31. Zhang Q., et al., "On the degradation of the solder joints of underfilled flip chip packages: a case study", *Soldering & Surface Mount Tech.* **12**(3): 24-28, (2000).

32. Zhang Z., Yoon J., and Suo Z., "Method to analyze dislocation injection from sharp features in strained silicon structures", *Appl. Phys. Lett*. **89:** 261912 (2006).

33. Zhang Z., and Suo Z., "Split singularities and the competition between crack penetration and debond at a bimaterial interface", *Int. J. Solids Struct.* **44**(13), 4559-4573 (2007).

Chapter 5 Effect of Coating on Reliability of Stiff Islands on a Compliant Substrate

A flexible electronic system may consist of a polymeric substrate and an array of stiff islands, on which devices are fabricated. When the substrate is stretched, the devices on the islands experience small strains, but the islands may debond if they exceed a critical size. We show that a thin layer of polymer coating, covering the islands and the substrate, can markedly increase the critical island size.

5.1 Introduction

In one design of flexible electronics, illustrated in Figure 5-1, the substrate is a compliant polymer, while active devices are fabricated on thin-film islands of a stiff material (Hsu et al., 2004; Wagner et al., 2005; Bhattacharya et al, 2005). When the substrate is bent or stretched, the deformation is mostly accommodated by the substrate, and the strains in the islands are small. This design readily incorporates inorganic electronic materials into flexible electronics. It has been shown, however, when the

substrate is stretched by a certain amount, the islands may crack or debond when they are too large (Hsu et al., 2004; Bhattacharya et al, 2005; Lacour et al., 2006). The critical size of the islands depends on materials of the substrate and the islands (Yoon et al., 2007; Lu and Suo, 2007), and varies statistically. Experiments have shown that the critical island size markedly increases when a coating of a compliant material is applied to cover the islands and the substrate (Bhattacharya et al, 2005). For example, a 200 *nm* polymer coating enhances the survival rate of 120 μm indium-tin-oxide islands from 20% to 100%.

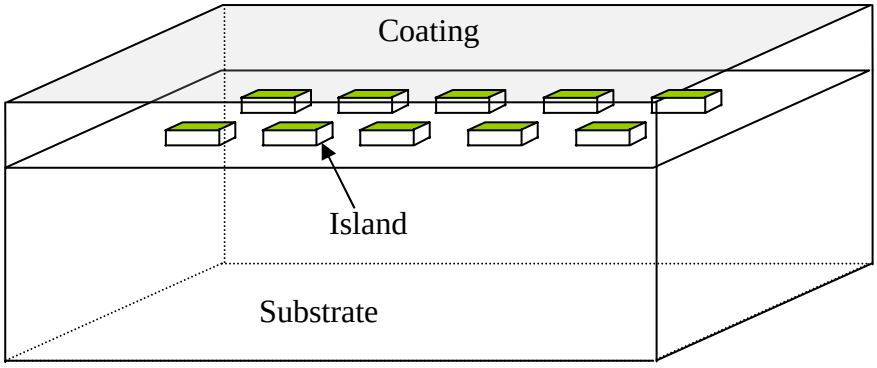

Figure 5-1: Schematic of an array of islands on a compliant substrate. A compliant coating is applied as a blanket film over the islands and substrate.

The object of this chapter is to study how a compliant coating improves the reliability of stiff islands on a complaint substrate. We first use the commercial finite element code, ABAQUS, to analyze the stress field near the edge of an island, with or without coating. When the edge is sharp and the island is bonded to the substrate, the stress field near the edge is singular (Bogy, 1971; Pageau et al., 1994). Our calculation

shows that a coating reduces the intensity of the stress field near the edge. This result, however, does not directly translate to a prediction of the critical island size. To do so, we prescribe a failure mechanism: debonding of the island from pre-existing flaws on the interface. We use the finite element code to compute the energy release rate of these flaws. We show that for a given fracture energy of the interface, the critical size of islands increases markedly when a coating is applied.

5.2 Decrease of stress intensity

Williams (1952) first studied the stress singularities of wedge corner in homogeneous isotropic materials, and many others, such as Bogy (1971) and Pageau et al (1994), extended this method to the wedge bonded by two dissimilar materials or the junction by three dissimilar materials.

Figure 5-2(a) depicts a wedge of the island bonded on the substrate, along with a system of polar coordinates (r,θ) centered at the root of the wedge. In this view, focused on the root of the wedge, the island takes the quarter space, $0^0 \le \theta \le 90^0$, and the substrate takes the half space, $-180^0 \le \theta \le 0^0$. The two materials are bonded along the interface, $\theta = 0^0$. Both materials are elastic and isotropic. Around the root of the wedge, when $r/h << 1$, the relation between the stress and the distance follows a power law

$$\sigma_{ij} \sim r^{-\lambda} \tag{5.1}$$

where λ is the singularity exponent. The larger the value of λ is, the more singular the stress field is. The exponent λ is determined by an eigenvalue problem, resulting in a transcendental equation (Bogy 1971). The exponent is commonly restricted as

$0 < \mathrm{Re}(\lambda) < 1$, with justifications critiqued by Hui and Ruina (1995) and Dunn et al (2001).

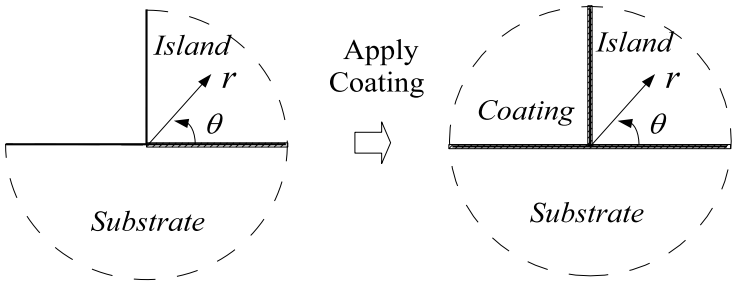

(a) (b)

Figure 5-2: (a) A bimaterial wedge. (b) A tri-material junction.

Physically the stress concentration around the wedge is due to the elastic mismatch and geometric discontinuity in this domain. There is an open space, equivalently a material with modulus zero. If we put a coating material to fill the open space, then the bimaterial wedge becomes a triple junction as shown in Figure 5-2(b). The singular stress field still takes the form of Eq.(5.1). And the singularity exponent λ can also be solved by the eigenvalue problem (Pageau et al 1994), but here λ becomes usually much smaller than the case of Figure 5-2(a).

As a demonstration, Figure 5-3 plots the singularity exponent λ as a function of the moduli ratio of the coating to the substrate E_c / E_s, with fixed Young's moduli of the stiff island and the compliant organic substrate, $E_f = 200$ GPa and $E_s = 5$ GPa, respectively. The Poisson's ratios of all materials are set to be 0.3. When $E_c = 0$, i.e.,

the case of bimaterial wedge, the singularity exponents are a pair of complex conjugates λ =0.483 ±0.0779*i*. The real part $\mathrm{Re}(\lambda)$ indicates the order of singularity, while the imaginary part $\mathrm{Im}(\lambda)$ indicates the oscillatory phenomena close to the wedge root, as in the case of interfacial crack (Connimu, 1977; Rice, 1988). When E_c increases, the order of singularity drops monotonically to the value of zero when $E_c = E_f$, in which case the concentrated stress field disappears since the triple junction becomes flat interface. If the coating becomes even stiffer than the island, the stresses concentrate again around the triple junction. The singularity exponent λ can be solved *quantitatively* for any material combination. The results obviously show that triple junction is usually of smaller singularity than bimaterial wedge. *Qualitatively,* this can be understood as follows: in triple junction structure Figure 5-2(b), the elastic mismatch is smaller than that in bimaterial wedge Figure 5-2(a), and also the geometric discontinuity is closed. This is why the coating can effectively enhance reliability.

Consider a periodic array of islands on a substrate shown in Figure 5-1. The period of the islands, *S*, sets the width of the unit cell in our calculation, as illustrated in the inset of Figure 5-4, with a single island, width *L* and thickness *h*. In the calculation, we set *S/L* = 1.5, set the thickness of the coating to be 2*h*, and set the thickness of the substrate to be 100*h*. All three materials are taken to be isotropic and linear elastic, with Young's modulus *E* and Poisson's ratio ν prescribed for each material, and subscripts *f, c* and *s* indicating the thin-film island, the coating and the substrate. Representative Young's moduli for islands and the substrate are $E_f = 200$ GPa and $E_s = 5$ GPa, respectively. In the calculation, we set $E_f / E_s = 40$, and set Poisson's ratios of all

materials to be 0.3. To study the effects of coating, we will vary E_c / E_s. In practice, the island may be of a square shape, but in our calculation, to illustrate the trend and avoid three-dimensional calculations, we assume that the unit cell undergoes plane strain deformation. The two edges of the substrates are prescribed with displacement $\pm \varepsilon_0 S / 2$, and the nominal stain ε_0 will be used to represent the applied load.

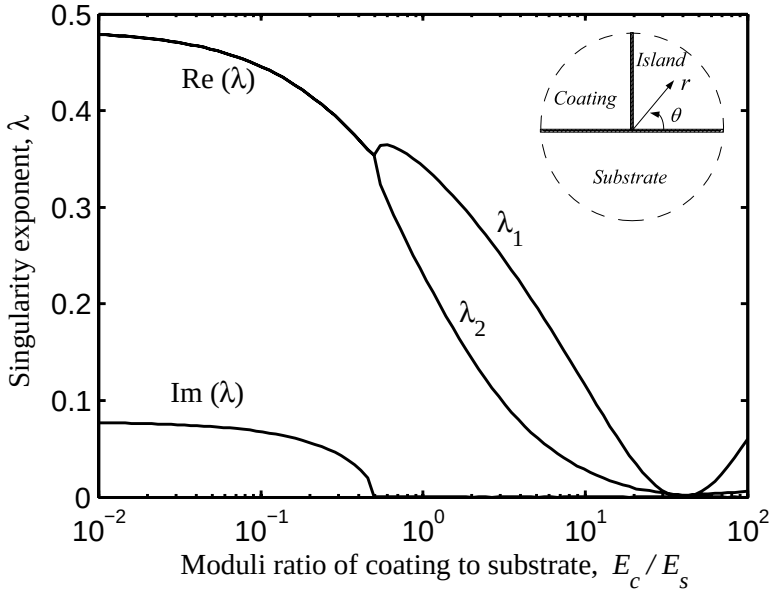

Figure 5-3: Singularity exponent, λ, is plotted as a function of E_c / E_s, the moduli ratio of coating to substrate with fixed moduli ratio of still island to compliant substrate $E_f / E_s = 40$. The Poisson's ratios of all materials are set to be 0.3.

Figure 5-4 plots the shear stress τ on the interface between the island and the substrate, distance r from the edge. The stress is normalized by $E_f^* \varepsilon_0$, where

$E_f^* = E_f / \left(1 - \nu_f^2\right)$ is the plane strain modulus of the island. The singularity analysis in Bogy (1971) and Pageau et al. (1994) determines the exponent λ, but does not determine the magnitude of the stress. For each value of E_c / E_s, our calculation shown in Figure 5-4 gives the exponent as the slope in the plot. Comparing the three cases, E_c / E_s = 0 (without coating), E_c / E_s = 0.2 and E_c / E_s = 1 (with a coating), we note that even the compliant coating not only reduces the exponent λ, but also reduces the magnitude of the stress, which is explicitly justified by Figure 5-4.

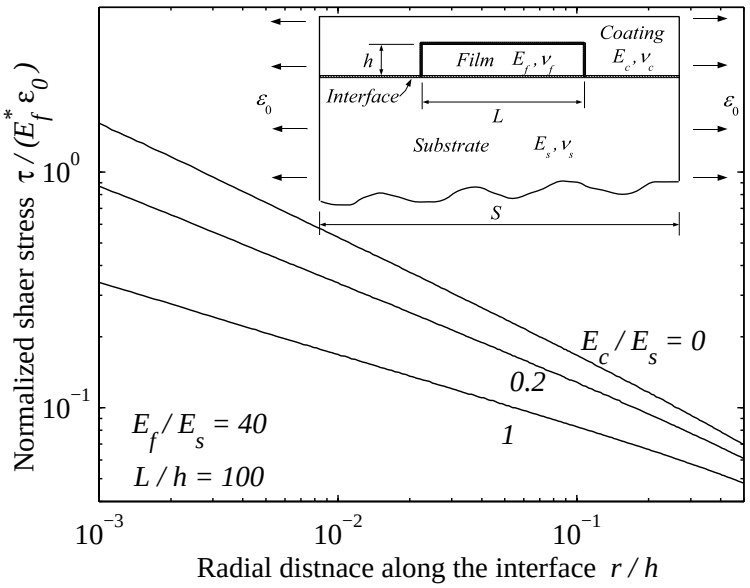

Figure 5-4: The inset shows a unit cell used in calculation. Shear stress along the interface is plotted as a function of the distance from the left edge of the island. The shear stress decreases as the modulus of the coating increases.

Note that when the singularity exponents are close to zero, the nonsingular terms make the great contribution to the whole stress field, so a complete power-law series needs to be adopted (Rice, 1988). Then the asymptotic singular solution is not easy to use any more. However, the finite element analysis supplies the numerical solution anyway.

In practice, there are other materials and features are integrated on the substrate. But the feature sizes are much smaller than the island thickness. Hence, regardless of the details, the coating always reduces stress intensity.

5.3 Increase of critical size of islands

While the above section shows that the coating reduces the intensity of the stress near the edge, the result does not lend itself to a prediction of the critical island size. To do so, we specify a failure mechanism by introducing interfacial flaws at the edges. Figure 5-5 illustrates flaws, length *a,* placed on the interface near the edges of the island. A dimensional analysis shows that the energy release rate of the interfacial crack takes the following form:

$$G = E_f^* \varepsilon_0^2 h \cdot F\left(\frac{a}{h}, \frac{L}{h}, \frac{E_c}{E_s}\right). \tag{5.2}$$

where $F\left(a/h, L/h, E_c/E_s\right)$ is a dimensionless function. Note that we have already specified a number of other dimensionless ratios, as discussed in the previous paragraphs.

The energy release rate is calculated using ABAQUS. Figure 5-5 plots the normalized energy release rate as a function of E_c/E_s, with a fixed flaw size $a = 0.1h$

and a fixed island size L = 100h. The energy release rate decreases markedly in the presence of the coating. When the modulus of the coating equals that of the island, $E_c = E_f$ (or $E_c / E_s = 40$), the coating and the island become an elastically homogeneous blanket film. In this case, the interface is free of shear and normal stresses, so that the energy release rate vanishes. On the other hand, when the coating is as stiff as the island, the strain in the middle of island will be the same as the nominal strain ε_0, so that the island will be prone to cracking. Consequently, one should select a coating compliant enough to ensure low strains inside the island, but stiff enough to alleviate the stress intensity at the edges.

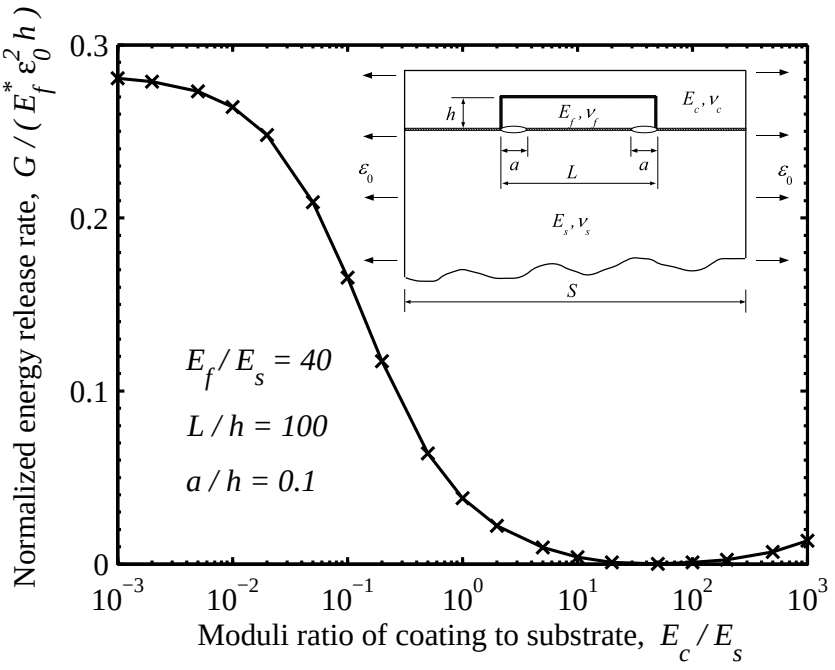

Figure 5-5: The normalized energy release rate of a flaw is plotted as a function of the normalized modulus of the coating. The inset shows a unit cell used in the calculation. Flaws are added on the interface near the edges.

Figure 5-6(a) plots the normalized energy release rate as a function of the normalized flaw size a/h. Three cases are considered, one without coating $E_c/E_s = 0$, the other two with compliant coatings $E_c/E_s = 0.2$ and $E_c/E_s = 1$. For example, when $a/h = 0.01$, the energy release rate reduces by 80% for $E_c/E_s = 0.2$, and reduces by 96% for $E_c/E_s = 1$. The reduction is still significant even when $a/h = 1$. For a small crack $a/h << 1$, on the basis of an asymptotic analysis, we expect that $G \propto a^{1-2\lambda}$. This scaling law is evident from the plots in Figure 5-6(a). Of course, we are aware that this power law relation is not strict if we consider the dependence of local mode mixity on crack length, as we discussed in Chapter 4.

In practice, the size and the location of a flaw are statistical. The variation of the energy release rate with the flaw size may partially account for statistical variations of the critical island size observed in experiments.

The mode angle ψ is defined such that $\tan\psi$ is the ratio of the shear stress to the normal stress on the interface at a small distance ahead the tip of the interfacial crack. Figure 5-6(b) plots the mode angle as a function of normalized crack size a/h for $E_c/E_s = 0$, 0.2 and 1. All three curves show that the shearing mode dominates.

Figure 5-7 plots the normalized energy release rate as a function of the normalized island size, *L/h*. The flaw will grow and cause debonding when the energy release rate *G* reaches the fracture energy of the interface, Γ. The condition $G = \Gamma$ would correspond to a horizontal line in Figure 5-7, and the intersections of the line with the curves in Figure 5-7 would predict the critical island size. Thus, Figure 5-7 shows the effect of the coating in increasing the critical island size. For example, taking

representative values, $E_f^* = 200\text{GPa}$, $h = 1\mu\text{m}$, $\varepsilon_0 = 2\%$, and $\Gamma = 10\text{J/m}^2$, we obtain that $\Gamma/\left(E_f^*\varepsilon_0^2 h\right) = 0.125$. Drawing this value as a horizontal line in Figure 5-7, we note that the critical island size is about $24\,\mu\text{m}$ in the absence of coating, and is about $90\,\mu\text{m}$ with a coating of $E_c / E_s = 0.2$.

(a)

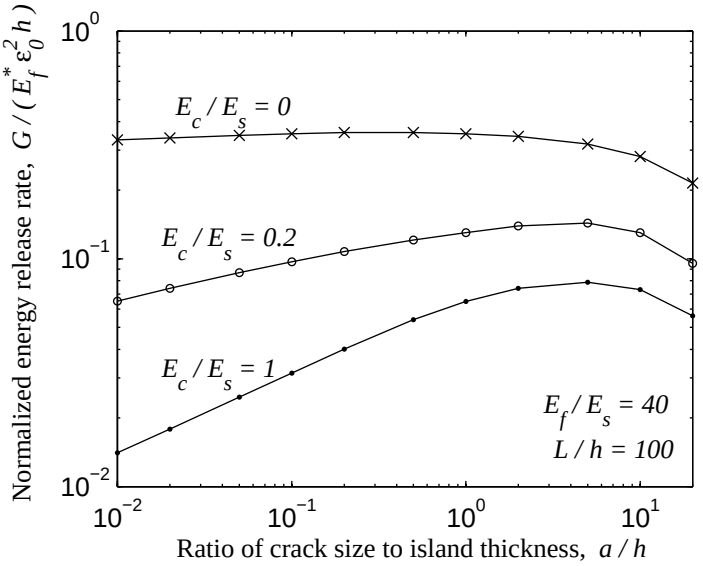

(b)

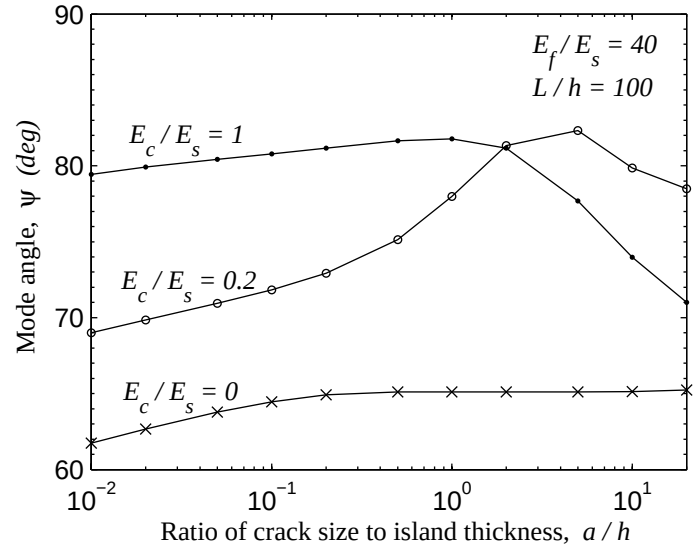

Figure 5-6:(a) Normalized energy release rate is plotted as a function of normalized crack size. (b) Mode angle ψ is plotted as a function of normalized crack size.

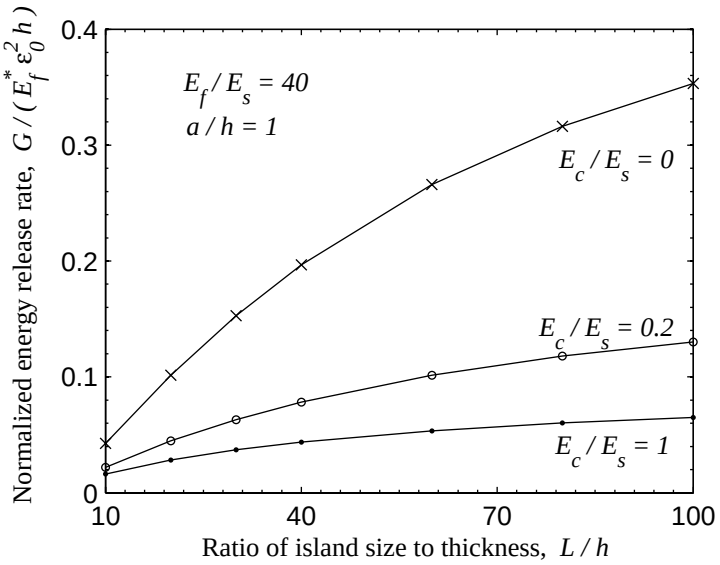

Figure 5-7: The normalized energy release rate is plotted as a function of the normalized island size.

The suppression of debonding by coating can be understood as follows. If there is no coating, the traction-free surface of an edge is easy to move to accommodate the deformation, so that the interfacial flaw can readily cause the island to slide relative to the substrate. However, if a coating is applied, the displacement of the edge is constrained, so that the crack is more difficult to propagate.

In the above discussion, we have chosen a specific failure mechanism: debonding between the island and the substrate. The stress concentration at the edge of the island can cause other mechanisms of failure, such as debonding between the coating and the island, and damage of the substrate. By reducing the stress intensity near the edge, the coating is expected to mitigate these other mechanisms as well. Quantitative analyses of these other mechanisms are beyond the scope of this chapter.

5.4 Summary

In summary, we have shown the effects of compliant coating in two ways. First, the coating reduces the intensity of stresses near the island edges by reducing the elastic mismatch. Second, the coating suppresses the delamination by constraining the sliding of dissimilar materials around the edge. Even though we study the effect of coating for flexible electronics, we expect that the coating enhance the reliability of other microelectronic devices, such as flip-chip packages.

References:

1. P. I. Hsu, M. Huang, Z. Xi, S. Wagner, Z. Suo, and J.C. Sturm, "Spherical deformation of compliant substrates with semiconductor device islands", *J. Appl. Phys.,* **95**, 705 (2004)
2. S. Wagner, S. P. Lacour, J. Jones, P. I. Hsu, J. C. Sturm, T. Li, and Z. Suo, Electronic skin: architecture and components", *Physica E*, **25**, 326 (2005)
3. R. Bhattacharya, S. Wagner, Y. J. Tung, J.R. Esler, and M. Hack, "Organic LED Pixel Array on a Dome." *Proc. IEEE*, **93**, 1273 (2005)
4. S. P. Lacour, S. Wagner, R. J. Narayan, T. Li, and Z. Suo, "Stiff subcircuit islands of diamond-like carbon for stretchable electronics", *J. Appl. Phys.*, **100**, 011905 (2006)
5. J. Yoon, T. Li, and Z. Suo, "Critical size of stiff islands on stretchable substrates" Unpublished work.
6. N. Lu, J. Yoon and Z. Suo, "Delamination of stiff islands patterned on stretchable substrates", *Int. J. Mat. Res.*, 2007 (in press).
7. M.L. Williams, "Stress singularities resulting from various boundary conditions in angular corners of plates in extension." *J. Appl. Mech.* **19**(4), 526-528 (1952).
8. D. B. Bogy, "Two edge-bonded elastic wedges of different materials and wedge angles under surface traction." *J. Appl. Mech.* **38**, 377-386 (1971).
9. S. S. Pageau, P. F. Joseph, and S. B. Biggers, Jr., "The order of stress singularities for bonded and disbanded three-material junctions." *Int. J. Solids Struct.* **31**(21), 2979-2997 (1994).

Chapter 6 Saturated Voids in Interconnect Lines due to Thermal Strains and Electromigration

Thermal strains and electromigration can cause voids to grow in conductor lines on semiconductor chips. This long-standing failure mode is exacerbated by the recent introduction of low-permittivity dielectrics. We describe a method to calculate the volume of a saturated void (VSV), attained in a steady state when each point in a conductor line is in a state of hydrostatic pressure, and the gradient of the pressure along the conductor line balances the electron wind. We show that the VSV will either increase or decrease when the coefficient of thermal expansion of the dielectric increases, and will increase when the elastic modulus of the dielectric decreases. The VSV will also increase when porous dielectrics and ultrathin liners are used. At operation conditions, both thermal strains and electromigration make significant contributions to the VSV. We discuss these results in the context of interconnect design.

6.1 Introduction

Silicon dioxide has long been used on semiconductor chips as an interlevel dielectric. To enhance the performance of the chips, the industry has been introducing new dielectrics with low permittivity (Morgen et al., 1999; Martin et al., 2000; Maex et al., 2003; Hussein and He, 2005). The rapid introduction of materials calls for effective methods to select materials and ensure reliability. This chapter focuses on the impact of the new dielectrics on a long-standing failure mode: the formation of voids in the conductor lines caused by thermal strains and electromigration.

Figure 6-1 sketches a representative life of a Cu line, encapsulated by a TaN liner, a SiN cap and an interlevel dielectric, fabricated on a silicon substrate. These materials have dissimilar coefficients of thermal expansion (CTEs). When the structure is cooled from the processing temperature, a stress field arises in the conductor line, motivating Cu atoms to diffuse and voids to form (Gleixner et al., 1997; Ogawa et al., 2002; Harada et al., 2003; Besser and Zhai, 2004). When an electric current is applied in the conductor, the electron wind also motivates Cu atoms to diffuse (Blech, 1976; Korhonen et al., 1993; Rosenberg et al., 2000). The combined action of thermal strains and electromigration leads to a complex dynamics of the voids: they nucleate, disappear, drift, change shape, break up, and coalesce (Arzt et al., 1994; Lee et al., 2002; Leon et al., 2004).

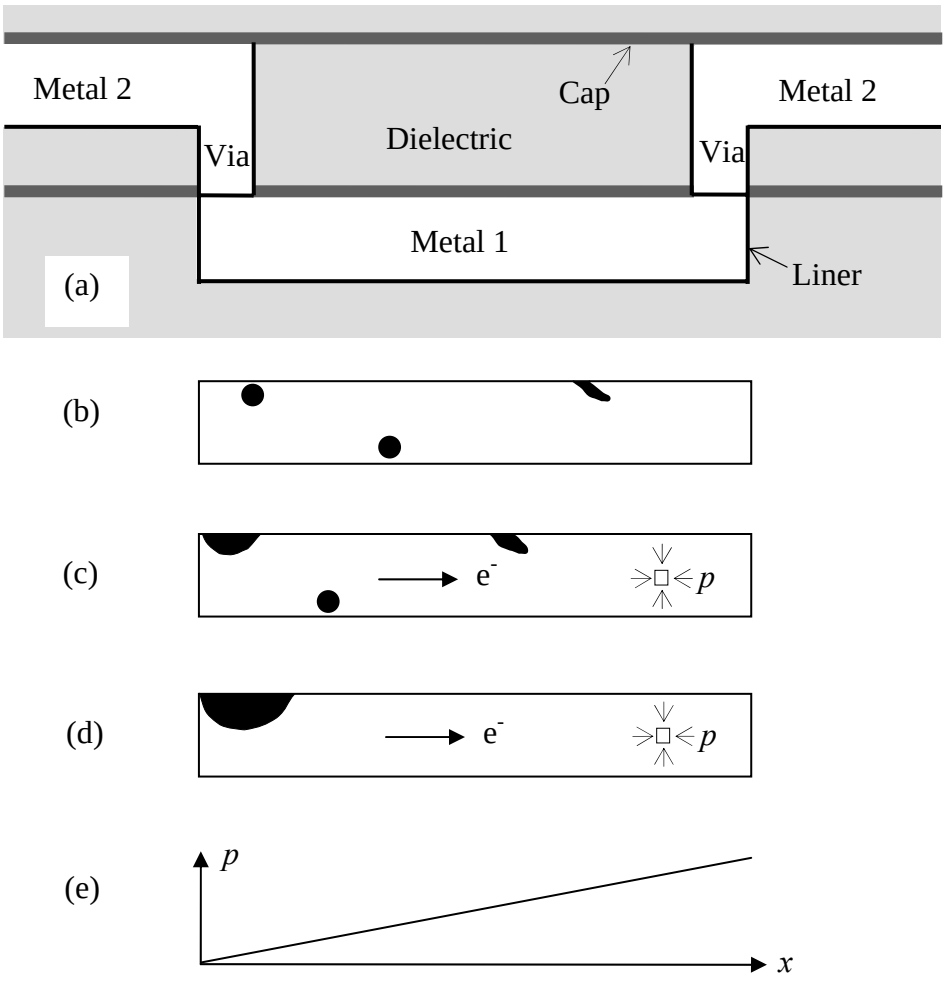

Figure 6-1:(a) Schematic of a M1-V1-M2 structure. (b) Stresses arise upon cooling from the processing temperature and are relaxed by the formation of the voids. (c) Subject to an electric current, atoms diffuse in the direction of electron flow. Voids grow upstream and pressure builds up downstream. (d) When the pressure gradient balances the electron wind force, a single void is left near the upstream via, and net atomic diffusion stops. (e) In the steady state, the pressure distributes linearly in the conductor line.

The complex dynamics of the voids is lively to watch, but difficult to translate

into an engineering decision. The conductor line, however, may reach a *steady state*, a well-defined state that can be used in interconnect design. As Cu atoms diffuse in the direction of electron flow, the voids grow upstream, and pressure rises downstream. During this process, the encapsulation prevents Cu atoms from diffusing out of the conductor line. Eventually, when the steady state is reached, a single void remains near the upstream via and the pressure gradient in the conductor line balances the electron wind: the net drift of Cu atoms stops, and the void saturates. If the volume of the saturated void (VSV) is too small to block the electric current, the conductor line is immortal (Filippi et al., 1996; Suo, 1998; Hau-Riege and Thompson, 2000; Hau-Riege, 2002, Filippi et al., 2002; Suo, 2003). Consequently, the VSV can be used to rank materials and geometries of interconnect structures. A reliable method to determine the VSV will help to ensure the reliability of interconnect structures today, and to design those in the future.

Up to now the VSV due to thermal strains has only been considered in rudimentary terms. When a structure is cooled from a reference temperature T_0 to a temperature T, the VSV is proportional to the temperature drop and the conductor volume:

$$V_{sv}^{TH} = 3\alpha(T_0 - T)AL\,. \tag{6.1}$$

where A is the cross-sectional area and L the length of the conductor line. The coefficient α, which we will call the effective mismatch in the CTEs, depends on not only the CTEs of the materials in the structure, but also their elastic moduli, as well as the aspect ratio of the conductor line and other geometric parameters. Table 6-1 gives representative properties of the materials, including three choices of interlevel dielectrics: SiO_2, carbon-doped oxide (CDO), and SiLK. Although the use of the SiLK is limited, this material is

included here to illustrate the effects of a dielectric with a large CTE (Strittmater et al., 2003; Dalton et al. 2003). When SiO_2 is used, all the materials surrounding the conductor have similar CTEs as silicon, so that the VSV scales with the difference in the CTE of copper and silicon: $\alpha = \alpha_{Cu} - \alpha_{Si} = 14\text{ppm/K}$. When a dielectric with a large CTE is used, however, will the VSV increase or decrease, and by how much? Such questions cannot be answered by the rudimentary consideration. Section 6.2 will describe a general method to calculate the VSV due to thermal strains.

Table 6-1: Materials properties used in calculation.

Materials	E (GPa)	ν	α (10^{-6} K^{-1})
Cu	138	0.33	17
TaN	200	0.3	6
SiN	275	0.24	4
Si	165	0.22	3
SiO_2	71	0.17	3
CDO	10	0.3*	12
SiLK	3	0.3*	50

* Poisson's ratios of the CDO and the SiLK are unavailable to us, and are assigned to be 0.3 in our calculations.

By comparison, the VSV due to electromigration has been examined closely. When the conductor line is subject to an electric current, the VSV due to electromigration

takes the form (Filippi et al., 1996)

$$V_{sv}^{EM} = \frac{Z^* e \rho j L^2 A}{2\Omega B}. \tag{6.2}$$

where Z^* is the effective valence, e the elementary charge, ρ the resistivity, j the current density, and Ω the volume per atom in the conductor line. The factor B is an effective modulus of the structure. In an analytical estimate of B, a conductor line is modeled as a cylinder of a circular cross section, embedded in an infinite homogenous matrix (Korhonen et al., 1993). This model gives $B^{-1} = B_{Cu}^{-1} + G^{-1}$, where B_{Cu} is the bulk modulus of copper, and G is the shear modulus of the matrix (Suo, 2003). As shown in Table 6-1, the new dielectrics have lower elastic moduli than SiO_2. The more compliant a dielectric is, the more Cu atoms need to move downstream to build up the pressure gradient to balance the electron wind, and the larger the VSV will be. In a realistic interconnect structure, the materials surrounding the conductor have dissimilar elastic moduli. This effect is accounted for in a finite element model, assuming that the interconnect structure is an elastic composite and the conductor line undergoes a transformation strain (Hau-Riege and Thompson, 2000).

It is difficult to justify the assumption that the conductor remains elastic when metal atoms can diffuse over the entire length of the conductor line. Recent experimental data have shown that the diffusivity of Cu atoms on grain boundaries in the conductor is larger than that on the interface between the conductor and the cap (Gan et al., 2004). The grain boundaries and the interface will allow Cu atoms to redistribute by diffusion, a process that will stop only when deviatoric stresses in the conductor vanish. Consequently, when the void saturates, the stresses at every point in the conductor reach

a state of hydrostatic pressure. On the basis of this picture, Section 6.3 will describe a method to calculate the VSV due to electromigration.

We study the impact of the new dielectrics, as well as the effects of the width of the Cu lines, the thickness of the liners, and the spacing between the neighboring Cu lines. Section 6.4 will study the impact on the VSV due to the use of porous dielectrics and ultrathin liners. Section 6.5 will place the results into the context of interconnect design.

6.2 Saturated void due to thermal strains

As a computational model, Figure 6-2 illustrates a cross section of a conductor line of Metal 1 surrounded by other materials. The structure is replicated periodically in the horizontal direction to represent an array of parallel conductor lines. The coordinate x is along the conductor line, and z is normal to the substrate surface. In the current technology, the typical thickness of a conductor line is h = 150-250nm. Above the structure in Figure 6-2 are several other levels of conductor lines. The actual thickness of the dielectric between levels, h_1, is about h, but we set $h_1 = 2h$ to account for the constraint due to materials above the conductor. Similarly, to account for the constraint due to the silicon substrate, we set its thickness to be $50h$. Also fixed are the thicknesses of the SiN cap ($h_2 = 0.25h$), the dielectric beneath the conductor ($h_3 = h$), and the SiO_2 buffer layer ($h_4 = h$). We will vary the width of the conductor line w, the pitch between the neighboring conductor lines s, and the thickness of the liner t.

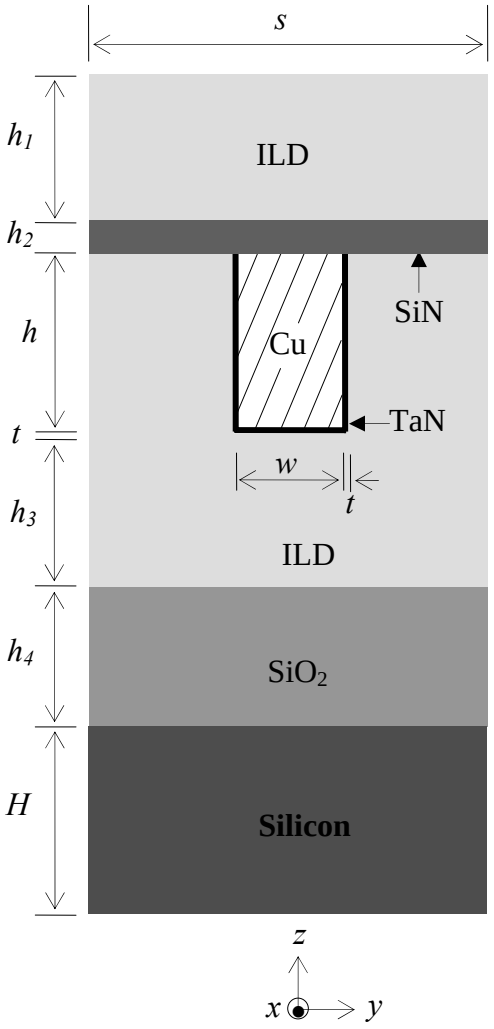

Figure 6-2: The cross section of a Cu line, surrounded by a TaN liner, a SiN cap, and an interlevel dielectric (ILD).

We first consider the VSV due to thermal strains, in the absence of electric current. In this case, when the voids saturate, the stress in the copper line vanishes. Consequently, we take the Cu line out of its surrounding structure, leaving the latter with a hole (Figure 6-3). On cooling the stress-free Cu line changes its volume by

$$\Delta V_{Cu}^{TH} = -3\alpha_{Cu}(T_0 - T)AL\,. \tag{6.3}$$

If all the surrounding materials had the same CTE as silicon, the volume of the hole would change by $-3\alpha_{Si}(T_0 - T)AL$. In reality, however, these materials have different CTEs, giving rise to an extra change in the volume of the hole. We write this extra change in the volume of the hole as $-3\beta(T_0 - T)AL$, an equation that defines the quantity β. The net change in the volume of the hole is

$$\Delta V_{hole}^{TH} = -3(\alpha_{Si} + \beta)(T_0 - T)AL\,. \tag{6.4}$$

The difference between the two changes, Equations (6.3) and (6.4), gives the VSV due to thermal strains: $V_{sv}^{TH} = \Delta V_{hole}^{TH} - \Delta V_{Cu}^{TH} = 3\alpha(T_0 - T)AL$, with

$$\alpha = \alpha_{Cu} - \alpha_{Si} - \beta = 14\text{ppm/K} - \beta\,. \tag{6.5}$$

The effective mismatch in the CTEs, α, scales the VSV due to thermal strains. In our sign convention, when the hole *shrinks* by an extra volume, $\beta > 0$, which decreases the VSV.

To calculate β, we focus on the structure surrounding the hole (Figure 6-3). Upon cooling, this structure develops a stress field in itself, which is governed by a three-dimensional thermoelastic boundary value problem. This problem is reduced to a two-dimensional one on the basis of the following considerations. The extra change in the volume of the hole is calculated by replacing the CTE α_i of each material in the structure with $\alpha_i - \alpha_{Si}$. With this replacement, the silicon substrate undergoes no thermal strain and constrains the structure, and the strain in the *x*-direction in the structure vanishes. Also vanishing are the displacements in the *y*-direction at the lines of symmetry. The top surface is traction-free. These considerations define a plane strain thermoelastic problem,

which we solve using the commercial finite element code ABAQUS. We then calculate the extra change in the volume of the hole using an integral along the boundary of the hole, $L\int u_n ds$, where u_n is the displacement normal to the surface of the hole, positive when pointing outwards of the hole. By definition, β is calculated from

$$-3\beta(T_0 - T)AL = L\int u_n ds\,. \tag{6.6}$$

Since u_n is linear in the temperature drop $T_0 - T$, the calculated β is independent of the temperature drop.

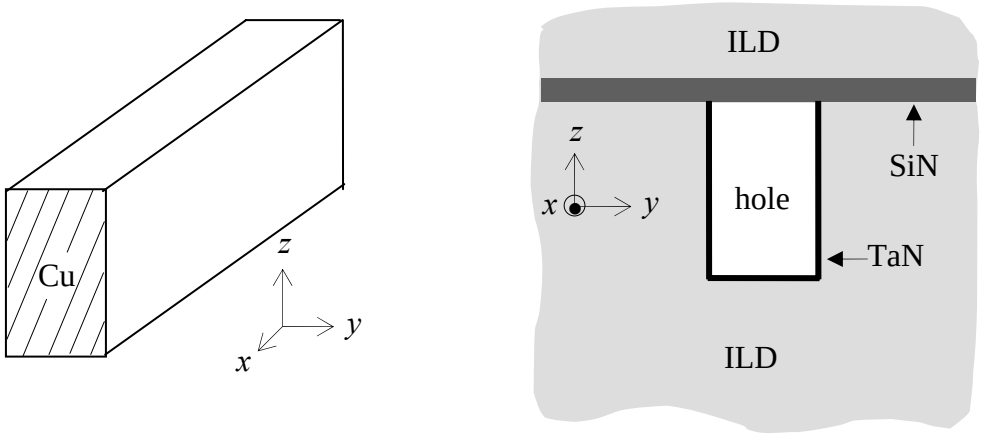

Figure 6-3: The copper line is taken out of the surrounding structure, leaving a hole in the latter.

Figure 6-4(a) shows the calculated α as a function of the aspect ratio h/w of the conductor line for the three choices of interlevel dielectrics. When the SiO_2 is used as the interlevel dielectric, the extra change in the volume of the hole is negligible: $\beta \approx 0$ and

$\alpha \approx 14\,\text{ppm/K}$. When the CDO is used, its CTE is large but its elastic modulus is much lower than that of silicon, so that α only deviates slightly from 14 ppm/K. When the SiLK is used, however, its CTE is so large that α varies significantly: $\alpha > 14\,\text{ppm/K}$ for narrow lines, and $\alpha < 14\,\text{ppm/K}$ for wide lines. For all cases calculated, α is positive; that is, on cooling the copper line shrinks more than the hole, even though the SiLK has a much larger CTE than copper.

These surprising results for the SiLK are understood as follows. Figure 6-5 shows an undeformed mesh at the reference temperature, and a deformed mesh at the lower temperature. In the calculation, the CTE of the silicon substrate is set to be zero. The substrate constrains the structure, so that the horizontal displacements vanish at the two lines of symmetry. When the structure is cooled, the dielectric on the side of the hole contracts in both vertical and horizontal directions. The vertical contraction moves the top and the bottom surface of the hole toward each other, decreasing the volume of the hole. By contrast, the horizontal contraction draws the side surface of the hole outward, increasing the volume of the hole. For a wide conductor line, the vertical contraction prevails, and the saturated void decreases, $\alpha < 14\,\text{ppm/K}$. For a narrow conductor line, the horizontal contraction prevails, and the saturated void increases, $\alpha > 14\,\text{ppm/K}$.

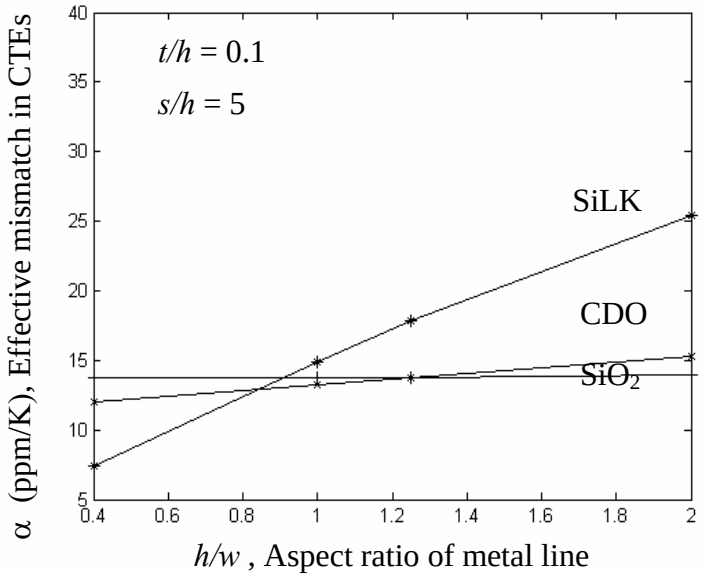

Figure 6-4(a): The effective mismatch in CTE as a function of the aspect ratio of the copper line.

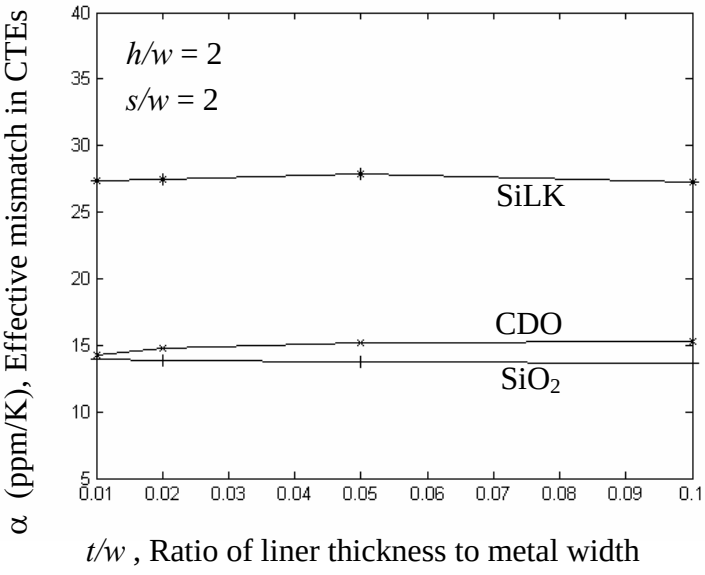

Figure 6-4(b): The effective mismatch in CTE as a function of the thickness of the liner.

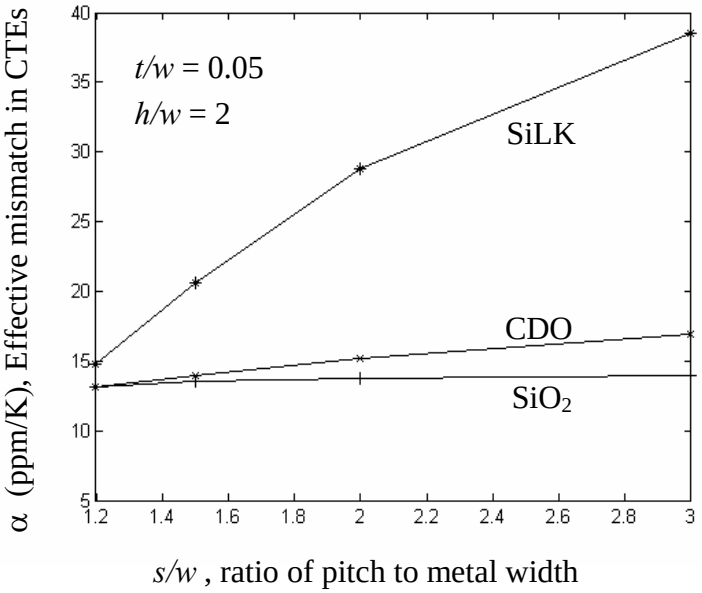

Figure 6-4(c): The effective mismatch in CTE as a function of the aspect ratio of the pitch between the neighboring copper lines.

When the conductor line is very wide, or when the TaN liner and the dielectric between the neighboring conductor lines are thin, the side surface of the hole moves negligibly, and the top and bottom surfaces move to shrink the hole, so that $\beta = (\alpha_{ILD} - \alpha_{Si})/3$, where α_{ILD} is the CTE of the interlevel dielectric. This maximum value of β is 3 ppm/K for the CDO and is 15.7 ppm/K for the SiLK. Regardless the geometry of the structure, the effective mismatch α will be positive if the maximum value $\beta = (\alpha_{ILD} - \alpha_{Si})/3$ is less than $\alpha_{\mathrm{Cu}} - \alpha_{\mathrm{Si}} = 14\,\mathrm{ppm/K}$, namely, if $\alpha_{ILD} < 45\,\mathrm{ppm/K}$.

Figure 6-4(b) shows that α weakly depends on the liner thickness. Figure 6-4(c) shows that α increases with the pitch between the neighboring conductor lines, a trend that can also be understood in a similar way as above.

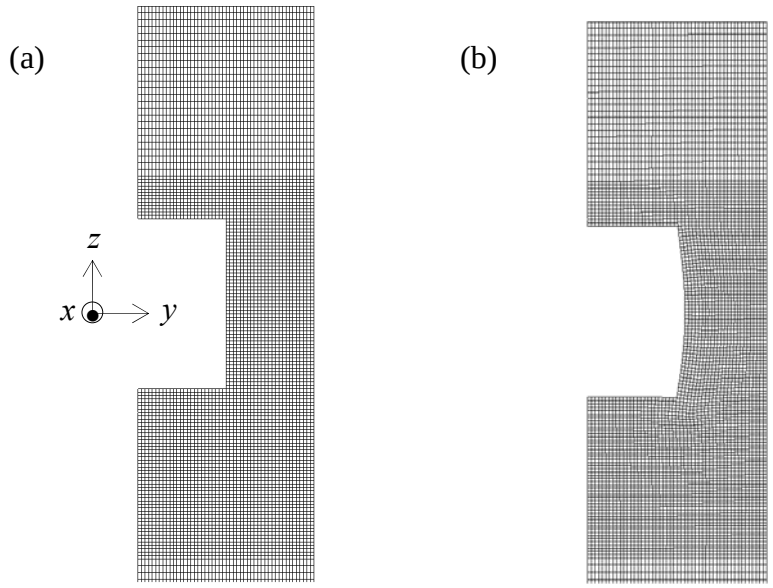

Figure 6-5:(a) Undeformed mesh at the reference temperature. (b) Deformed mesh at a lower temperature. The displacement field is amplified by a factor of 10 for visional clarity.

6.3 Saturated void due to electromigration

We next calculate the VSV due to electromigration, in the absence of thermal strains. When a Cu line is subject to an electric current, the momentum exchange between conduction electrons and Cu atoms results in an electron wind force, $F = Z^* e\rho j$, motivating Cu atoms to diffuse in the direction of the electron flow. As a void grows upstream, pressure rises downstream. When the gradient of the pressure balances the electron wind force, net atomic drift stops and the void saturates. In this steady state, the pressure in the conductor line vanishes at the upstream via ($x = 0$), where the void forms, and builds up linearly toward the downstream via, $p = Fx/\Omega$ (Blech, 1976).

Once again, we take the Cu line out of its surrounding structure, leaving the latter

with a hole. In the steady state, the Cu line is subject to the linear distribution of pressure, and changes its volume by $\Delta V_{Cu}^{EM} = -A\int_0^L (p/B_{Cu})dx$, or

$$\Delta V_{Cu}^{EM} = -\frac{FL^2 A}{2\Omega B_{Cu}}. \tag{6.7}$$

Subject to the linear distribution of pressure, the hole enlarges its volume, which we write in a similar form:

$$\Delta V_{hole}^{EM} = \frac{FL^2 A}{2\Omega\mu}. \tag{6.8}$$

This equation defines an effective modulus of the surrounding structure, μ. The difference between the two changes, Equations (6.7) and (6.8), gives the VSV due to electromigration: $V_{sv}^{EM} = \Delta V_{hole} - \Delta V_{Cu} = \left(Z^* e\rho j L^2 A\right)/\left(2\Omega B\right)$, with

$$\frac{1}{B} = \frac{1}{B_{Cu}} + \frac{1}{\mu}. \tag{6.9}$$

The quantity $1/B$ is an effective compliance of the interconnect structure, and scales the VSV due to electromigration.

Single crystalline copper has a cubic crystal structure, with elastic moduli $C_{11} = 168\text{GPa}$, $C_{12} = 121\text{GPa}$ and $C_{44} = 75\text{GPa}$. When a polycrystalline copper line is subject to a hydrostatic stress, the strains are identical in all directions and all grains. Consequently, the bulk modulus B_{Cu} of the polycrystal is the same as that of the single crystal, given by $B_{Cu} = \left(C_{11} + 2C_{12}\right)/3 = 136\text{GPa}$.

To calculate the effective modulus of the surrounding structure, μ, we prescribe on the surface of the hole the linear pressure distribution, $p = Fx/\Omega$. As illustrated in Figure 6-6(a), this is a three-dimensional elastic boundary value problem. When the

length of the conductor line is much larger than its height and width, the pressure varies slowly along the length of the hole. Consequently, the three-dimensional structure can be approximated by many slices, each subject to a uniform pressure on the surface of the hole, deforming under the plane strain conditions [Figure 6-6(b)]. We solve the plane strain elastic boundary value problem using the finite element code ABAQUS. By definition, μ is calculated from

$$Ap/\mu = \int u_n ds \,. \tag{6.10}$$

Since the displacement u_n in this case is linear in the pressure, the calculated μ is independent of the pressure.

Figure 6-7(a) shows the calculated B as a function of the aspect ratio of the copper line for the three choices of interlevel dielectrics. The results are similar to those calculated using the models of transformation strains (Hau-Riege and Thompson, 2000). In all cases, B is much below the bulk modulus of copper (136 GPa), suggesting that $\mu << B_{Cu}$ and $B \approx \mu$. It is mainly the surrounding materials, rather than the copper line itself, that accommodate the Cu atoms relocated to the downstream. Of the three interlevel dielectrics, the SiO_2 is the least compliant, the CDO the intermediately compliant, and the SiLK the most compliant. For each dielectric, B reaches maximum at $h/w \approx 1.25$. This trend is understood as follows. In the analytical model of a conductor line of elliptic cross section embedded in an infinite homogeneous matrix, the effective modulus maximizes when the cross section of the conductor is circular (Korhonen et al., 1993). However, in a realistic interconnect structure, a somewhat larger *h/w* makes the structure stiffest, because the silicon substrate is stiffer than the dielectric and constrains the lateral deformation.

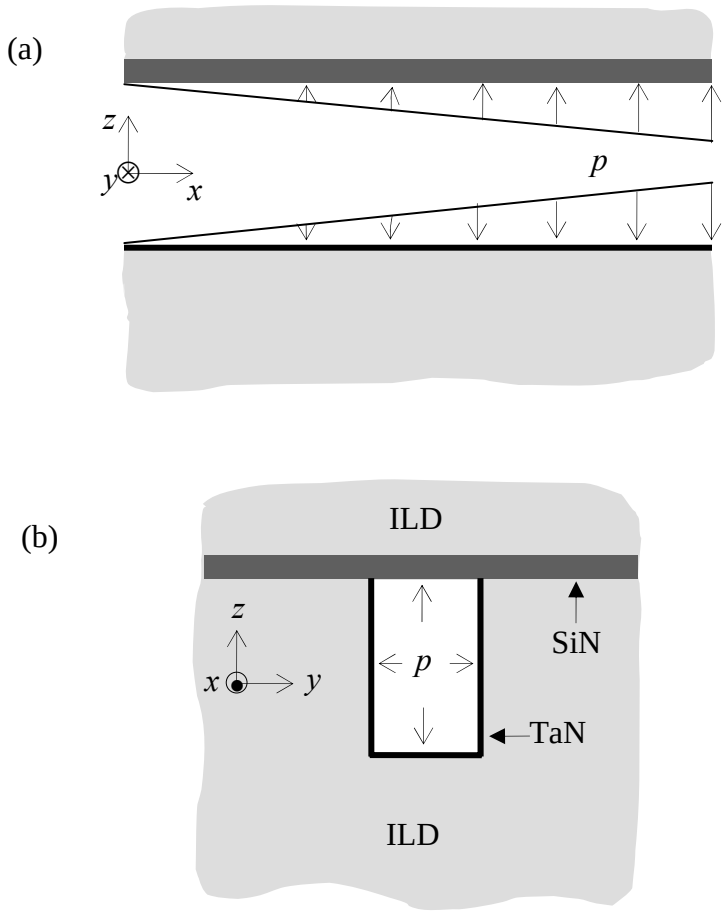

Figure 6-6:(a) Pressure distribution along the hole. (b) A cross section of the structure surrounding the hole.

Figure 6-7(b) shows B as a function of the liner thickness. As shown in Table 6-1, the TaN liner is a stiff material, so that B increases with the liner thickness. As remarked above, $\mu << B_{Cu}$ and $B \approx \mu$. An estimate is given by (Suo, 2003)

$$B \approx G_{ILD} + G_{liner} \cdot t / w. \tag{6.11}$$

where G_{ILD} and G_{liner} are the shear moduli of the two materials. This analytical solution is obtained for a conductor line of a circular cross section, which is a good approximation

when the cross section is a square. For the results shown in Figure 6-7(b), where $h/w = 2$, the slopes are somewhat different from G_{liner}.

Figure 6-7(c) shows B as a function of the pitch between the neighboring conductor lines. For the SiLK and the CDO, the smaller the pitch, the stiffer the structure. For the SiO_2, however, B is not a monotonic function of the pitch. These trends can also be explained by the moves of various surfaces of the hole. Recall that the horizontal displacement vanishes at the vertical line of symmetry. The effect of this constraint is more pronounced when the neighboring lines are closer. On the other hand, the top surface is traction-free. When the hole is subject to the pressure, the less the material on the side of the hole, the more readily the top and the bottom surface move apart. These two effects compete to determine B, and give rise to the various trends in Figure 6-7(c). When the pitch becomes very large, the effective modulus approaches an asymptote.

(a)

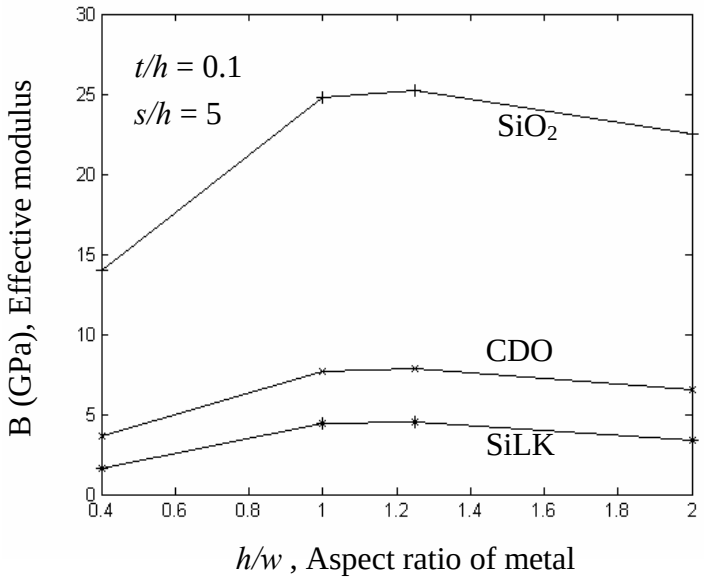

Figure 6-7(a):The effective modulus B of the aspect ratio of the copper line.

(b)

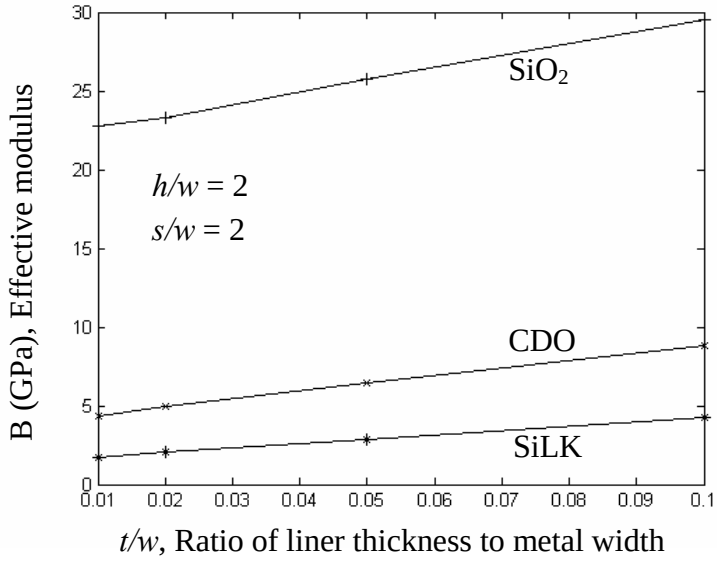

Figure 6-7(b): The effective modulus B of the thickness of the liner.

(c)

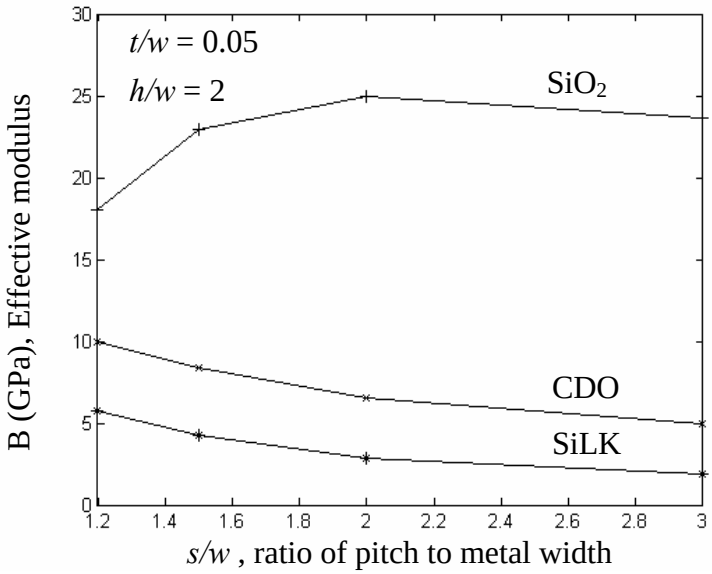

Figure 6-7(c): The effective modulus B of the pitch between the neighboring copper lines.

6.4 Effects of porous dielectrics and ultrathin liners

Two trends are anticipated for the interconnect structures of the coming generations. First, to increase the speed of the chips, the industry will introduce lower-permittivity dielectrics, mostly likely porous dielectrics. Second, to further miniaturize, the thickness of the liners, as well as all other features, will reduce. This section examines the effects of porous dielectrics and ultrathin liners on the VSV. We will use CDOs with an increasing amount of porosity as an example. When the porosity of the CDO increases, the elastic modulus decreases, but the CTE is nearly a constant (Grill, 2003). In our calculations, we vary the modulus from 1 to 16 GPa and keeps the CTE to be 12 ppm/K.

Figure 6-8 shows the calculated α and B as functions of the modulus of the dielectric for several values of the liner thickness. The effective mismatch in the CTEs, α, deviates slightly from $\alpha_{Cu} - \alpha_{Si} = 14\,\text{ppm/K}$, as expected from the discussion in Section 6.2. Consequently, the use of the porous CDOs and the ultrathin liners has little effect on the VSV due to thermal strains. By contrast, the porous CDOs and the ultrathin liners have a significant impact on the effective modulus B. For example, for representative values $t/w = 0.08$ and $E = 10\text{GPa}$ in the current technology, B = 7.7 GPa. For a thinner liner and more compliant dielectric, $t/w = 0.04$ and $E = 3\text{GPa}$, the effective modulus reduces to B = 2.5 GPa, leading to a VSV three times larger.

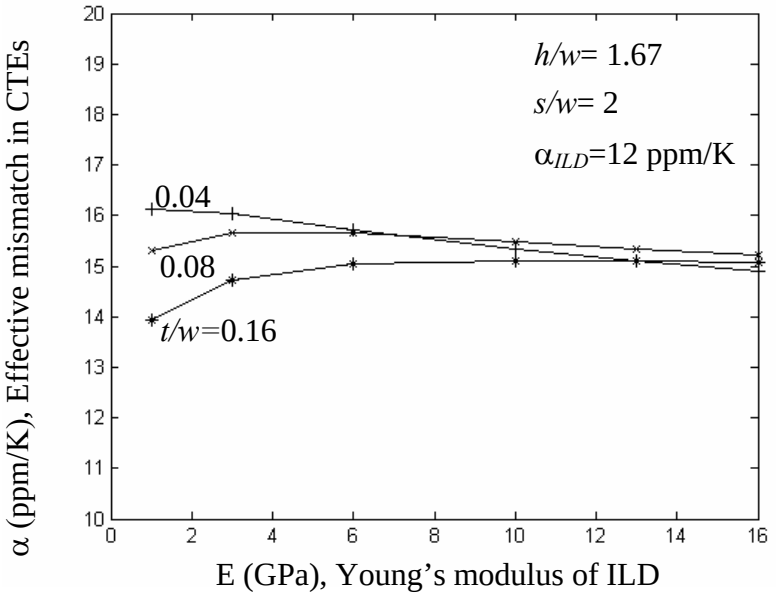

Figure 6-8(a):The effect of elastic modulus of the dielectric and the thickness of the liner on the effective mismatch in the CTEs.

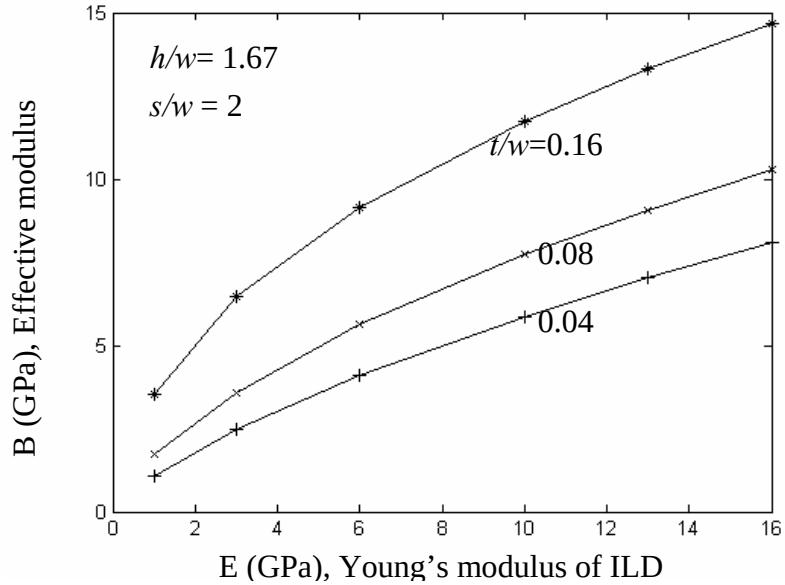

Figure 6-8(b):The effect of elastic modulus of the dielectric and the thickness of the liner on the effective modulus.

6.5 Discussions

In this section, we place the above results into the context of interconnect design. Unless otherwise stated, we will use the following values in numerical estimates: $Z^* = 1$, $\rho = 4\times10^{-8}\,\Omega\text{m}$, $\Omega = 1.18\times10^{-29}\,\text{m}^3$, $j = 10^{10}\,\text{A/m}^2$, $w = 10^{-7}$ m, $h = 2\times10^{-7}\,\text{m}$, $L = 10^{-5}\,\text{m}$, $T_0 - T = 200^0\text{C}$, $\alpha = 15$ ppm/K, and $B = 7.7\text{GPa}$.

Thus far we have focused on one kind of the steady state, in which a single void forms near the upstream via, and the electron wind is balanced by the pressure gradient $\partial p/\partial x = Z^* e\rho j/\Omega$. An alternative steady state is that no void forms, and the electron wind is balanced by the same pressure gradient. In this void-free steady state, the stress at the upstream via no longer vanishes. The pressure gradient induces a tensile stress $Z^* e\rho jL/2\Omega$ near the upstream via, and a compressive stress of the same magnitude near the downstream via. In addition, the temperature change causes a uniform hydrostatic tensile stress $3B\alpha(T_0 - T)$ in the conductor. The sum of the two effects gives the net stress at the upstream via:

$$\sigma = 3B\alpha(T_0 - T) + \frac{Z^* e\rho jL}{2\Omega}. \tag{6.12}$$

Thermal stresses in encapsulated narrow Cu lines have been measured using X-ray diffraction, and calculated using the finite element method assuming the conductor line is elastic (e.g., Rhee et al., 2003). The mean of the stresses so obtained agrees well with thermal stress in Equation (6.12).

Using the values listed in the beginning of this section, we find from Equation (6.12) that the stress due to thermal strains is 69 MPa, and that due to electromigration is

27 MPa. Let γ be the surface energy; for copper its value is on the order of 1 J/m^2. A void-like flaw in the conductor will grow if its initial size exceeds about γ/σ, which is on the order of 10 nm. Flaws of this size are likely to be present in the conductor lines. Also, right after the cooling, the stresses in the conductor can be very high at grain junctions. These high stresses are not described by the steady state formula (6.12), but can motivate voids to nucleate in the conductor. Consequently, the void-free steady state is unlikely to be stable in practice, and will not be discussed any further in this chapter.

The net VSV in a conductor line is the sum of the contributions from thermal strains, electromigration, and any other origins:

$$V_{sv} = V_0 + 3\alpha(T_0 - T)AL + \frac{Z^* e\rho j L^2 A}{2\Omega B}. \tag{6.13}$$

where V_0 is the contribution from all other origins. It is sometimes assumed that the conductor line is stress-free and void-free at the encapsulation temperature. Under this assumption, $V_0 = 0$ if the encapsulation temperature is set to be the reference temperature T_0. In practice, however, this assumption is unreliable. As-deposited copper lines contain a large number of defects such as grain boundaries. During annealing and even after encapsulation, the defects are gradually removed, a process that generates stresses in the conductor line. Furthermore, encapsulation may introduce other defects that add to the void volume. On the basis of these considerations, a prudent approach is to set the reference temperature T_0 at an arbitrary level, and determine V_0 by an independent measurement. Alternatively, the temperature at which a conductor line is stress-free and void-free should be determined independently.

Voids induced by thermal strains and electromigration are usually tested

separately, under different conditions. This practice may lead to misleading predictions. For example, a representative stress-free, void-free temperature is 300^0C. At this temperature, when an electric current is applied, the VSV is solely due to electromigration, and is estimated to be $0.7\times10^{-21}\mathrm{m}^3$, using the numbers listed at the beginning of this section. However, at an operation temperature, say 100^0C, the VSV due to the temperature drop is $1.8\times10^{-21}\mathrm{m}^3$. Here the thermal strains contribute significantly to the VSV. Consequently, subject to the same electric current, a conductor line found immortal at an elevated temperature can be mortal at the operation temperature.

A void in a conductor line becomes critical when it blocks the electric current. The volume of the critical void is a random variable depending on, among other factors, the exact location where the void forms. The smallest current-blocking void usually forms right at the upstream via. The volume of this critical void can be estimated as follows. Copper atoms are mobile on the void surface. The void shape depends on the relative magnitude of the electron flux and the surface energy, measured by the dimensionless number (Suo et al., 1994)

$$\eta = \frac{Z^* e \rho j a^2}{\gamma\Omega}. \tag{6.14}$$

where a is a representative size scale of the void. For representative void size $a = 100\mathrm{nm}$, the dimensionless number is on the order $\eta = 10^{-1}$. Consequently, the void shape is largely determined by the surface energy. Furthermore, we will neglect the anisotropy in the surface energy, and assume that the surface diffusion is fast compared to the transport along the line. The critical void takes the equilibrium shape of a spherical cap, its base diameter coinciding with the via size d, giving the volume

$$V_{\text{crit}} = \frac{\pi d^3}{12}\left(\frac{1}{1-\cos\Psi} + \frac{\cos\Psi}{2}\right)\sin\Psi\,. \tag{6.15}$$

where Ψ is the wetting angle of copper on the liner. The critical volume scales with the via diameter as $V_{\text{crit}} \sim d^3$, and increases as the wetting angle decreases. Taking $\Psi = 90^\circ$ and $d = 10^{-7}$ m, we find that $V_{\text{crit}} = 0.26\times10^{-21}\,\text{m}^3$.

When the volume of the saturated void is smaller than the volume of the critical void, $V_{sv} < V_{\text{crit}}$, the conductor line is immortal (Filippi et al., 1996; Suo, 1998; Hau-Riege and Thompson, 2000; Hau-Riege, 2002; Filippi et al., 2002; Suo, 2003). The above numerical estimates, however, show that the VSV exceeds the V_{crit}, indicating that the conductor line is mortal. This prediction is consistent with the reported experimental data (e.g., He et al., 2004; Hau-Riege et al., 2004). One remedy to immortalize a conductor line is to increase V_{crit} by introducing, for example, multiple vias, or a large via, or an effective shunt. It is also possible to reduce the VSV by changing geometry. As evident in Equation (6.13), the VSV due to electromigration is quadratic in the line length, and the VSV due to temperature change is linear in the line length. If the length of the line is reduced to $L = 0.5\times10^{-5}\,\text{m}$, for example, the VSV due to electromigration is $0.18\times10^{-21}\,\text{m}^3$, and the VSV due to a temperature drop of 200°C is $0.9\times10^{-21}\,\text{m}^3$. To further reduce the latter, one may explore processing conditions that lower the stress-free and void-free temperature of the conductor line. In a given interconnect structure, conductor lines may have different geometric parameters. Their effects on the VSV are contained in the numerical results presented in this chapter. For example, for compliant dielectrics, the more closely spaced the neighboring conductor lines, and larger the effective modulus *B*, and the smaller the VSV [Figure 6-7(c)]. As another example,

upper level conductor lines in an interconnect structure are typically wide. Such wide lines have small effective modulus B [Figure 6-7(a)].

When the volume of the saturated void exceeds the volume of the critical void, $V_{sv} > V_{\text{crit}}$, the conductor line is mortal. A design rule for mortal lines must ensure that the lifetime is long enough. Time-dependent models, invoking void nucleation and growth, have been discussed in Andleigh et al. (1999), He et al. (2004), and Hau-Riege et al. (2004). Further discussions of such models are beyond the scope of this chapter.

6.6 Summary

Voids caused by thermal strains and electromigration are a major concern in the semiconductor industry. In a conductor line a void may saturate to a deterministic volume, the VSV, a well-defined quantity that can be used to rank materials and geometries of the interconnect structures. We describe a general method to calculate the VSV, assuming that the steady state is reached when each point in a conductor line is in a hydrostatic state. The method circumvents the complexity caused by the transient processes of atomic migration and void dynamics. Numerical results show that the VSV can either increase or decrease when the coefficient of thermal expansion of the dielectric increases, and will increase when the elastic modulus of the dielectric decreases. The use of porous dielectrics and ultrathin liners will significantly increase the VSV. Thermal strains contribute significantly to the VSV, and must be taken into account in interpreting electromigration tests. Subject to a given electric current, a conductor line found

immortal at an elevated temperature can be mortal at the operation temperature. The method to determine the VSV provides a tool to assess options in interconnect design.

References:

1. M. A. Hussein and J. He, IEEE Trans. Semi. Manufacturing 18, 69 (2005).
2. M. Morgen, E.T. Ryan, J.-H. Zhao, C. Hu, T. Cho, P.S. Ho, JOM, September, 37-40 (1999).
3. S.J. Martin , J.P. Godschalx, M.E. Mills, E.O. Shaffer, P.H., Townsend, Advanced Materials, 12, 1769 (2000).
4. K. Maex, M.R. Baklanov, D. Shamiryan, F. Iacopi, B.H. Brongersma, Z.S. Yanoviskaya, J. Appl. Phys. 93, 8793 (2003).
5. R.J. Gleixner, B.M. Clemens, and W.D. Nix, J. Mater. Res. 12, 2081 (1997).
6. E. T. Ogawa, J. W. McPherson, J. A. Rosal, K. J. Dickerson, T. - C. Chiu, L. Y. Tsung, M. K. Jain, T. D. Bonifield, J. C. Ondrusek, and W. R. McKee. Proceedings of 2002 IEEE International Reliability Physics Symposium. pp.312-321.
7. M. Hommel, A.H. Fischer, A. v. Glasow, A.E. Zitzelsberger, in Stress-Induced Phenomena in Metallization: 6th International Workshop, edited by S.P. Baker, M.A. Korhonen, E. Arzt, P.S. Ho, (AIP, 2001), pp. 157-168.
8. T. Harada, K. Kobayashi, M. Takashi, K. Nii, A. Ikeda, T. Ueda, and T. Yabu, in Proc. IEEE Int. Interconnect Technology Conference, 2003, pp. 92-94.
9. P. R. Besser, and C. J. Zhai, in Stress-Induced Phenomena in Metallization: 7th International workshop, edited by P.S. Ho, S.P. Baker, T. Nakamura, and C.A. Volkert (AIP, Austin, 2004), pp. 207-216.
10. I.A. Blech, J. Appl. Phys. 47, 1203 (1976).

11. M. A. Korhonen, P. Børgesen, K.N. Tu, and Che-Yu Li, J. Appl. Phys. 73, 3790 (1993).

12. R. Rosenberg, D.C. Edelstein, C.-K. Hu, K.P. Rodbell, Annu. Rev. Mater. 30, 229 (2000).

13. S.-H. Lee, J. C. Bravman, J. C. Doan, S. Lee, P. A. Flinn, and T. N. Marieb, J. Appl. Phys. 91, 3653 (2002).

14. R. Leon, J.A. Colon, K.C. Evans, D.T. Vu, V. Blaschke, B. Bavarian, E.T. Ogawa and P.S. Ho, J. Mater. Res. 19, 3135 (2004).

15. E. Arzt, O. Kraft, W.D. Nix, and J.E. Sanchez, J. Appl. Phys., 76, 1563 (1994).

16. R.G. Filippi, R.A. Wachnik, H. Aochi, J.R. Lloyd, M.A. Korhonen, Appl. Phys. Lett. 69, 2350 (1996).

17. Z. Suo, Acta Mater. 46, 3725 (1998).

18. S. P. Hau-Riege and C. V. Thompson, J. Mater. Res. 15, 1797 (2000).

19. S. P. Hau-Riege, J. Appl. Phys. 91, 2014 (2002).

20. R.G. Filippi, R.A. Wachnik, C.-P. Eng, D. Chidambarrao, P.C. Wang, J.F. White, M.A. Korhonen, T.M. Shaw, R. Rosenberg, and T.D. Sullivan, J. Appl. Phys. 91, 5787 (2002).

21. Z. Suo, in Comprehensive Structural Integrity, edited by W. Gerberich and W. Yang (Elsevier, Amsterdam, 2003), Vol. 8, pp. 265-324.

22. R.J. Strittmatter et al., Mater. Res. Soc. Symp. Proc. 766, 265-272 (2003).

23. T.J. Dalton et al., Proceedings of Advanced Metallization Conference 2003, edited by G.W. Ray, T. Smy, T. Ohla and M. Tsujimura, Warrendale, PA, USA: Mater. Res. Soc, 2004. pp. 85-89.

24. D. Gan, R. Huang, P.S. Ho, J. Leu, J. Maiz, and T. Scherban, in Stress-Induced Phenomena in Metallization: 7th International workshop, edited by P.S. Ho, S.P. Baker, T. Nakamura, and C.A. Volkert (AIP, Austin, 2004), pp. 256-267.

25. A. Grill, J. Appl. Phys. 93, 1785 (2003).

26. S.-H. Rhee, Y. Du, P.S. Ho, J. Appl. Phys. 93, 3926 (2003).

27. Z. Suo, W. Wang, and M. Yang, Appl. Phys. Lett. 64, 1944 (1994).

28. J. He, Z. Suo, T. N. Marieb, and J. A. Maiz, Appl. Phys. Lett. 85, 4639 (2004).

29. C.S. Hau-Riege, S.P. Hau-Riege, A.P. Marathe, J. Appl. Phys. 96, 5792 (2004).

30. V.K. Andleigh, V.T. Srikar Y.J. Park, C.V. Thompson, J. Appl. Phys. 86, 6737 (1999).

Chapter 7 Concluding Remarks

The microelectronic devices integrate more and more diverse materials in a complicated three-dimensional structure with feature size from nanometers to meters. The performance leaps of these devices are so attractive; meanwhile the reliability issues become more urgent in semiconductor industry.

In this dissertation, we explored some key issues in the thermal-mechanical reliability of microelectronic devices. We have developed a framework to study the stress singularities with unequal exponents for broad applications, such as crack penetration and deflection, dislocation injection into strained silicon, chip-package interaction, and suppression of island-substrate debonding, etc. We also developed a method to calculate the volume of saturated voids in conductor lines due to thermal strains and electromigration. The major findings of the dissertation are listed as follow:

(1). The singular stress field around the sharp features, such as crack, wedge, corner, etc., is a linear superposition of two singular modes, one stronger and the other weaker. So long as the process zone size is small compared with the macroscopic length, there exists a *k*-annulus where the asymptotic singular stress field applies. In the past, the contribution from the weaker singularity had not been appreciated, sometimes were

neglected without careful consideration. In this dissertation, we prudently consider its significance, and characterize the proportion of the two modes by a dimensionless parameter: local mode mixity (or mode angle). In the case of a crack impinging upon a bimaterial interface, the weaker singularity may readily affect whether the crack will penetrate across, or debond, the interface. In the case of a dislocation emitting from the sharp edge of strained silicon structures, the weaker singularity is negligible when the film is compliant, but is significant when the film is stiff.

(2). In the study of dislocation emission in strained silicon, we describe a procedure to select the critical slip systems for the full range of the mode angle; give a scaling relation between the residual stress level and feature sizes; predict the correct orders of magnitude of the critical stress; and compare the analysis with experimental observations. Our approach can be easily applied to other crystallographic orientations, different material combinations, and various shapes of sharp features. The approach may ultimately contribute to the design of strained silicon devices.

(3). We extend the framework of split singularities and local mode mixity to investigate the interfacial delamination due to chip-packaging interaction. We simplify the structure to be silicon/substrate with 90^0 wedge configuration, and neglect the small local features of integrated circuits. We calculate the energy release rate and the mode angle of crack on the chip-package interface based on the asymptotic linear elastic stress field. The asymptotic solution agrees with finite element calculation very well for the crack length varying several orders of magnitude. In addition, we find that the relation of energy release rate G and crack length a is not power-law since local mode mixity η is dependent of crack length a. Therefore, the curve of G~a can be wavy and hardly goes to

zero even if crack length *a* goes to atomically small. The local mode mixity plays an important role in crack behavior.

(4). A remedy to reduce the singularity and to suppress the debonding in flexible electronics is proposed—applying coating. We show that a thin layer of polymer coating, covering the islands and the substrate, can markedly increase the critical island size.

(5). Voids caused by thermal strains and electromigration are another major concern in the semiconductor industry. In a conductor line a void may saturate to a deterministic volume, the VSV, a well-defined quantity that can be used to rank materials and geometries of the interconnect structures. We describe a general method to calculate the VSV, assuming that the steady state is reached when each point in a conductor line is in a hydrostatic state. The method circumvents the complexity caused by the transient processes of atomic migration and void dynamics.

The use of porous dielectrics with low modulus and ultra-thin liners are the technology trends. Nevertheless, numerical results show that the VSV will significantly increase when the elastic modulus of the dielectric decreases and the diffusion barrier becomes thinner. Therefore, the voiding failure mode continues to be a major problem.

In addition, the great contribution to VSV from thermal strains should draw attention. In electromigration tests, a conductor line found immortal at an elevated temperature can be mortal at the operation temperature. The approach and results provide a tool to assess options in interconnect design.

After having finished the above work, we think more detailed considerations and/or lots of other related work can be done. In the following, we envision some urgent

reliability issues that are the extension of the study in this dissertation.

(1). Strained silicon-on-insulator (sSOI) is the future of semiconductor industry. The large strain, e.g. 1.4% to 2.5%, is introduced in silicon layer to enhance the device performance. In the device, the triple junction is a very common geometric feature, such as shallow trench isolation (STI), gate-sSOI-cap junction, etc. The dislocations are easily emitted from the corner, or the concentrated stress derives the dislocation to move under the transistor channel. Some researchers did the experiments to measure and/or FEM to calculate the singular stress field around the triple junctions or contact corners, but there is no good model for the stress field analysis or useful formula to approximate the near-junction stress field, and there is no good parameter defined to assess critical conditions. The study of stress singularities supplies a possibility with careful consideration of higher-order singularities and non-singular terms.

(2). In our model, we considered a straight dislocation nucleates along the film edge under the assumption of plain strain condition, which deserved careful consideration. Before a dislocation nucleates, the stress field is generated due to SiN stripe, so it is plain strain problem. However, once it nucleates, this assumption needs to be checked carefully. First, once the dislocation nucleates, it must be a half loop with the two ends pinned on the film edge. It is hardly to be straight. Second, the 60^0 mixed dislocation has screw part which can not be modeled as plane strain problem any more since the dislocation itself generates a stress field which is not plane strain. So, the final stress state is the superposition of the two fields. If we study the propagation of the 60^0 mixed dislocation, we have to consider the three-dimensional elastic field.

In addition, the dislocation propagates into the silicon to some depth, and then

threads along the edge of film. The threading depth should be finite since the driving force—the resolved shear stress—decreases. And the threading process has similarities with channel cracking in the thin films, so it can be studied the same way as propagation of channel crack.

(3). In practice, SiN square pads are used rather than the long stripes. In order to avert the complexity of 3D corner singularities, we use a long stripe in our study. But, the 3D corner is more critical than 2D edge and therefore deserves attention. Dunn et al. (JMPS, 2001) had an asymptotic solution for the perfectly 3D corner. Here, we propose a 2D approximate solution for the 3D corner based on the following arguments. Since in practice, the 3D corner is formed by the perpendicular edges of pads on the substrate, and usually rounded with a radius much larger than atomic scale, e.g., 40 nm rounded radius for a 500 nm thick SiN pad in Kammler et al. (APL, 2005). The local stress state close to the root of 3D bimaterial interface is still in plain strain state. Hence, the singular stress expression in the dissertation still applies, except that the stress intensity factors need to be modified to include the effects of the stress overlapping from two adjacent edges. Then, the remaining complexity just arises from the 3D FEM calculation.

(4). As we know, if a dislocation is present under the source/drain channel of a transistor, it leads to electrical leakage, and fail the device. Because the dislocation is so detrimental to transistors that we want to avert any dislocation under transistor channel in the final product. But, there are many steps in the whole process to fabricate a transistor on strained silicon, such as silicidation, ion implantation in source and drain area, shallow trench isolation, except the SiN capping. Any step can induce dislocations. In Chapter 3, we just considered one processing step. The assurance of reliability in one step cannot

assure no dislocation in the final product. The reliability of the final product deserves more attention and work. For example, if dislocations are nucleated inevitably, it is essential to understand the mechanism of dislocation motion under the operation conditions in the final product. Only if the dislocation does not move into the source/drain channel, the transistor functions well.

(5). We demonstrated that the coating could reduce singularities and suppress delamination in flexible electronic structures. As we know, the coating reduces the concentrated stresses around the bi-material wedge or triple junction by reducing the elastic mismatch and closing the geometric discontinuity. Wedge or junction is very common to many microelectronic structures, such as in chip-package and package-board. Once the stress concentration is alleviated, many failure modes could be avoided, such as interfacial debonding, solder bump's detachment, etc. Hence, we expect that the coating enhance the reliability of many other microelectronic devices.

(6). In the problem of voiding due to thermal strain and electromigration, the temperature can be not uniform in the Cu line. Therefore, the initial stress gradient due to temperature gradient could initiate multiple voids in the Cu line. After applying electric current, the combination effects of electromigration and thermal gradient maybe lead to multiple voids in saturated state.

We eagerly await future works on these topics.